Université du Québec

Institut national de la recherche scientifique

Centre Énergie, Matériaux et Télécommunications

PHOTON STATISTICS: A VERSATILE TOOL FOR CLASSICAL AND QUANTUM APPLICATIONS

Par

Agnes George

Thèse présentée pour l'obtention du grade de

Philosophiae Doctor, Ph.D.

en sciences de l'énergie et des matériaux

Jury d'évaluation

Directeur de recherche	Prof. Roberto Morandotti INRS-EMT
Président du jury et examinateur interne	Prof. Bienvenu Irenge Ndagano INRS-EMT
Examinateur externe	Prof. Pablo Bianucci Concordia University
Examinateur externe	Prof. Kai Wang McGill University

ACKNOWLEDGEMENTS

First and foremost, I am deeply indebted to my PhD supervisor, Prof. Roberto Morandotti. His constant support, guidance, and encouragement have been invaluable throughout the entire process. His patience and mentorship have been crucial in my academic growth.

In addition, I would like to express my deepest appreciation to my post-docs, whose support has been a constant source of motivation. I thank Dr. Andrew Bruhacs and Dr. Aadhi Abdul Rahim for their collaboration, mentorship and guidance in the nanolaser project. Our collaborative writing sessions and informal discussions, whether held through screens during lockdowns or in person whenever circumstances permitted, offered much-needed support during the toughest times. Furthermore, I would like to thank Dr. Mario Chemnitz for including and mentoring me in the coupled fiber-loop project, especially during the period of lock-down. The skills I earned those days have certainly helped me to finish my PhD.

I must give special recognition to Dr. Nicola Montaut, who has been my advisor during the final stages of my quantum metrology project. Her extensive feedback and expert guidance have played an important role in refining my academic writing and strengthening my arguments. Beyond her academic supervision, she has also been a remarkable friend, always there to provide support when I needed it.

I am also deeply grateful to our collaborators, Prof. Mercedeh Khajavikhan (CREOL, University of Central Florida), for providing the nanolasers used in this work, and Prof. Ulf Peschel (Institute of Condensed Matter Theory and Optics, Friedrich Schiller University), for his invaluable guidance and insightful discussions on the coupled fiber-loop system. His research group worked closely with us in building the setup and performing the measurements. Their expertise and support have been instrumental in shaping this research, and I truly appreciate their contributions and generosity in sharing their knowledge.

I am grateful to Robin Helsten for building custom mechanical and electronic components, without which both my projects would not have been possible. I am also thankful to Benjamin Crockett, who helped me to write the French summary of my thesis. I would like to extend my gratitude towards Monika, Dr. Farzam Nosrati, Kobra Mahdavipour, Dr. Stefania Sciara, Shashwath S Bharadwaj, Dr. Navathej Preetha Genesh, Mayank Kumar, fellow group members and all my friends at INRS and in India for their constant support.

Finally, I would like to thank my family, who have always supported me despite the physical distance. I thank my parents, Dally and George, and my sister, Anna, for always being my pillars of strength. I extend my heartfelt gratitude to my husband, Alex, for accompanying me through the ups and downs of

this academic journey. Their constant support and unwavering faith in me have been a source of determination, inspiration, and motivation.

ABSTRACT

Photon statistics is a branch of physics that involves observing the behavior of single or a small number of photons and then aggregating the results through statistical averaging. This process is essential to obtain meaningful and reliable data, especially in quantum optics research. Photon statistics provides valuable information about correlations in the electromagnetic field and characteristics of the type of light being measured. For example, second-order correlation function obtained via Hanbury Brown and Twiss experiment is the fundamental way to differentiate between coherent, chaotic and quantum light.

Moreover, extensive investigations into the quantum properties of light resulted in significant progress that allows for precise control of quantum optical systems and sets the stage for genuine quantum engineering. This progress extends to applications in confirming the generation of entangled photons and exploring their properties for various purposes. The non-classical correlation between the entangled photons has resulted in various quantum optical techniques that enable the practical implementation of conceptual experiments that probe the core principles of quantum theory. This enhanced control over quantum phenomena offers exciting opportunities to explore novel information-processing approaches, with the potential to revolutionize technologies rooted in quantum information science.

Driven by the significance and pivotal role of photon statistics, our research pursuits were directed toward two specific domains: the characterization of nanolasers and the characterization of time-bin entangled photons. In the first segment, we delve into the realm of metallic coaxial nanolasers, renowned for their intriguing threshold-less lasing behavior. Through comprehensive photon statistics analysis, we seek to unravel the coherence properties inherent in these nanolasers. Our focus also lies on understanding the elusive threshold-less operation, which has remained a subject of debate and intrigue. To evaluate this unique lasing characteristic, we conduct rigorous second-order coherence measurements alongside time-resolved second-order correlation analyses.

The second segment of this study ventures into the generation and characterization of high-dimensional time-bin entangled states, a critical resource for quantum technological applications. We simulate a synthetic photonic lattice by employing a coupled fiber-loop system to perform various quantum walk schemes to generate and process high-dimensional time-bin entangled states. Our investigation focuses on the quantum interference phenomena through detailed photon statistics analysis, with an emphasis on their applications across diverse quantum technologies.

Through these two interconnected research endeavors, this thesis demonstrates the profound significance of photon statistics as a versatile tool, bridging classical and quantum realms, and paving the way for advancements in diverse applications, ranging from nanolasers to quantum technologies.

Keywords: Photon statistics, correlation functions, thresholdless laser, quantum optics, entanglement, quantum interference, quantum walks.

SOMMAIRE RÉCAPITULATIF

STATISTIQUES DES PHOTONS: UN OUTIL POLYVALENT POUR LES APPLICATIONS CLASSIQUES ET QUANTIQUES

Résumé

Les statistiques sur les photons sont une branche de la physique qui implique l'observation du comportement d'un seul ou d'un petit nombre de photons, puis l'agrégation des résultats par le biais d'une moyenne statistique. Ce processus est essentiel pour obtenir des données significatives et fiables, en particulier dans la recherche en optique quantique, telles que des informations précieuses sur les corrélations dans le champ électromagnétique et les caractéristiques du type de lumière mesuré. Par exemple, la fonction de corrélation de second ordre obtenue facilement par l'expérience de Hanbury Brown et Twiss est le moyen fondamental de différencier une lumière cohérente et chaotique d'une lumière quantique. Les recherches approfondies sur les propriétés quantiques de la lumière ont abouti à des progrès notables qui permettent un contrôle précis des systèmes optiques quantiques et ouvrent la voie à une véritable ingénierie quantique. Cela nous amène à l'application suivante des statistiques sur les photons, la confirmation de la création des photons intriqués. La corrélation non classique entre les photons intriqués a donné naissance à diverses techniques d'optique quantique qui permettent la mise en œuvre pratique d'expériences conceptuelles qui sondent les principes fondamentaux de la théorie quantique. Ce contrôle accru des phénomènes quantiques offre des possibilités passionnantes d'explorer de nouvelles approches de traitement de l'information, susceptibles de révolutionner les technologies fondées sur la science de l'information quantique.

Motivés par l'importance et le rôle central des statistiques sur les photons, nos travaux de recherche ont été orientés vers deux domaines spécifiques : la caractérisation des nanolasers et la caractérisation des photons intriqués dans le temps pour des applications en métrologie quantique. Dans le premier segment, nous nous plongeons dans le domaine des nanolasers coaxiaux métalliques, réputés pour leur comportement intriguant de lasing sans seuil. Grâce à une analyse statistique complète des photons, nous cherchons à démêler les propriétés de cohérence inhérentes à ces nanolasers. Notre objectif est de comprendre l'insaisissable fonctionnement sans seuil, qui est resté un sujet de débat et d'intrigue. Pour évaluer cette caractéristique unique, nous effectuons des mesures rigoureuses de cohérence du second ordre ainsi que des analyses de corrélation du second ordre résolues dans le temps.

La deuxième partie de cette thèse porte sur la génération de photons intriqués dans le temps, une ressource essentielle pour les applications de technologies quantiques. En utilisant un système de boucles de fibre couplées, nous simulons un réseau photonique synthétique pour effectuer divers schémas de marche

quantique afin de traiter des états intriqués en dimension élevée dans la base des créneaux temporels (*time-bin)*.

Grâce à ces deux projets de recherche interconnectés, cette thèse démontre la signification profonde des statistiques sur les photons en tant qu'outil polyvalent, faisant le lien entre les domaines classique et quantique, et ouvrant la voie à des avancées dans diverses applications, allant des nanolasers à la métrologie quantique.

1. Caractérisation du nanolaser coaxial métallique

Introduction

Les progrès constants de la société moderne, dans des domaines tels que les soins de santé, l'éducation et les transports, dépendent fortement de notre capacité à générer, traiter, transmettre et recevoir des données. Actuellement, les dispositifs et circuits électroniques jouent un rôle important dans la réalisation de ces tâches, mais ils sont limités par des facteurs tels que la vitesse, la consommation d'énergie et les effets d'auto-échauffement. Pour surmonter ces limitations, la vision d'avenir consiste à remplacer les dispositifs et circuits électroniques par des équivalents photoniques. Les éléments fondamentaux de tout système photonique sont les sources de lumière. Au départ, comme les premiers transistors, les premiers lasers étaient des dispositifs macroscopiques, occupant une surface physique importante allant de quelques centimètres à quelques décimètres. Lorsque la taille d'une cavité électromagnétique est réduite par rapport à la longueur d'onde d'émission, des phénomènes physiques fascinants, spécifiques à ces cavités, apparaissent. Par exemple, les premières expériences menées dans les fréquences radio et micro-ondes ont montré que le taux d'émission spontanée des atomes à l'intérieur d'une cavité pouvait être soit augmenté soit inhibé par rapport à leur taux d'émission dans l'espace libre. Cette modification du taux d'émission spontanée s'est avérée être influencée par la géométrie de la cavité ainsi que par l'orientation et les spectres des atomes. Ce phénomène, connu sous le nom d'effet Purcell, a trouvé des applications significatives, notamment dans les lasers à diode avec une largeur de bande de modulation améliorée, une efficacité énergétique accrue et un éclairage sans seuil.

Un nanolaser souhaitable doit avoir un seuil très bas et présenter des dimensions inférieures à la longueur d'onde dans les trois directions, à la fois dans sa taille physique et dans le confinement de son mode optique. De tels dispositifs sont essentiels pour diverses applications pratiques, notamment les circuits photoniques hautement intégrés à l'échelle de la puce, les écrans et les capteurs. Diverses architectures de lasers à petite échelle, y compris les VCSEL, les lasers à micropiliers, les lasers à cristaux photoniques, etc. ont été introduites. Cependant, la structure globale reste relativement grande, tandis que pour d'autres, les modes ne sont pas bien confinés dans leurs régions actives et peuvent s'étendre au-delà des limites physiques de la cavité, conduisant à un couplage de mode indésirable entre les dispositifs voisins.

Les nanolasers à revêtement métallique, introduits à la fin des années 2000, ont révolutionné ce domaine en permettant à la fois des empreintes physiques inférieures à la longueur d'onde et des volumes de modes. Dans les métaux, les modes excités sont connus sous le nom de polaritons plasmoniques de surface (SPP), qui consistent en un photon couplé à une oscillation collective d'électrons. Les SPP ont une longueur d'onde effective plus courte que la longueur d'onde dans l'espace libre. Cela permet de confiner les champs électriques à des échelles inférieures à la longueur d'onde. La gaine métallique guide efficacement les

modes optiques, ce qui permet une conception précise de la cavité afin de canaliser la majeure partie de l'émission spontanée dans le mode de télédiffusion, ce qui se traduit par des valeurs β élevées, qui décrivent le degré d'utilisation de l'émission spontanée dans le mode de télédiffusion, donnant ainsi lieu à une télédiffusion sans seuil. Cependant, il est important de noter que les nanolasers ont un seuil et ne doivent pas être confondus avec un hypothétique seuil zéro. Le seuil de ces lasers ne peut pas être déterminé par les approches classiques habituelles, telles que le rétrécissement de la largeur de ligne ou la courbe d'entrée et de sortie de la lumière (courbe $L - L$). Par conséquent, nous devons utiliser des mesures de corrélation de second ordre ($g^2(0)$) effectuées par le biais de la configuration Hanbury Brown et Twiss (HBT) pour déterminer le seuil réel. Cette fonction dépend de la nature de la source lumineuse et est indépendante de la puissance d'entrée ou de sortie.

Nanolaser coaxial métallique

Dans nos études, nous avons utilisé un nanolaser coaxial métallique dont les dimensions sont R_{core} = 65 nm et Δ = 285 nm (le schéma du nanolaser coaxial métallique est présenté à la figure 1). Le laser comprend un barreau métallique (R_{core}) entouré d'un anneau semi-conducteur recouvert d'un métal argenté, qui agit comme un dissipateur thermique efficace, facilitant le processus de télédiffusion sous pompage optique, et un milieu de gain, qui consiste en six couches alternées empilées verticalement sous la forme d'anneaux d'$In_{x=0,56}Ga_{1-x}As_{y=0,938}P_{1-y}$ et $In_{x=0,734}Ga_{1-x}As_{y=0,57}P_{1-y}$ d'une épaisseur de 10 nm et 20 nm, respectivement. Le système de puits quantiques d'une hauteur totale de $h = 260$ nm est protégé par SiO_2 (30 nm) et InP (10 nm) pour la couche supérieure, ainsi que par un bouchon d'air (20 nm) dans la partie inférieure. Les faces supérieure et inférieure, terminées respectivement par un bouchon de SiO_2 et de l'air, améliorent le confinement des modes. En outre, la couche de SiO_2 empêche la formation de modes plasmoniques indésirables à l'interface, tandis que le bouchon d'air inférieur permet le pompage optique et le découplage de la lumière. Cette cavité coaxiale présente plusieurs propriétés prometteuses d'un nanolaser “ideal”, notamment la capacité de supporter des modes confinés ultra-petits malgré une longueur d'onde inférieure.

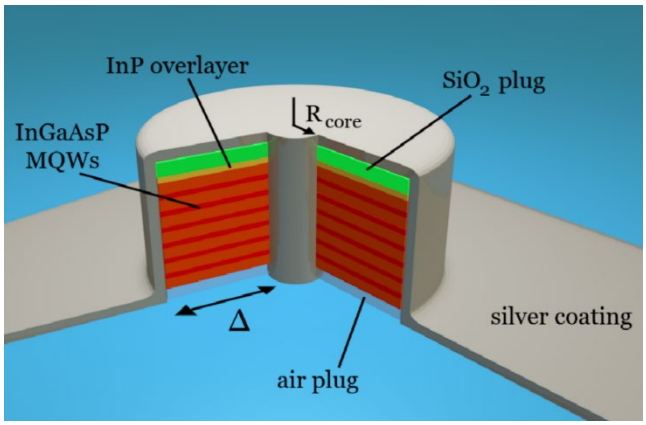

Fig. 1 : Schéma d'un nanolaser coaxial métallique. Le système a la forme d'un pilier composé de puits multi-quantiques InGaAsP, entourant un cœur métallique plasmonique. Les côtés supérieur et inférieur sont terminés par un bouchon de SiO_2 et de l'air, respectivement, pour améliorer le confinement des modes.

L'échantillon contenant les nanolasers coaxiaux métalliques a été refroidi à des températures cryogéniques (77 K) et maintenu à une pression de 10^{-2} mbar. Cela a permis de surmonter les pertes métalliques en réduisant les pertes par effet Joule et en augmentant le gain semi-conducteur réalisable, améliorant ainsi les performances de la nanolaser coaxiale métallique. Par conséquent, le nombre de photons émis était suffisamment élevé pour notre système de détection de photons uniques.

Dispositif expérimental

Le nanolaser coaxial métallique a été pompé optiquement par un laser Q-switché de 1064 nm avec une largeur d'impulsion de 5 ns à un taux de répétition de 1 MHz. Un atténuateur a été installé afin de contrôler la puissance d'entrée délivrée au nanolaser coaxial métallique sans modifier les conditions de gain du laser de pompage. Compte tenu de notre taille de spot de 150 µm déterminée à partir de mesures en lame de couteau, la fluence de pointe au nanolaser par impulsion de pompe est estimée à 310 W/cm2, pour une puissance d'entrée moyenne de 150 µW à 1 MHz. Une illustration détaillée du dispositif expérimental est présentée à la figure 2.

Le dispositif expérimental comporte un miroir cinématique qui dirige la sortie couplée du nanolaser coaxial métallique soit vers un monochromateur, soit vers un montage HBT. Le premier caractérise les propriétés spectrales, y compris le spectre et la largeur de raie, en utilisant un monochromateur en plus de l'analyse de la courbe $L - L$. Le second étudie les propriétés de cohérence et la largeur de raie. La seconde étudie les propriétés de cohérence et la dynamique temporelle de l'émission du nanolaser. La configuration HBT se compose d'une paire de détecteurs de photons uniques à nanofils supraconducteurs très sensibles et d'un marqueur de temps électronique, qui sont placés après le séparateur de faisceau non polarisant 50:50. Sur

ce dernier chemin, la lumière est passée à travers un réseau de diffraction et une fente avant la mesure de $g^2(0)$ pour le filtrage spectral et l'élimination de toute fuite de la pompe.

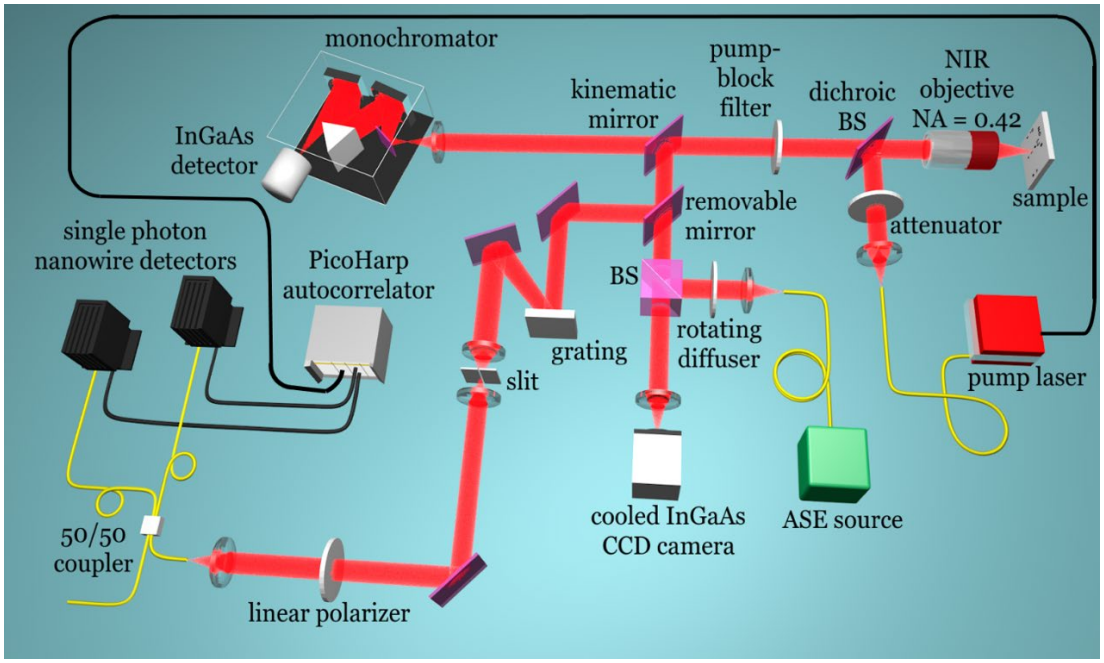

Fig. 2 : Montage expérimental pour la cohérence statistique des photons et les mesures spectrales. L'échantillon contenant les nanolasers est maintenu au foyer d'un objectif. L'émission du nanolaser coaxial métallique est dirigée vers trois lignes de faisceau distinctes (caméra CCD dans le proche infrarouge, spectromètre ou détecteurs de photons uniques). L'échantillon est refroidi à 77 K (chambre cryogénique et alimentation de refroidissement non représentées). Le schéma de pompage optique peut être modifié en mode CW ou en mode pulsé avec différents taux de répétition, durées et formes d'impulsions.

Résultats

Le dispositif de mesure de la microphotoluminescence a été utilisé pour effectuer des mesures classiques. Le nanolaser coaxial métallique a été excité à l'aide d'un laser pulsé. Nous avons fait varier la puissance d'entrée moyenne entre 45 µW et 750 µW. L'émission a été collectée et envoyée au monochromateur. Initialement, les données spectrales ont été collectées et la longueur d'onde d'émission s'est avérée être ~1300 nm. En outre, nous avons observé un décalage bleu avec l'augmentation de la puissance, qui a été attribuée à la saturation des états d'énergie dans le puits quantique induite par les porteurs localisés. Avec l'augmentation de la puissance de la pompe et la saturation des états quantiques, les porteurs libres ont tendance à sortir de ces états, ce qui provoque un décalage vers le bleu de l'émission de photoluminescence. En outre, nous avons mesuré la largeur de ligne de l'émission du nanolaser, qui augmentait avec la puissance d'entrée. Cet élargissement pourrait être le résultat de fluctuations de l'indice de réfraction liées à la densité de porteurs et à l'effet d'auto-échauffement.

Nous avons également tracé la courbe $L - L$ pour le nanolaser coaxial, où la puissance de sortie est obtenue en intégrant la densité spectrale de puissance sur l'ensemble du pic PL en fonction de la puissance d'entrée

moyenne. Au lieu d'une courbe typique en forme de "S", nous avons observé un comportement linéaire sans coude prononcé. L'absence de coude est typique des lasers à haut$-\beta$ et s'accorde bien avec l'hypothèse d'un laser sans seuil. Cependant, le concept de fonctionnement sans seuil basé sur la courbe $L-L$ est un sujet de débat et nous avons donc effectué des mesures statistiques de photons pour étudier son comportement sans seuil.

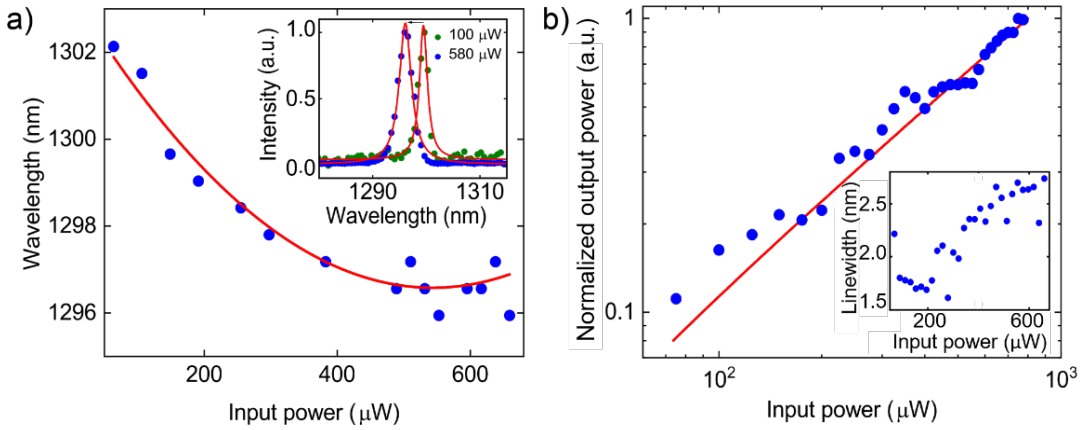

Fig. 3 : a) Diminution de la longueur d'onde centrale pour des valeurs croissantes de la puissance d'entrée moyenne. L'encadré montre les spectres de photoluminescence à deux puissances de pompe d'entrée différentes. b) Graphique normalisé de la puissance d'entrée-sortie du nanolaser coaxial métallique sur une échelle logarithmique. Notamment, ces mesures n'ont révélé aucun comportement de lasing de type seuil.

Après la caractérisation classique du nanolaser, nous avons effectué des mesures HBT pulsées pour déterminer les statistiques des photons. Tout d'abord, nous avons calculé la moyenne de la fonction de corrélation de second ordre sur l'ensemble de l'impulsion de pompe, comme c'est généralement le cas. Le $g^2(0)$ pour différentes puissances d'entrée a été déterminé. Nous avons observé que même si la courbe $L-L$ montrait une émission sans seuil, le nanolaser pose un seuil. Au fur et à mesure que la puissance d'entrée augmentait, il y avait une transition de l'émission chaotique à l'émission cohérente de photons du nanolaser. L'émission chaotique dans le régime à faible puissance d'entrée est due à une émission spontanée qui commence progressivement à émettre au seuil. D'après la mesure HBT, le seuil a été déterminé à ~400 μW, où la valeur de $g^2(0)$ est proche de l'unité. Un léger écart par rapport à l'unité a été observé même pour des puissances d'entrée plus élevées en raison des fluctuations d'amplitude de l'impulsion de pompe.

En outre, la largeur du pic de corrélation normalisé pour différentes puissances de pompe a également été déterminée pour suivre la transition d'un comportement thermique à un comportement cohérent, car le FWHM est influencé par l'impulsion de pompe et la durée de vie des photons. Nous avons observé qu'initialement, la largeur du pic se rétrécit à mesure que l'intensité de la pompe augmente dans le régime d'émission spontanée, et tombe au minimum dans le régime d'émission spontanée amplifiée. Pour les

puissances d'entrée supérieures au seuil, la largeur du pic s'élargit, puis se rétrécit à nouveau pour des puissances de pompe plus élevées en raison des effets de chauffage.

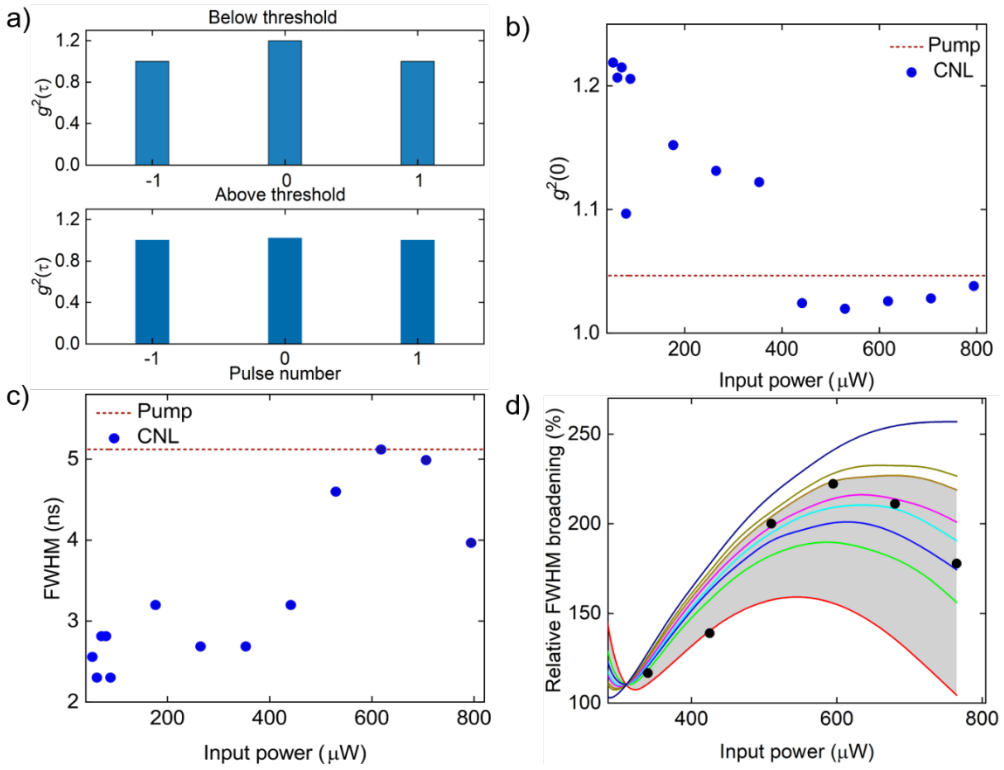

Fig. 4 : a) Exemple de mesure de $\boldsymbol{g^2(0)}$ au-dessus et au-dessous du seuil. b) Valeurs de la fonction de corrélation du second ordre $\boldsymbol{g^2(0)}$ tracées pour une puissance de pompe variable. c) FWHM des pics de corrélation en fonction de la puissance moyenne. d) FWHM de la trace d'autocorrélation en fonction de la puissance de pompe obtenue à partir du modèle de l'équation de taux.

En outre, nous avons mené une étude détaillée de la fonction de corrélation de second ordre résolue dans le temps ($g^2(t, \tau = 0)$) dans la durée de l'impulsion émise par le nanolaser coaxial métallique, en utilisant des fenêtres temporelles plus étroites sur l'ensemble de l'enveloppe temporelle de l'impulsion. Nous avons cartographié la transition d'une réponse thermique à une réponse cohérente des impulsions émises dans l'enveloppe de l'impulsion à différents niveaux de puissance d'entrée, sans qu'il soit nécessaire de procéder à un filtrage spectral supplémentaire. Nous avons observé que le front d'attaque de l'impulsion de pompe génère des porteurs dans les états supérieurs du puits quantique ou de la barrière et que ces porteurs se relaxent rapidement dans les états inférieurs du puits quantique, produisant une émission spontanée ($g^2(0) > 1$). Lorsque l'intensité de l'impulsion de pompe augmente dans le temps, la population devient suffisamment forte et le système passe au régime d'émission cohérente ($g^2(0) = 1$). Comme les cavités des nanolasers ont une réponse ultrarapide, au bord de fuite de l'enveloppe de l'impulsion (où l'intensité de l'impulsion de pompe est faible), l'émission spontanée domine sur l'émission cohérente, ce qui conduit à

$g^2(0) > 1$. En outre, pour des densités d'excitation plus élevées, l'émission stimulée est maintenue plus longtemps, ce qui entraîne une asymétrie dans les données résolues en temps.

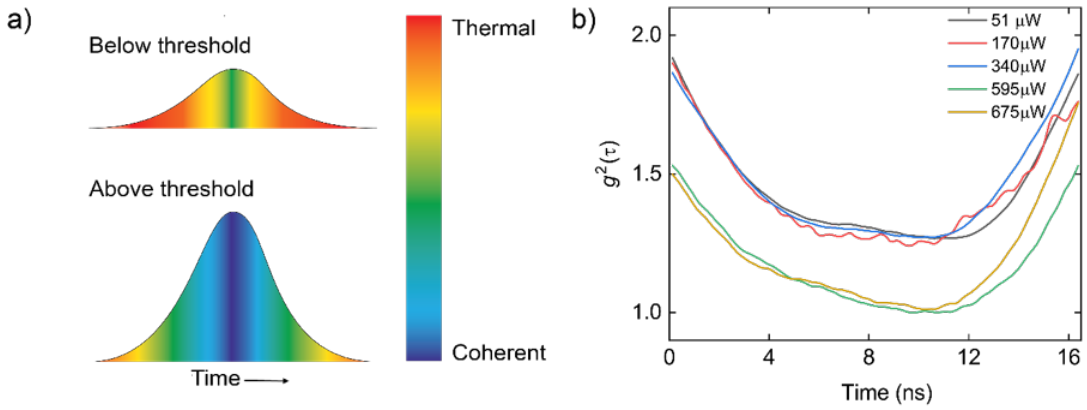

Fig. 5 : a) Schéma de la statistique des photons attendue en fonction de l'enveloppe temporelle de l'impulsion émise pour deux cas, au-dessus et au-dessous du seuil. b) Évolution de $\boldsymbol{g^2(\tau)}$ d'un comportement thermique (regroupement de photons) à un comportement cohérent balayé sur la longueur de l'impulsion émise.

En résumé, notre enquête a fait appel à la caractérisation classique et à la statistique des photons pour étudier de manière exhaustive les propriétés d'émission d'un nanolaser sans seuil. Il est devenu évident que les méthodes conventionnelles telles que le graphe $L - L$ et la caractérisation spectrale étaient insuffisantes, et les statistiques de photons sont apparues comme l'approche clé pour extraire le comportement d'émission du nanolaser. Nos résultats indiquent que l'émission du nanolaser, même à des puissances d'entrée plus élevées, comprend une combinaison d'émissions spontanées et stimulées.

2. Caractérisation de l'état intriqué dans le temps

Introduction

Le contrôle accru des phénomènes quantiques, grâce aux progrès réalisés dans le domaine de l'ingénierie quantique, offre des possibilités passionnantes d'explorer de nouvelles approches du traitement de l'information. L'une des ressources les plus importantes dans la technologie quantique est l'intrication, essentielle notamment pour le calcul quantique, la communication quantique, la simulation quantique et la métrologie quantique. L'intrication est un phénomène purement quantique qui fait référence à la corrélation entre d'au moins deux systèmes, où l'état d'un système ne peut pas être décrit indépendamment de l'autre. L'intrication est la clé qui permet d'atteindre la « suprématie quantique », en particulier dans les systèmes utilisant des qubits. Le qubit, un système à deux niveaux, est l'unité de base de l'information dans la technologie quantique.

L'information quantique peut être encodée dans divers systèmes physiques, notamment les atomes de Rydberg, les ions piégés, les défauts à l'état solide, les molécules polaires, les circuits supraconducteurs et les photons. Parmi les divers systèmes physiques qui peuvent être utilisés, les photons sont particulièrement adaptés pour le traitement de l'information quantique en raison de leurs propriétés avantageuses telles que la haute vitesse, l'interaction minimale avec l'environnement, les longs temps de cohérence et les technologies bien établies pour leur génération, leur manipulation et leur détection. De plus, ils possèdent de nombreux degrés de liberté externes ainsi qu'internes qui peuvent être exploités. Les degrés de liberté internes incluent la polarisation, le moment angulaire orbital, la fréquence et le temps de génération, tandis que les degrés de liberté externes incluent la position spatiale et le chemin parcouru par un photon. En conséquence, le développement de plateformes et de techniques pour générer des états photoniques quantiques appropriés est crucial pour leur déploiement pour des technologies pratiques.

Les premières expériences utilisant la polarisation, les chemins optiques et les modes de moment angulaire orbital ont été réalisées dans l'espace libre. Cependant, le développement des télécommunications basées sur les fibres a conduit à l'exploitation de degrés de liberté qui sont plus robustes et compatibles avec les fibres, tels que la fréquence et le temps. L'idée d'utiliser des créneaux temporels pour porter l'informations quantiques a été proposée pour la première fois en 1989 et des expériences ultérieures ont démontré avec succès l'intrication bidimensionnelle des créneaux temporels. Pour créer une intrication entre deux photons et coder l'information quantique dans le domaine de l'intervalle de temps, on utilise deux impulsions laser indiscernables séparées par une différence de temps fixe. Chaque impulsion laser génère des paires de photons à l'aide d'une source de lumière non linéaire telle que la conversion paramétrique spontanée vers le bas (*spontaneous parametric down conversion,* SPDC).

Pour des applications telles que la communication ou l'informatique quantiques, les systèmes quantiques à haute dimension, ou qudits, offrent des avantages par rapport aux qubits en raison de leur plus grande capacité d'information, de leur sécurité accrue et de leur résistance au bruit. Par conséquent, l'intrication quantique de haute dimension fournit un domaine riche tant pour la recherche fondamentale que pour l'innovation technologique.

En principe, la dimensionnalité des états intriqués dans l'intervalle de temps peut être augmentée en augmentant le nombre d'impulsions indiscernables. Cependant, la caractérisation des états intriqués à haute dimension nécessite l'estimation de nombreux paramètres, tels que les valeurs de phase multiples qui découlent des retards entre les impulsions. Le processus d'estimation nécessite un grand nombre de mesures, ce qui devient peu pratique à mesure que la dimensionnalité augmente. Les limitations expérimentales deviennent donc des obstacles considérables pour un traitement efficace de l'intrication. Leur caractérisation implique généralement l'utilisation d'interféromètres déséquilibrés en cascade, où chaque interféromètre mesure la phase entre deux intervalles de temps. Ainsi, pour obtenir des états intriqués dans un intervalle de temps de dimension N, il faut $N-1$ interféromètres, ce qui devient irréalisable pour les grandes dimensions. En outre, cela se traduit par une complexité et un coût expérimentaux considérables. Par conséquent, des méthodes efficaces et innovantes pour générer et traiter des états intriqués à haute dimension dans le temps, en particulier dans les fibres optiques, sont cruciales pour la communication quantique pratique.

Dans les réseaux de fibres optiques, la génération et le traitement d'états intriqués à haute dimension dans le temps peuvent être réalisés par des marches quantiques. Les marches quantiques, l'analogue quantique des marches aléatoires classiques, reposent sur l'interférence et la superposition. En tant que dispositif de mesure généralisé, elles décrivent efficacement le transport de photons intriqués dans les réseaux de fibres optiques. Par exemple, un système de boucles de fibre couplées, qui peuvent simuler un réseau photonique synthétique, ont été largement utilisés pour étudier la propagation non linéaire de la lumière à travers des marches quantiques. Cependant, l'application de ce système dans le traitement de l'information quantique et les technologies quantiques rest à explorer.

Ces considérations nous motivent à enquêter expérimentalement sur 1) la génération d'états intriqués de haute dimension en créneaux temporels dans un réseau photonique synthétique et 2) le traitement des états intriqués générés via divers schémas de marche quantique.

Réseau photonique synthétique et marche quantique contrôlée

Dans notre travail, le réseau photonique synthétique est simulé à l'aide d'un système de boucle de fibre couplée comprenant deux boucles de fibre de longueurs variables couplées à un commutateur optique qui

peut contrôler la proportion et la direction du flux de lumière. L'entrée et la sortie des impulsions lumineuses dans le système de boucle de fibre couplée sont également contrôlées par deux autres commutateurs optiques, appelés portes 1 et 2. Pour comprendre le réseau photonique synthétique, considérons la boucle de fibre couplée, où le commutateur optique est maintenu en permanence à un rapport de transmission-réflexion de 50-50. Chaque fois qu'une impulsion lumineuse atteint le commutateur optique, elle se divise en deux boucles, l'une longue et l'autre courte. La différence de temps nécessaire à ces impulsions pour atteindre le séparateur de faisceau après chaque aller-retour correspond à la différence de longueur des boucles de fibre. L'aller-retour et le temps d'arrivée des impulsions définissent respectivement le pas de temps (t) et la position synthétique (x) dans le réseau photonique synthétique, ce qui permet une marche quantique unidimensionnelle en temps discret (DTQW) à l'aide de l'impulsion lumineuse. Cependant, pour obtenir des mesures optimales, nous devons utiliser un schéma de marche quantique contrôlée, dans lequel nous utilisons les propriétés dynamiques du commutateur optique.

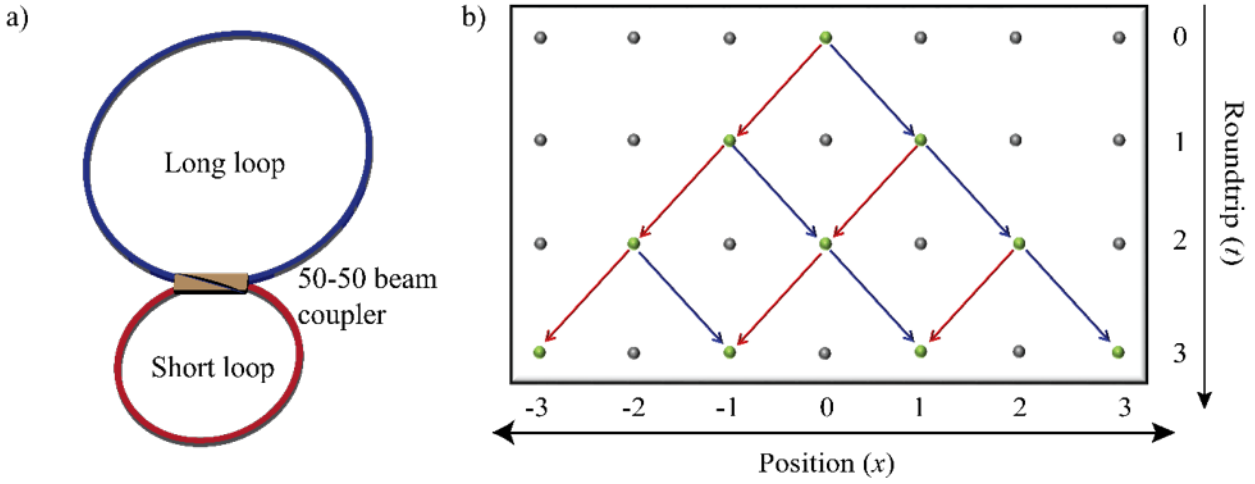

Fig. 6 : a) Boucle de fibre couplée constituée de deux boucles de fibre de longueurs différentes couplées à un coupleur de faisceau 50-50. b) Marche quantique décrivant la propagation d'une impulsion lumineuse dans le système de boucle de fibre couplée.

La marche quantique contrôlée comprend trois opérations, à savoir la réflexion (100:0), la transmission (0:100) et Fourier (50:50) en fonction des rapports de division du coupleur optique. Lorsque l'impulsion lumineuse se trouve dans la boucle longue, l'opération de réflexion passe de la boucle longue à la boucle courte, tandis que pour la transmission, elle reste dans la boucle résidente, c'est-à-dire la boucle longue. Lorsque le commutateur optique est réglé sur le fonctionnement de Fourier, il divise également l'impulsion lumineuse en boucles longues et courtes.

Dispositif expérimental

Le dispositif expérimental complet illustré à la Fig. 7 comprend quatre tâches principales : 1) la génération d'une double impulsion classique, 2) la génération d'un état intriqué dans le temps et le codage de l'information, 3) l'étape de traitement qui comprend la marche quantique et, enfin, 4) l'étape de détection.

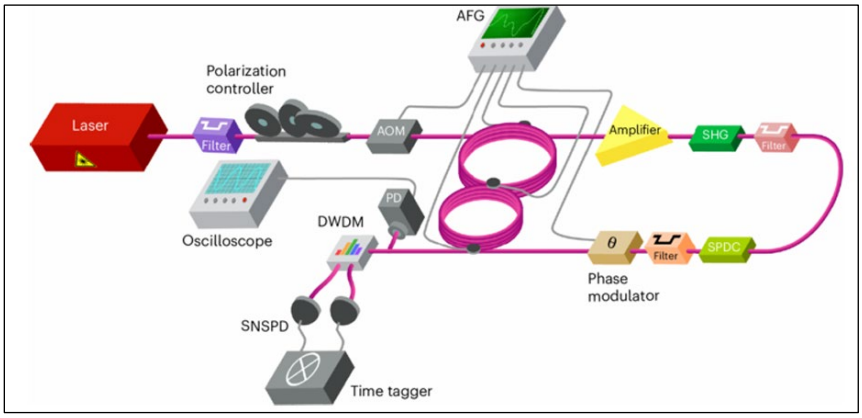

Fig. 7 : Préparation des photons : Le taux de répétition de la sortie du laser fs est réduit à 181,81 kHz à l'aide d'un modulateur acousto-optique (AOM). Ces impulsions sont envoyées au système de boucle pour générer deux impulsions classiques pour la préparation de l'état. Ces impulsions sont transmises aux cristaux PPLN pour la génération d'une paire de photons corrélés dans deux intervalles de temps, $\boldsymbol{t_1}$ et $\boldsymbol{t_2}$. Codage et traitement de la phase : Le modulateur de phase module la phase de l'un des intervalles de temps et est autorisé à interférer dans le système de boucle à fibres optiques. Détection : Les pics d'interférence à différentes phases codées sont envoyés au DWDM pour séparer les photons de signal et les photons parasites. Ces photons sont détectés par des détecteurs de photons uniques à la pointe de la technologie.

L'impulsion classique générée par le laser est dirigée vers la porte 1 pour préparer une double impulsion, le commutateur optique étant maintenu à 50-50 pendant le processus. Les doubles impulsions générées, séparées par un délai correspondant à la différence entre les longueurs des boucles courte et longue, sont utilisées pour exciter une paire de cristaux de niobate de lithium à pôles périodiques (PPLN) afin de générer une paire de photons signal-idler dans deux intervalles de temps, t_1 et t_2. Ensuite, l'état quantique préparé subit un codage individuel de l'information de phase $\phi = \{\phi_1, \phi_2, \ldots \phi_n\}$ à l'aide d'un modulateur de phase. L'état résultant, $|\psi_1\rangle = \frac{1}{\sqrt{2}} \left(|t_1, t_1\rangle_{s,i} + e^{2i\phi}|t_2, t_2\rangle_{s,i}\right)$, est ensuite injecté dans la plate-forme de marche quantique par la porte 2 pour subir le schéma de mesure optimal utilisant le schéma de marche contrôlée, qui nécessite deux allers-retours (Fig. 8).

Pour le DTQW non contrôlé, l'interrupteur optique était réglé sur l'opération de Fourier en permanence. Lors du second aller-retour, la première fenêtre temporelle dans la boucle longue et la seconde fenêtre temporelle dans la boucle courte ont atteint l'interrupteur optique en même temps, entraînant une interférence quantique. Le composant interféré dans la boucle courte a ensuite été extrait par la porte 2 et a été dirigé vers l'étape de détection.

Pour le DTQW contrôlé, au départ, les boîtes quantiques sont injectées dans le système par la boucle courte. Au cours du premier aller-retour, nous effectuons des opérations de réflexion et de transmission pour régir l'arrivée de t_1 et t_2, en déplaçant t_1 vers la boucle longue ($x = -1$) et t_2 vers la boucle courte ($x = 1$). Dans l'aller-retour suivant, l'opération de Fourier répartit les composantes d'interférence entre les boucles courte et longue. Enfin, ces composantes d'interférence sont dirigées vers l'étage de détection par la porte 2. Un multiplexeur dense à répartition en longueur d'onde (DWDM), compatible avec les télécommunications, sépare les photons du signal et les photons parasites, qui sont envoyés aux détecteurs de photons uniques de pointe. L'heure d'arrivée du signal et des photons parasites est enregistrée par un système électronique de marquage temporel.

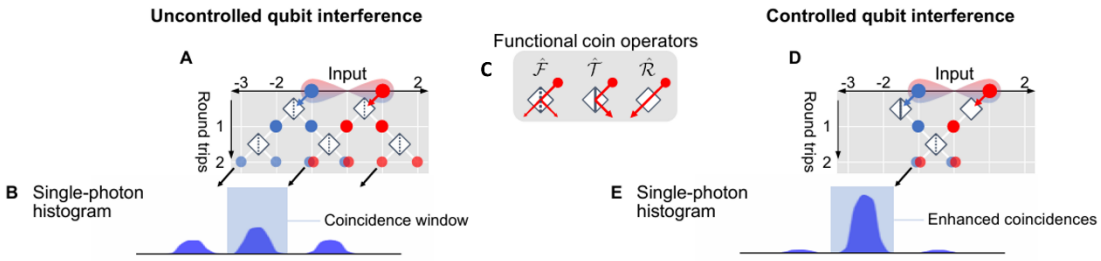

Fig. 8 : Le schéma de marche quantique non contrôlée a) et contrôlée d) dans un réseau photonique synthétique. c) représente diverses opérations de pièce utilisées dans la marche quantique. b) et e) sont les illustrations des histogrammes de photons uniques obtenus dans les schémas de marche quantique contrôlée et non contrôlée. Les flèches bleues et rouges représentent respectivement les boucles courte et longue.

Nous avons également généré des états intriqués en temps-bin de quatre dimensions sur la même plateforme. Contrairement au cas à deux dimensions, cela nécessitait quatre aller-retours. Une fois que les quatre impulsions classiques en superposition cohérente ont été générées, elles ont été envoyées pour exciter une paire de guides d'onde PPLN afin de générer des états intriqués en temps-bin de quatre dimensions. L'état quantique est donné par $|\psi_1\rangle = \frac{1}{\sqrt{2}}\left(|t_1, t_1\rangle_{s,i} + e^{2i\phi}|t_2, t_2\rangle_{s,i} + e^{4i\phi}|t_3, t_3\rangle_{s,i} + e^{6i\phi}|t_4, t_4\rangle_{s,i}\right)$.

L'état intriqué en temps-bin de quatre dimensions a ensuite été envoyé au système de boucles de fibre couplées pour le traitement. Nous avons utilisé deux schémas de DTQW contrôlés pour obtenir des franges d'interférence. Le schéma de marche quantique contrôlée 1 consistait en deux opérations : réflexion et Fourier. Pour les deux premiers aller-retours, nous avons maintenu l'interrupteur optique en mode Fourier, et pour le troisième aller-retour, nous avons maintenu l'interrupteur optique en pleine réflexion. Lors du dernier aller-retour, l'interrupteur optique a de nouveau été maintenu en mode Fourier pour subir une interférence quantique. Le signal interféré, ainsi que les modes latéraux, ont ensuite été dirigés vers l'état de détection.

Dans le second schéma de contrôle, nous avons découpé l'état intriqué, c'est-à-dire que les deux premières fenêtres temporelles ont été envoyées dans la boucle longue et les deux dernières fenêtres temporelles ont été conservées dans la boucle courte. Lors du second aller-retour, l'interrupteur optique a été maintenu en mode pleine réflexion, permettant aux fenêtres temporelles de rester dans leurs boucles respectives. Au cours des deux aller-retours suivants, l'interrupteur optique a été maintenu en mode Fourier pour l'interférence quantique. Le signal interféré, ainsi que les modes accompagnants, ont été extraits par la porte 2 et envoyés vers l'étape de détection.

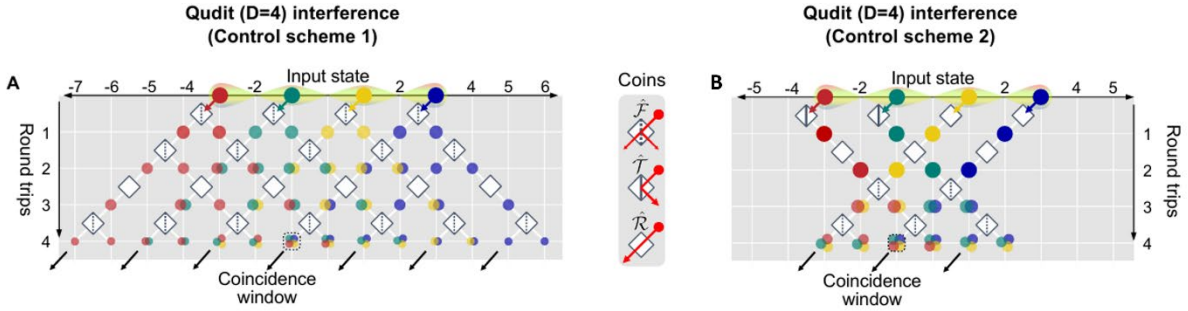

Fig. 9: Les schémas de DTQW contrôlés 1 (a) et 2 (b) dans un réseau photonique synthétique.

Résultats

Nous avons recueilli les statistiques des photons à chaque réglage de phase, $\phi \in (0, \pi)$ et mesuré les franges d'interférence. La Fig. 10 (a) et (b) démontre les franges d'interférence obtenues grâce aux marches quantiques contrôlées et non contrôlées utilisées pour les états intriqués en temps-bin à deux dimensions. Les visibilités de ces franges ont été estimées à 95,45 % et 90,17 %, respectivement, ce qui viole l'inégalité de Bell.

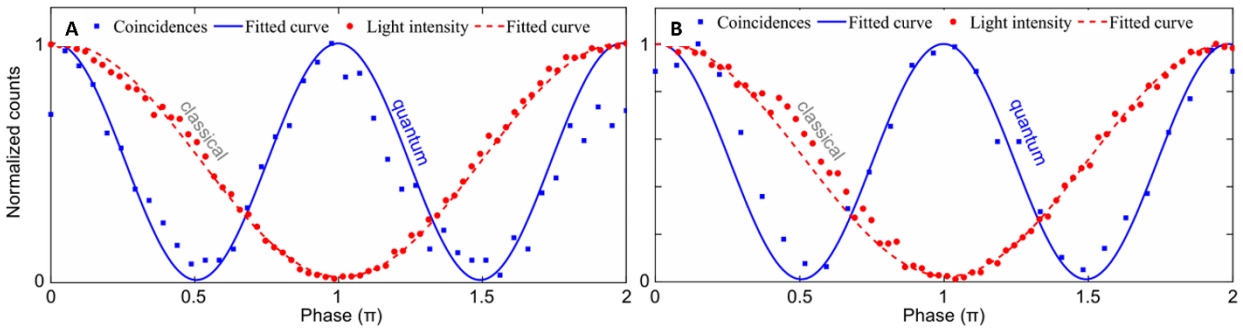

Fig. 10: **Franges d'interférence**. a) Frange d'interférence obtenue en utilisant le schéma de marche quantique non contrôlée. b) Frange d'interférence obtenue grâce au schéma de marche quantique contrôlée.

Les franges d'interférence pour les états intriqués en temps-bin de quatre dimensions obtenues via les schémas de DTQW contrôlés 1 et 2 sont présentées dans la Fig. 11 (a) et (b), respectivement. Les visibilités de ces franges ont été estimées à 91,55 % et 89,51 %, respectivement, et ont violé l'inégalité de CGLM.

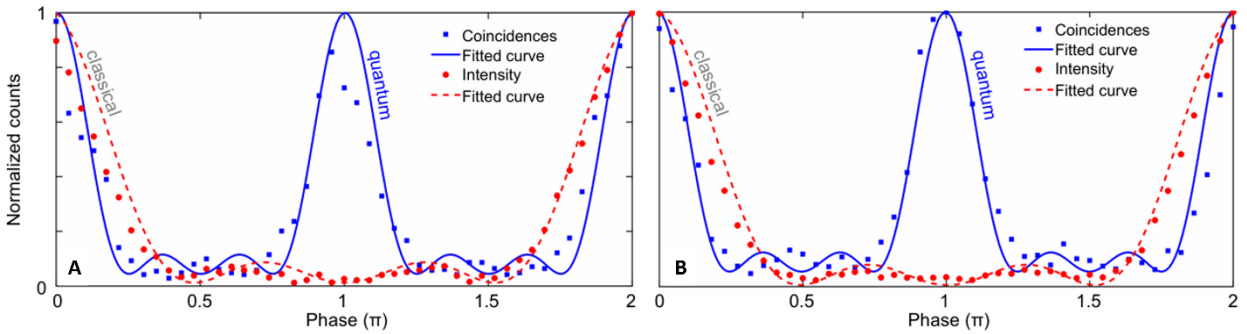

Fig. 11: **Franges d'interférence.** a) Frange d'interférence obtenue en utilisant le schéma de marche quantique contrôlée 1. b) Frange d'interférence obtenue grâce au schéma de marche quantique contrôlée 2.

Nous démontrons les propriétés quantiques des réseaux photoniques synthétiques (SPL) comme un cadre prometteur pour la préparation, la génération et la manipulation de paires de photons intriqués en temps-bin de dimension d basées sur un système de boucle de fibre couplées dynamiquement et une marche quantique en temps discret. Nous avons pu mettre en œuvre un schéma de marche quantique contrôlée nous permettant de mesurer une interférence quantique sans sélection postérieure pour des états intriqués à deux dimensions, ainsi que d'optimiser l'évolution de marches quantiques pour des efficacités de détection et des comptages de coïncidence plus élevés, tant pour les cas à deux que pour ceux à quatre dimensions.

TABLE OF CONTENTS

LIST OF FIGURES

LIST OF TABLES

LIST OF ABBREVIATIONS

ASE	AMPLIFIED SPONTANEOUS EMISSION REGIME
DTQW	DISCRETE TIME QUANTUM WALK
DWDM	DENSE WAVELENGTH-DIVISION MULTIPLEXER
EPR	EINSTEIN, PODOLSKY AND ROSEN
HOM	HONG-OU MANDEL
L-L	LIGHT INPUT - LIGHT OUTPUT
MZI	MACH-ZEHNDER INTERFEROMETER
PL	PHOTOLUMINESCENCE
POVM	POSITIVE OPERATOR-VALUED MEASURE
PPLN	PERIODICALLY POLED LITHIUM NIOBATE
Q **FACTOR**	QUALITY FACTOR
SPDC	SPONTANEOUS PARAMETRIC DOWN CONVERSION
SPL	SYNTHETIC PHOTONIC LATTICE

1 INTRODUCTION

1.1 General introduction

Optics, the study of light and its behavior, could be considered among the oldest branches of physics. Even today, after two thousand years, optics remains a vibrant field of study with significant developments that continue to push the boundaries of our understanding.

In the 17th century, Sir Isaac Newton made a groundbreaking contribution to optics with his work "Opticks", which is widely regarded as one of the most important works in the history of science. He proposed a corpuscular theory, viewing light as small, discrete particles called 'corpuscles'. While this could account for reflection or refraction, it fell short in explaining other optical phenomena such as interference, diffraction, and polarization. On the contrary, Huygens's wave theory suggested that light behaves as waves, leading to an improved understanding of light and providing explanations for various optical phenomena. In the 19th century, James Clarke Maxwell formulated a wave model to describe the wave-like nature of electromagnetic radiation, including light. However, these models were insufficient to explain the characteristics of subatomic particles or their interaction between light and matter as demonstrated by the photoelectric effect, ejection of electrons from a metal surface when it is exposed to light, discovered by Hertz in 1887 (1).

The quantum theory of light had its origins with Plank in 1900 when he proposed that the energy of a harmonic oscillator is quantized based on his observations of blackbody radiation. He found that the harmonic oscillator with angular frequency, ω, can only have energies that are integral multiple of $\frac{h\omega}{2\pi}$, where h is the Planck's constant. Subsequently, in 1905, Albert Einstein again introduced the concept of "corpuscularity" to explain the photoelectric effect, suggesting that light can be regarded as a stream of discrete particles known as photons. However, the term "photon" for the quantum of electromagnetic field was officially coined later in 1926. Shortly after Einstein introduced the concept of light quanta, Taylor in 1909 conducted an experiment using extremely faint light in a two-slit Young-type setup. The light was so weak that, on average, only one photon was present in the apparatus at a time. Surprisingly, no deviation from classical interference patterns was observed. Dirac later accomplished the formal quantization of the electromagnetic field in 1924, introducing the idea of wave-particle duality, where particles can exhibit both wave-like and particle-like behavior. With the development of a fully-fledged theory of quantized light, we now understand that experiments of this nature cannot distinguish between the classical explanation that involves interference of electric field waves and the quantum explanation that involves interference of probability amplitudes for photons passing through the slits (2).

The complete quantum theory of light and matter, known as quantum electrodynamics (QED), was developed around 1950 by Sin-Itiro Tomonaga, Julian Schwinger, Richard Feynman, and Freeman Dyson. QED has exhibited remarkable accuracy in explaining all prevailing electromagnetic phenomena and its inclusion of nuclear processes forms the foundation of the present day model of physics.

The origin of quantum optics began with the invention of laser around 1960, which prompted Roy Glauber to formulate a theory that specifically describes light. In his quantum optics framework, he maintained the QED concept of ordering processes based on the number of particles involved (3, 4). The first order deals with the coherence properties of individual, non-interacting photons and aligns with predictions from wave theory (5). The second order, however, delves into correlations between two photons in terms of both time and space (5). This level of analysis becomes particularly significant because wave theory fails to account for all second-order phenomena. To reconcile theory with experimental results, one commonly assumes space-time separability and then examine simultaneous correlations between pairs of photons. Consequently, multiphoton experiments, which were previously unattainable, now directly unveil the intrinsic quantum nature of the electromagnetic field.

In 1956, Hanbury Brown and Twiss made a ground-breaking contribution to modern quantum optics by introducing intensity interferometry (6). This marked the first serious attempt to explore correlations between intensities measured at two separate detectors, sparking further development in photon counting and correlation experiments. Subsequently, Glauber's quantum theory of optical coherence (3, 4) was verified experimentally through the manipulation of lasers. In the early experiments, atomic beams were employed as sources, leading to unavoidable fluctuations in atomic number and emission statistics. However, progress was made, and in 1987, Diedrich and Walther successfully conducted experiments using a single trapped ion, observing photon antibunching and sub-Poissonian statistics in the system (7). Furthermore, squeezed states of light were experimentally generated using different techniques, such as four-wave mixing in atomic sodium (8) and optical fibers (9), as well as by employing an optical parametric oscillator (10).

Photon detection and counting are key components in all quantum optics experiments. These experiments typically involve observing the behavior of a single or a small number of photons and then aggregating the results through statistical averaging. This process is essential for obtaining meaningful and reliable data in quantum optics research, such as valuable information about correlations in the electromagnetic field and characteristics of the type of light being measured. In typical quantum optics experiments, one measures the number of photons that arrive at a detector within a specific time interval. When more than one photon arrives within the detector time window, they are said to be recorded in coincidence, which means that they arrive at the same time. Quantum optics experiments often focus on the

behavior of only a few photons, with the most studied cases involving the coincident arrival of just two photons.

One practical application of this involves confirming the creation of a so-called two-photon state, which is generated by splitting an incident photon into two photons. Although the creation of such photon pairs is a rare event, it can be achieved using a laser and a nonlinear crystal (11). What makes this phenomenon remarkable is that the two photons, born simultaneously, remain connected or "entangled" even after their creation (12). Einstein in the mid-1930s famously debated this concept, naming it as "spooky action at a distance". However, it was the modern proof of entanglement that earned Alain Aspect, John Clauser, and Anton Zeilinger the Nobel Prize in Physics in 2022 (13). Recent developments in the field of quantum optics resulted in crucial advancement of many quantum technologies, such as lithography (14, 15), quantum communication (11, 16–20), quantum metrology (21–24), quantum computation (25–27), and photonic quantum simulations (28, 29).

1.2 Objectives

The main objective of this thesis is to explore the application of photon statistics in different scenarios. Specifically, we investigate two key areas: characterization of the emission properties of thresholdless nanolasers (30) and characterization of time-bin entangled states (31).

Characterization of the emission properties of thresholdless nanolasers

In this part, we face the challenges arising when we use classical characterization techniques to quantify the thresholdless behavior of nanolasers. To overcome this limitation, we resort to second-order coherence measurements, which provide deeper insights into the emission behavior of these small-scale lasers. The classical characterization includes conventional spectral analysis and Light input - Light output ($L-L$) curves (32), focusing on the emission wavelength and its spectral bandwidth, as well as its dependence on pump power. While narrowing of the spectral bandwidth/linewidth indicates lasing, a straight line in the $L-L$ curve suggests thresholdless behavior (32–34). However, these classical methods alone cannot precisely define the threshold for these nanolasers. To address this, we perform photon statistics by conducting second-order correlation measurements at different pump powers, enabling us to determine the threshold more accurately. Additionally, we delve into the properties of the emission itself by analyzing the temporal profile of the emitted light.

Characterization of time-bin entangled states

The second part of the thesis benefits from the know-how previously acquired and revolves around the characterization of time-bin entangled photons (16). The study involves two main sub-focuses: a) generation, and b) processing of time-bin entangled photons. We generate and process high-dimensional time-bin entangled photons in a synthetic photonic lattice (35, 36), simulated by a coupled fiber-loop system through quantum walks. The coupled fiber-loop system features two fiber loops of different lengths coupled with a programmable optical switch. By leveraging the programmability of the optical switch, various quantum walk schemes are implemented to process the high-dimensional time-bin entangled state (31). The photon statistics of the processed quantum states are collected and analyzed to obtain interference fringes, which are essential for evaluating the quality of the generated entangled states. This process enables precise control over the entangled state without requiring complex experimental setups.

1.3 Thesis structure

The thesis is structured around the two main objectives mentioned earlier. Chapter 2 establishes the fundamental principles of photon statistics and quantum optics, serving as the theoretical foundation for the subsequent chapters. Chapters 3 and 4 build upon this foundation, each dedicated to one of the main objectives: a) characterization of metallic coaxial nanolaser; b) characterization of time-bin entangled states. These chapters provide a comprehensive account of the respective experiments, including an overview, theoretical background, experimental methods, and results obtained.

Chapter 2: Fundamentals of Photon Statistics and Quantum Optics

This chapter provides the theoretical foundation for the thesis. It begins with an introduction to photon statistics and correlation measurements, which are used to categorize different photon sources used in this thesis. The chapter then covers key principles of nonlinear optics, which are exploited to generate entangled photons, and quantum interference, which characterize the generated entangled states and plays a fundamental role in quantum optics experiments. Finally, the chapter discusses quantum walks, highlighting their role in quantum information processing, particularly for the optimal characterization of photonic entangled states.

Chapter 3: Characterization of Metallic Coaxial Nanolaser

This chapter is dedicated to the nanolaser characterization. It commences with an overview, highlighting the significance of nanolaser devices in today's rapidly advancing world and the progress made in this field. Subsequently, the theory and methods employed in our experiments are described, covering material properties, their impact on the nanolaser thresholdless emission, as well as aspects related to photon detection, correlation measurements, and photon statistics. The chapter then presents the experimental setup utilized for the measurements, followed by the main results obtained. A summary concludes the chapter, highlighting the key results.

Chapter 4: Characterization of Time-Bin Entangled States

This chapter centers on the characterization of time-bin entangled states. Like the previous chapter, it begins with an overview that underscores the importance of high-dimensional entangled states for quantum technologies. The theory and methods utilized in the experiment are then elucidated, including discussions on the generation of the time-bin entangled state, quantum interference, and quantum walk. The experimental setup and processing scheme employed for the measurements are presented, and the main results obtained from the measurements are discussed. The chapter concludes with a summary, encapsulating the essential outcomes.

Chapter 5: Conclusion and Outlook

This chapter summarizes the key outcomes of the thesis and discusses their broader impact. It also outlines potential future directions in both nanolaser characterization and time-bin entanglement research.

Chapter 6: Bibliography

This chapter contains a comprehensive list of references cited throughout the thesis.

2 Fundamental Concepts in Photon Statistics and Quantum Optics

Chapter abstract:

This chapter covers the fundamental concepts of photon statistics and quantum optics. It begins with an overview of correlation measurements, starting with the Hanbury Brown and Twiss experiment, which introduces key principles for understanding photon correlations. We then explore the generation of entangled photonic states through nonlinear optics, a vital technique in quantum information science. The chapter also discusses the principles of quantum interference, including the operation of beam splitters, and introduces quantum walks. Finally, the photon detection technique used in our experiments is explained.

Chapter content:

2.1 Correlation measurements

Correlation measurements are used to analyze the statistical relationships between photons detected at different times or positions. These measurements help to characterize the nature of light, distinguishing between classical and quantum light sources. In quantum optics, correlation measurements are crucial for understanding photon statistics and quantum coherence. A key example is the Hanbury Brown and Twiss experiment, which measures intensity correlations to determine whether light exhibits random, bunching or antibunching behavior.

2.1.1 Hanbury Brown and Twiss experiment

The Hanbury Brown, and Twiss (HBT) interferometer (6) is based on the principle that the coherence of a beam of light is directly linked to its intensity fluctuations (3, 4, 37–39). Fig. 2.1 illustrates the fundamental concept of the HBT interferometer. When a coherent source of light is impinged upon a HBT interferometer, its coherence can be quantified via the intensity correlations measured at the two detectors, D_1 and D_2. In the original HBT experiment, they considered two light beams generated by independent sources on the disk of a star, with wave vectors denoted as $\bar{k}$ and $\bar{k'}$. The angle between the emitted light be ϕ. Assuming that the sources $\bar{k}$ and $\bar{k'}$ produce electric fields $E_k e^{i\bar{k}.\bar{r}}$ and $E_{k'} e^{i\bar{k'}.\bar{r}}$, respectively, the total amplitudes at $\bar{r_1}$ and $\bar{r_2}$ can be expressed as follows:

$$E(\bar{r_1}) = E_k e^{i\bar{k}.\bar{r_1}} + E_{k'} e^{i\bar{k'}.\bar{r_1}} \tag{2.1.1}$$

$$E(\bar{r_2}) = E_k e^{i\bar{k}.\bar{r_2}} + E_{k'} e^{i\bar{k'}.\bar{r_2}} \tag{2.1.2}$$

The intensities of the light beams at $\bar{r_1}$ and $\bar{r_2}$ can be measured with two detectors D_1 and D_2. The coherence between the signals, given by the second-order correlation function, can be described as:

$$C = \langle E^*(\bar{r_1}) E^*(\bar{r_2}) E(\bar{r_1}) E(\bar{r_2}) \rangle$$

$$C = \langle (|E_k|^2 + |E_{k'}|^2)^2 \rangle + 2\langle |E_k|^2 \rangle \langle |E_{k'}|^2 \rangle (1 + \cos(k r_0 \phi)) \tag{2.1.3}$$

where $k = |\bar{k}| = |\bar{k'}|$ and $r_0 = |\bar{r_1} - \bar{r_2}|$. r_0 is the magnitude of the vectorial distance between D_1 and D_2.

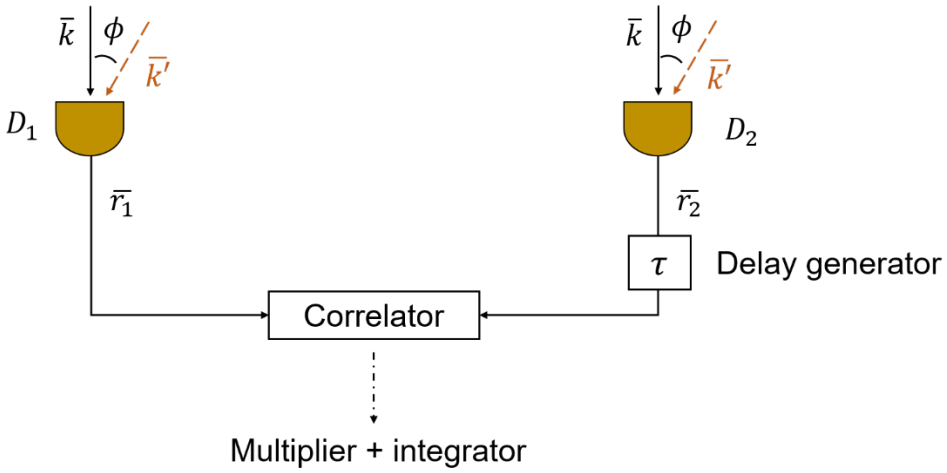

Fig. 2.1: **Schematic diagram of a HBT interferometer.** The wave vectors of the two rays are represented by $\bar{k}$ and $\bar{k}'$. The intensities of these rays are measured at positions, $\bar{r_1}$ and $\bar{r_2}$ using two detectors. The signals from the detectors are combined in an electronic correlator, which calculates the second-order correlation function.

By varying the separation of the detectors in the HBT interferometer, the angle between the two rays can be determined from the equations above. This angle allows to infer the size of the star. Since the intensity of each light is proportional to the number of photons, the correlation function can also be expressed in terms of the mean photon numbers and the angle between the rays.

$$C = \langle \hat{n}_k{}^2 \rangle + \langle \hat{n}_{k'}{}^2 \rangle + 2\langle \hat{n}_k \rangle \langle \hat{n}_{k'} \rangle (1 + \cos(k r_0 \phi)) \tag{2.1.4}$$

where $\langle \hat{n}_k \rangle$ and $\langle \hat{n}_{k'} \rangle$ are the mean photon number of the two lights (40).

The approach developed by Hanbury Brown and Twiss provided a means to determine the spatial coherence of the source through intensity correlations at different separations, r_0. However, it is important to note that the intensity interference effects are also influenced by the temporal coherence of the light and HBT measurement readily give the second-order correlation function. The temporal coherence, which is determined by the dynamics of the light-emitting atoms in the source, controls the fluctuations and correlations of the fields (5).

2.1.2 Second-order correlation function

Classical theory

Let us consider the statistical properties of the intensity fluctuations in chaotic light, in which fluctuations occur at a rapid pace, making direct observations challenging. Typically, measurements are obtained by averaging the intensity fluctuations over the response time of a detector. Here, we assume that ideal detectors are available with response time much shorter than the coherence time, τ_c, and this will enable instantaneous measurements of the intensity.

The average intensity, $\bar{I}(t)$, can be obtained by considering the statistical average over the distribution of phase angles. For a plane parallel light beam, the long-term average intensity is given by,

$$\bar{I}(t) \equiv \langle \bar{I}(t) \rangle = \frac{1}{2}\varepsilon_0 {E_0}^2 c \left\langle \left| \exp\left(i\phi_1(t)\right) + \exp\left(i\phi_2(t)\right) + \cdots + \exp(i\phi_\nu(t)) \right|^2 \right\rangle \quad (2.1.5)$$

where ν is the number of radiating atoms, ϕ_ν denotes the phase factors of each atom, E_0 is the amplitude of the electric field, $E(t)$, expressed as $E(t) = E_0 \exp(-i\omega_0 t)\{\exp\left(i\phi_1(t)\right) + \exp\left(i\phi_2(t)\right) + \cdots + \exp(i\phi_\nu(t))\}$ with ω_0 as the radiation frequency (5). By taking the average, the cross-terms between the phase factors cancel out, resulting in,

$$\bar{I}(t) \equiv \langle \bar{I}(t) \rangle = \frac{1}{2}\varepsilon_0 {E_0}^2 c\nu. \quad (2.1.6)$$

Thus, the variance of the average intensity, denoted as $(\Delta I)^2$, is given by,

$$(\Delta I)^2 = \langle \bar{I}(t)^2 \rangle - \langle \bar{I}(t) \rangle^2 = \bar{I}^2 \quad (2.1.7)$$

implying that the intensity fluctuation, ΔI, is dependent on the mean value, $\bar{I}$ (5).

Now, let us consider the case of two time measurements, where pairs of readings of the averaged intensity are taken with a fixed time delay, τ. The average of the product of each pair of readings gives us the intensity correlation function of light (5). The normalized form of this correlation function, known as the second-order temporal coherence, is defined as:

$$g^2(\tau) = \frac{\langle \bar{I}(t).\bar{I}(t+\tau) \rangle}{\bar{I}^2} = \frac{\langle E^*(t).E^*(t+\tau).E(t).E(t+\tau) \rangle}{\langle E^*(t).E(t) \rangle^2} \quad (2.1.8)$$

According to Cauchy's inequality, which applies to any pair of real numbers, the following relation holds for two measurements of the intensity at times t_1 and t_2:

$$2\bar{I}(t_1).\bar{I}(t_2) \leq \bar{I}(t_1)^2 + \bar{I}(t_2)^2 \quad (2.1.9)$$

Extending this inequality to N number of measurements,

$$\left\{\frac{\bar{I}(t_1)+\bar{I}(t_2)+\cdots+\bar{I}(t_N)}{N}\right\}^2 \leq \frac{\bar{I}(t_1)^2+\bar{I}(t_2)^2+\cdots+\bar{I}(t_N)^2}{N} \quad (2.1.10)$$

In terms of statistical average, this can be expressed as

$$\bar{I}^2 \equiv \langle \bar{I}(t) \rangle^2 \leq \langle \bar{I}(t)^2 \rangle \quad (2.1.11)$$

This implies that

$$1 \leq g^2(0). \quad (2.1.12)$$

Furthermore, considering the expression

$$\{\bar{I}(t_1)\bar{I}(t_1+\tau)+\cdots+\bar{I}(t_N)\bar{I}(t_N+\tau)\}^2 \leq \{\bar{I}(t_1)^2+\cdots+\bar{I}(t_N)^2\}\{\bar{I}(t_1+\tau)^2+\cdots+\bar{I}(t_N+\tau)^2\} \quad (2.1.13)$$

for a sufficiently long and numerous series of measurements, the two summations on the right-hand side become equal (5). Taking the square root of the above equation, we obtain:

$$\langle \bar{I}(t).\bar{I}(t+\tau) \rangle \leq \bar{I}(t)^2 \quad (2.1.14)$$

In terms of the correlation function, this can be expressed as

$$g^2(\tau) \leq g^2(0) \quad (2.1.15)$$

Therefore, the degree of second-order coherence can never exceed its value at zero time delay (5). This inequality applies to both stationary and non-stationary light beams in classical theory. The second-order electric field correlation function (Eq. 2.1.8), taking into account the contribution from each atom (i) can be approximated as

$$\langle E^*(t).E^*(t+\tau).E(t).E(t+\tau) \rangle = \nu^2\{\langle {E_i}^*(t)E_i(t) \rangle^2 + |\langle {E_i}^*(t)E_i(t+\tau) \rangle|^2\} \quad (2.1.16)$$

For large values of ν, this equation can be simplified to

$$g^2(\tau) = 1 + |g^1(\tau)|^2 \quad (2.1.17)$$

Where $g^1(\tau)$ is the first-order correlation function and its limiting value yields $g^2(0) = 2$ (5).

In contrast to chaotic beams, the electric field of a coherent wave (coherent at all space-time points), propagating in the z direction with wavevector $k = \frac{\omega}{c}$ is $E(z,t) = E_0 \exp(ikz - i\omega t + i\phi)$. Substituting the electric field in Eq. 2.1.8, we obtain $g^2(0) = 1$ for coherent light (5).

Quantum theory

One remarkable aspect of the theory of light is the significant agreement between the predictions of classical and quantum theory, despite their fundamental differences. Classical and quantum theories

provide identical predictions for interference effects and associated degrees of coherence in experiments involving coherent or chaotic light. However, phenomena that deviate from classical theory typically arise when non-classical light beams are used, which exhibit fluctuations and coherence properties that cannot be described classically. Many experiments demonstrating such phenomena can be expressed in terms of the components of the degree of second-order coherence, which play a crucial role in distinguishing between light beams that can or cannot be described by classical modes (5).

The degree of second-order coherence for single-mode light in the quantum regime can be defined as

$$g^2(\tau) = \frac{\langle \hat{a}^\dagger \hat{a}^\dagger \hat{a}\hat{a} \rangle}{\langle \hat{a}^\dagger \hat{a} \rangle} \tag{2.1.18}$$

where $\hat{a}^\dagger$ and $\hat{a}$ are creation and annihilation operators, respectively, with the properties

$$[\hat{a}, \hat{a}] = \left[\hat{a}^\dagger, \hat{a}^\dagger\right] = 0$$

$$\left[\hat{a}, \hat{a}^\dagger\right] = \hat{a}\hat{a}^\dagger - \hat{a}^\dagger\hat{a} = 1$$

$$\hat{a}^\dagger\hat{a} = \hat{n} \tag{2.1.19}$$

Where $\hat{n}$ is the number operator. Interestingly, Eq. 2.1.18 is independent of position and time, however it depends on the nature of a light beam. By using the properties of $\hat{a}^\dagger$ and $\hat{a}$, the degree of coherence can be expressed in terms of the mean and mean-square photon numbers as

$$g^2(\tau) = \frac{\langle n(n+1) \rangle}{\langle n \rangle} = \frac{\langle n^2 \rangle - \langle n \rangle}{\langle n \rangle^2} = 1 + \frac{\Delta n^2 - \langle n \rangle}{\langle n \rangle^2} \tag{2.1.20}$$

Thus, depending on the value of second-order correlation function, light can be classified as coherent, bunched, and antibunched (5).

In coherent light, the photodetector records a time-independent pair correlation function, resulting in a random stream of photocounts and an overall random distribution of photons (3, 5). On the other hand, high-intensity fluctuations or photon bunches in chaotic (bunched) light lead to closely spaced photo counts. This photon bunching effect is typically observed in the classical description of chaotic or thermal light. Conversely, in antibunched light, the succession of photo counts exhibits a significant spacing in the detection frequency.

Coherent light

The most commonly encountered single-mode states of light are represented by linear superpositions of number states, denoted as $|n\rangle$ (3). Among these states, the coherent state $|\alpha\rangle$ holds significant importance in practical applications of quantum theory. Coherent states exhibit quantum

properties that closely resemble those of classical electromagnetic waves, and a single-mode laser operating above threshold generates a coherent state excitation. A coherent state $|\alpha\rangle$ is given by the expression,

$$|\alpha\rangle = \exp\left(-\frac{1}{2}|\alpha|^2\right)\sum_{n=0}^{\infty}\frac{\alpha^n}{n!^{1/2}}|n\rangle. \tag{2.1.21}$$

For this state, the mean photon number squared is given by

$$\langle n\rangle^2 = \langle\alpha|\hat{n}^2|\alpha\rangle = |\alpha|^4 + |\alpha|^2 = \langle n\rangle^2 + \langle n\rangle \tag{2.1.22}$$

And the photon number variance, denoted by Δn^2, is

$$\Delta n^2 = |\alpha|^2 = \langle n\rangle \tag{2.1.23}$$

which arises due to the particle-like nature of light in the quantum theory (3). Additionally, the probability of finding n photons in the mode can be obtained as

$$P(n) = |\langle n|\alpha\rangle|^2 = \exp(-|\alpha|^2)\frac{|\alpha|^{2n}}{n!} \tag{2.1.24}$$

This probability distribution follows a Poissonian distribution. Also, the degree of second-order coherence for the coherent state, $|\alpha\rangle$, is given by (5):

$$g^2(\tau) = 1. \tag{2.1.25}$$

Bunched light

Let us now consider a chaotic light beam in an optical cavity, which is characterized by an uncertain phase and the inability to carry a coherent signal. The photon number probability of a single-mode chaotic light is given by

$$P(n) = \frac{\langle n\rangle^n}{(1+\langle n\rangle)^{1+n}} \tag{2.1.26}$$

And the photon number variance is given by

$$\Delta n^2 = \langle n\rangle^2 + \langle n\rangle. \tag{2.1.27}$$

The first term on the right-hand side represents fluctuations beyond those of coherent light, and its variance is equal to the mean photon number (5). This term corresponds to the wave contribution, while the second term represents the particle analogue in classical theory. It is important to note that light with a photon number variance exceeding the mean photon number, such as chaotic light, exhibits super-Poissonian fluctuations (5). From the above equations, for bunched light, the degree of second-order coherence is

$$g^2(\tau) = 2. \tag{2.1.28}$$

Antibunched light

In antibunched light, the photons are emitted with regular gaps between them, as opposed to random spacing. This is depicted in Fig. 2.2 c). If the flow is regular, then there will be long time intervals between observing photon counting events. In this case, there are longer time intervals between consecutive photon counts. As a result, the probability of detecting a photon on a detector is small for small values of τ and increases with τ. The degree of second order coherence for such light sources satisfies the inequality (5)

$$g^2(\tau) > g^2(0). \tag{2.1.29}$$

An example for such light sources exhibiting antibunching is resonance fluorescence by a single atom, where the time delays between successive photons arise due to atomic recovery between emissions. Additionally, photon antibunching is a significant phenomenon in the quantum theory of light, as it is a purely quantum effect without a classical counterpart. This non-classical effect is distinct from sub-poissonian statistics, which is identified by the condition (5)

$$g^2(0) < 1. \tag{2.1.30}$$

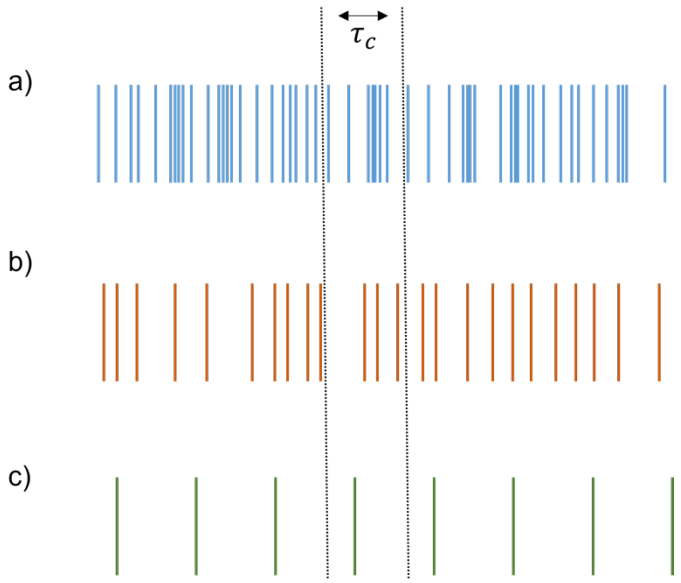

Fig. 2.2: **Comparison of various photon streams.** a) Bunched light (Chaotic light): In this case, the photons arrive in a clustered manner with high-intensity fluctuations. The correlation between photon arrival times is relatively strong, resulting in closely spaced photo counts. This type of light is commonly associated with chaotic or thermal sources., b) Coherent light: Coherent light exhibits random arrival times of photons. The correlation between the arrival times is weak, leading to a random distribution of photo counts. This type of light is characteristic of sources with good temporal coherence, such as lasers. c) Antibunched light (single-photon regime). In the case of antibunched light, the photon stream shows a significant spacing between successive photo counts. This phenomenon occurs in the single-photon regimes and implies that the probability of detecting two photons at the same time is exceptionally low. The coherence time of the light, $\boldsymbol{\tau_c}$, represents the characteristic timescale over which the temporal coherence of the light persists **(5)**.

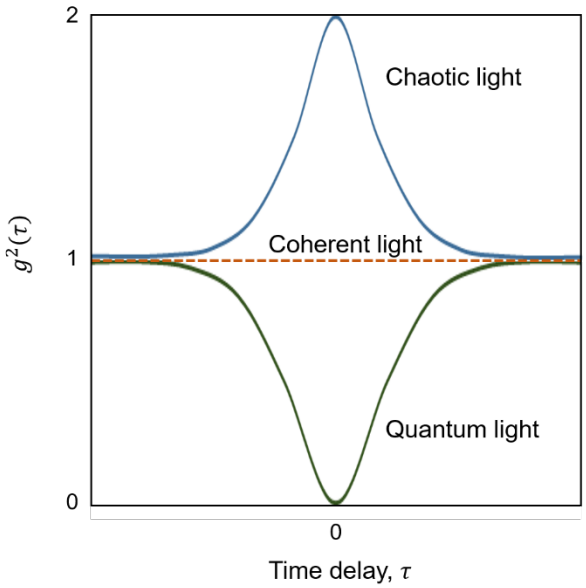

Fig. 2.3: **Second-order correlation function, $g^2(\tau)$ for various classifications of light.** The blue curve represents bunched (chaotic), the dashed maroon curve corresponds to random (coherent) light and the green curve corresponds to antibunched (quantum) light.

2.2 Generation of entangled photonic states using nonlinear optics

Nonlinear optics, which occurs as a consequence of the modification of the optical properties of a material system in the presence of external electric field, embraces a wide variety of phenomena and it forms an extensive field of study (41). When an intense electric field travels through a dielectric medium, its electric field induces a dipole moment to the atoms in the path of the radiation causing a displacement of the electron cloud with respect to the positive charged core. In the case of conventional (i.e., linear) optics, the induced polarization ($\vec{P}(t)$) depends linearly on the electric field strength ($\vec{E}(t)$) described by,

$$\vec{P}(t) = \epsilon_0 \chi^{(1)} \vec{E}(t) \tag{2.2.1}$$

where ϵ_0 and $\chi^{(1)}$ are the permittivity of free space and linear susceptibility, respectively. At low electric field strengths, the dipoles oscillate with the frequency of the incoming electric field, thus, the material will not alter the frequency of the electric field. In addition, material properties such as refractive index or absorption coefficient are independent of the light intensity.

However, as the electric field strength increases, the dipoles lose their equilibrium and oscillate with different frequencies giving rise to nonlinear processes. The resultant nonlinear optical response is expressed in terms of the polarization density as:

$$\vec{P}(t) = \epsilon_0\left(\chi^{(1)}\vec{E}(t) + \chi^{(2)}\vec{E}^2(t) + \chi^{(3)}\vec{E}^3(t) + \cdots\right) = \vec{P}_L(t) + \vec{P}_{NL}(t) \tag{2.2.2}$$

where $\vec{P}_L(t)$ and $\vec{P}_{NL}(t)$ represent the linear and nonlinear terms, respectively. The nonlinear polarization, represented as

$$\vec{P}_{NL}(t) = \epsilon_0\left(\chi^{(2)}\vec{E}^2(t) + \chi^{(3)}\vec{E}^3(t) + \cdots\right), \tag{2.2.3}$$

consists of the second- ($\chi^{(2)}$) and third- ($\chi^{(3)}$) order nonlinear optical susceptibilities that govern the nonlinear processes involving three and four fields, respectively. $\chi^{(2)}$ interactions occur in non-centrosymmetric crystals, that is, media that do not display inversion symmetry. If the electric field of the incident light contains two distinct frequency components, ω_1 and ω_2, as described as $\overrightarrow{E_1} = \vec{E}(\omega_1)\exp(-i\omega_1 t) + c.c.$ and $\overrightarrow{E_2} = \vec{E}(\omega_2)\exp(-i\omega_2 t)$, respectively, the resultant second-order term in Eq. 2.2.3 can be described as $\vec{P}_{NL}{}^{(2)}(t) = \chi^{(2)}\overrightarrow{E_1}\overrightarrow{E_2}$. This gives rise to three nonlinear processes, namely, sum- (SFG) and difference- frequency generation (DFG) as well as second harmonic generation (SHG) process governed by the frequency components $\omega_1 + \omega_2$, $\omega_1 - \omega_2$, and 2ω (when $\omega_1 = \omega_2$), respectively. Additionally, the nonlinear susceptibility depends on the polarization vectors of the field components and on the direction of the induced polarization. Therefore, $\chi^{(2)}$ in bulk media is described by a function of two

frequencies and three spatial directions (5, 41). In nonlinear waveguided systems, the spatial dependency of $\chi^{(2)}$ is restricted to the propagation axis of the waveguide due to confinement (42).

Fig. 2.4 (a) demonstrates the generalized schematic involving three fields that describe a typical classical nonlinear optical process of SHG. This requires the two stringent requirements to be met: i) Energy conservation – this dictates that the total energy within the system is preserved, implying $\sum E_{input} = \sum E_{output}$. In the standard notation, field interaction can be described as $\hbar\omega_1 + \hbar\omega_2 = \hbar\omega_3$, where $\omega_1 = \omega_2 = \omega$ provides the degeneracy condition for second harmonic generation, given by $\omega_3 = 2\omega$ and $\hbar = \frac{h}{2\pi}$, where h is the Planck's constant. ii) Momentum conservation – this dictates that the momentum of the interacting fields must be matched given by $k_1 + k_2 = k_3$, where $k_i = \frac{2\pi n_i}{\lambda_i}$ is the wave vector of the interacting fields within the crystal (2, 5, 41). When fields propagate within a nonlinear medium, a phase mismatch arises due to group velocity dispersion of the different fields. This phase mismatch results in the nonlinearly generated light to destructively interfere with itself, resulting in the failure to generate upconverted light (see Fig. 2.5 (b)). A possible way to circumvent this problem is to utilize anomalous dispersion, where the refractive index decreases with increasing frequency by means of quasi-phase-matching utilizing a periodically poled material (Fig. 2.5 (a)).

Periodically poled lithium niobate (PPLN) is a highly efficient nonlinear medium that exploits the second-order susceptibility term $\chi^{(2)}$ to enable nonlinear processes between interacting fields, giving access to a wide range of frequency conversion processes including SHG, SFG, and DFG (41, 43). This is made possible by the versatility of the PPLN optical properties in terms of its transparency window, high refractive index, phase matching scheme mature fabrication technologies, etc. (44, 45). The nonlinear process occurring within PPLN can be dictated by quasi phase-matching, i.e., engineering via periodic poling of the lithium niobate crystal. Furthermore, the quasi-phase matching in PPLN waveguides gives access to tailorable polarization properties of the interacting fields, namely type-0, type-1, and type-2 processes. Type-0 interactions involve fields having identical polarizations. The most dominant interaction in PPLN occurs when two V-polarized fields interact to generate a V-polarized output during second harmonic and sum-frequency generation processes. On the other hand, type-1 interactions involve fields with the same polarization as the input to generate an orthogonally polarized output, and type-2 processes involve two orthogonal input fields.

Such second-order nonlinear processes can also be enabled in the in the quantum domain, given by the process known as spontaneous parametric down conversion (SPDC). Here, the nonlinear interaction occurs when a pump photon of energy ω_p decays spontaneously to generate twin photons, signal and idler with energies ω_s and ω_i, respectively, as shown if Fig. 2.4 b (top). Like second-order classical frequency

conversion processes, the SPDC process necessitates the conservation of energy and momentum. In this case, $E_p = E_s + E_i$ and $k_p = k_s + k_i + k_G$ defines the energy (see Fig. 2.4 b (bottom)) and momentum conservation laws, respectively, where k_G is the momentum vector associated with the poling of PPLN waveguide. This gives rise to interesting quantum properties, specifically, the energy-time correlations between the twin photons. Furthermore, materials like PPLN allows for type-0 and type-2 interactions, giving access to polarization-dependent non-classical correlations (44, 46). Such correlations forms the basis for entanglement generation across various photonic degrees of freedom such as frequency, time, polarization, and path (12, 13, 147, 148).

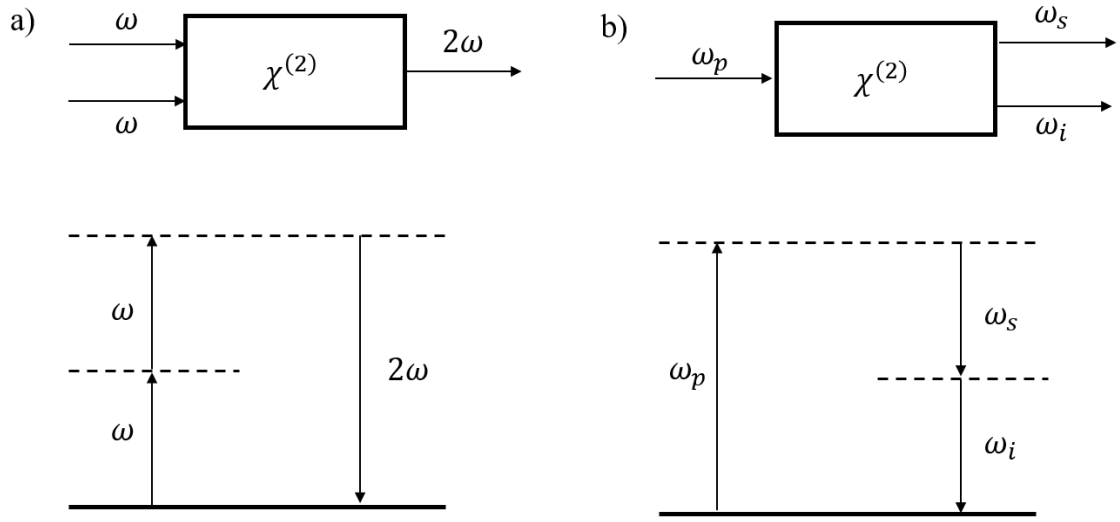

Fig. 2.4: **Second harmonic generation and spontaneous parametric down conversion.** a) Geometry and energy-level diagram describing second harmonic generation. b) Geometry and energy-level diagram describing spontaneous parametric down conversion**.**

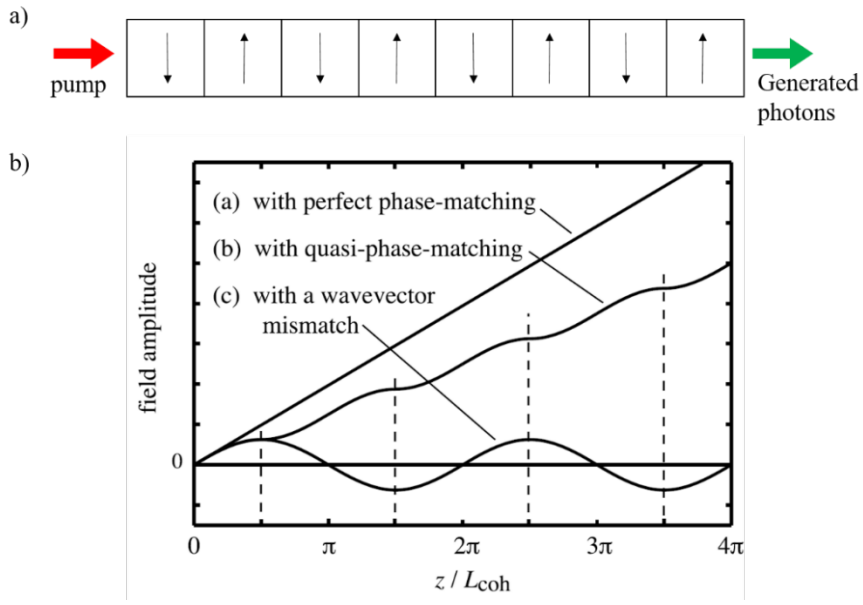

Fig. 2.5: **PPLN waveguide.** a) Schematic representation of a PPLN in which the positive c axis alternates in orientation with a certain period. b) Comparing the field amplitude of the generated wave in a nonlinear optical interaction under three different phase-matching conditions in relation to spatial variation. Reproduced from **(41)** with permission from Springer Nature, © 2023 Springer Nature.

2.3 Quantum interference

Quantum interference arises from the coherent superposition of probability amplitudes corresponding to indistinguishable quantum processes. This phenomenon is fundamental to various quantum technologies, including quantum computing, quantum communication, and precision metrology, where it enables the manipulation and control of quantum states with high fidelity.

2.3.1 Beam splitter operation

A beam splitter is one of the most fundamental building blocks of interferometers. It has two inputs (*a* and *b*) and two outputs (*c* and *d*) as shown in Fig. 2.6 (a). In the classical regime, when a light beam is incident on a beam splitter either at ports *a* or *b*, the beam splitter divides the intensity into reflected and transmitted components through the two output ports *c* and *d,* respectively. The proportion at which this splitting occurs depends on the complex parameters, reflectance, r, and transmittance, t. When a balanced beam splitter is considered, the beam-splitting operation is dictated by $|r| = |t| = \frac{1}{\sqrt{2}}$, representing a 50-50 beam splitting operation. However, in the non-classical realm, a quantum description of a beam splitter proves to be the most effective as it elucidate fundamental concepts of quantum superposition and randomness through the statistical behavior of photons (48, 49).

The quantum description of a beam splitter, in the second quantization formalism, can be represented by employing a set of bosonic annihilation and creation operators, $\hat{a}_i$ and $\hat{a}_i{}^{\dagger}$, respectively, to represent the input and output photonic modes (5). These operators satisfy the commutation relation $[\hat{a}_i, \hat{a}_j{}^{\dagger}] = \delta_{i,j}$. Let us use the notations, $\hat{a}$, $\hat{b}$, $\hat{c}$, and $\hat{d}$ to represent annihilation operators for the beam splitter ports *a*, *b*, *c* and *d*, respectively. The 50-50 operation of the beam splitter, also known as the Fourier operation, is given by (50, 51):

$$\hat{a} = \frac{1}{\sqrt{2}}(\hat{c} + \hat{d}) \tag{2.3.1}$$

$$\hat{b} = \frac{1}{\sqrt{2}}(\hat{c} - \hat{d}). \tag{2.3.2}$$

2.3.2 Quantum interference measurements

In two-photon interference experiments, the photons (1 and 2) are directed through two alternative pathways, *a* and *b* (acquiring a phase difference of ϕ), of the beam splitter. Subsequently, the photons are combined, and the resulting interference fringes are observed by measuring the coincidence count rates with two detectors at the output ports (*c* and *d*) at each phase values.

The initial state at the beam splitter can be written as

$$|\psi\rangle = |1\rangle_a|2\rangle_b = \hat{a}^\dagger{}_1\hat{b}^\dagger{}_2|0\rangle \tag{2.3.3}$$

where $\hat{a}^\dagger{}_1$ and $\hat{b}^\dagger{}_2$ are the creation operators of photons, 1 and 2, at ports *a* and *b* of the beam splitter, respectively. The output state of the beam splitter (i.e., after photons interfere) is given by the following transformation:

$$\begin{aligned}\hat{a}^\dagger{}_1\hat{b}^\dagger{}_2|0\rangle \rightarrow \frac{1}{2}\left(\hat{c}^\dagger{}_1 + \hat{d}^\dagger{}_1\right)\left(\hat{c}^\dagger{}_2 - \hat{d}^\dagger{}_2\right)|0\rangle \\ = \tfrac{1}{2}\left(\hat{c}^\dagger{}_1\hat{c}^\dagger{}_2 - \hat{c}^\dagger{}_1\hat{d}^\dagger{}_2 + \hat{c}^\dagger{}_2\hat{d}^\dagger{}_1 - \hat{d}^\dagger{}_1\hat{d}^\dagger{}_2\right)|0\rangle\end{aligned} \tag{2.3.4}$$

where $\hat{c}^\dagger{}_1$ and $\hat{c}^\dagger{}_2$ are the creation operators at the output port c, while $\hat{d}^\dagger{}_1$ and $\hat{d}^\dagger{}_2$ are the creation operators at the output port d, after the beam splitter interaction. This results in four possibilities when two photons interact at the input of a beam splitter, as shown in Fig. 2.6. The output terms $\hat{c}^\dagger{}_1\hat{c}^\dagger{}_2$ and $\hat{d}^\dagger{}_1\hat{d}^\dagger{}_2$ indicate that both photons leave the beam splitter through the same output, i.e., either *c* or *d*, respectively (50–52), while $\hat{c}^\dagger{}_1\hat{d}^\dagger{}_2$ and $\hat{c}^\dagger{}_2\hat{d}^\dagger{}_1$ depict that both photons exit at different outputs of the beam splitter. Considering a balanced beam splitter configuration, each of these output terms have the same probability of occurrence, i.e., 25%. For instance, for a two-photon entangled state, the two-photon detection probabilities at the output ports of a beam splitter are given by:

$$P_{c_1c_2} = \tfrac{1+\cos 2\phi}{4},\ P_{c_1d_2} = \tfrac{1+\cos 2\phi}{4},\ P_{c_2d_1} = \tfrac{1-\cos 2\phi}{4},\ \text{and}\ P_{d_1d_2} = \tfrac{1-\cos 2\phi}{4}$$

Here, the subscripts correspond to the four interaction possibilities as given in Eq. 2.3.4.

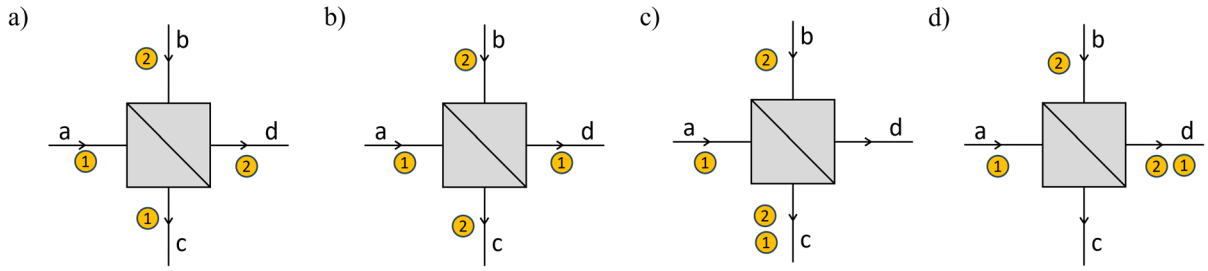

Fig. 2.6: **Operation of a beam splitter.** Illustration of four possible ways photons 1 and 2 can interact in a beam splitter and their corresponding output modes. a) and b) In casual configuration where a and b are the inputs and c and d are the outputs. c) and d) represent the HOM effect, where indistinguishable photons entering from both sides of the beam splitter interfere and will go out along the same direction. Therefore, there will be two photons in one of the two outputs of the beam splitter.

Interestingly, when we consider the specific case of interference between two indistinguishable (identical) photons, the above equation reduces to,

$$\hat{a}^\dagger \hat{b}^\dagger |0\rangle \rightarrow \frac{1}{2}\left(\hat{c}^\dagger \hat{c}^\dagger - \cancel{\hat{c}^\dagger \hat{d}^\dagger} + \cancel{\hat{c}^\dagger \hat{d}^\dagger} - \hat{d}^\dagger \hat{d}^\dagger\right)|0\rangle$$

$$= \frac{1}{2}\left(\left(\hat{c}^\dagger\right)^2 - \left(\hat{d}^\dagger\right)^2\right)|0\rangle$$

$$= \frac{1}{\sqrt{2}}(|2\rangle_c - |2\rangle_d) \qquad (2.3.5)$$

The final equation is obtained from the general equation, $\left(\hat{a}^\dagger\right)^n |0\rangle = \sqrt{n!}\,|n\rangle$. In this case, the two photons take output *c* or *d* showing a bunching effect due to bosonic character of photons. This kind of interference, giving ideally zero coincidences at zero delay/phase difference, i.e., when temporal indistinguishability of the photons are achieved, is called Hong-Ou-Mandel (HOM) interference (Fig. 2.7) (53). The theoretical and experimental work demonstrated by Hong, Ou, and Mandel outlines the occurrence of a dip in coincidence detections at the output of a MZI, when indistinguishable photons are passed through the inputs of MZI for various delays/phase values (Fig. 2.7) (53). HOM effect is truly quantum mechanical in nature and has no classical analogue, thereby providing a distinct advantage to outperform classical computations, securely communicate information, simulate highly complex physical systems and increase sensitivity of precise measurements (51, 53). However, in the case of fermions, the creation operators anti-commute, implying $\hat{c}^\dagger \hat{d}^\dagger = -\hat{d}^\dagger \hat{c}^\dagger$, causing fermions to exit through different output ports (51, 54).

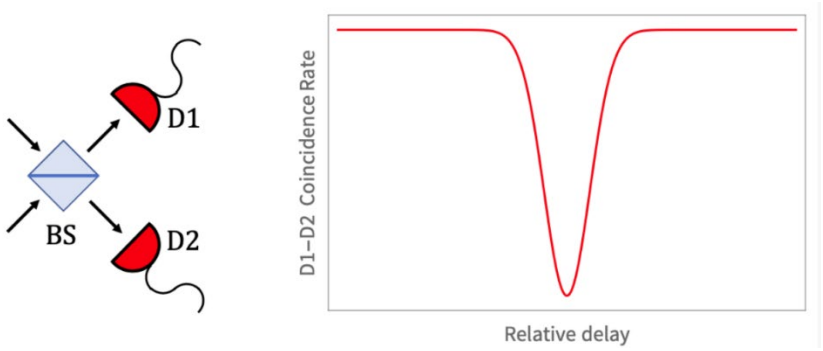

Fig. 2.7: **Illustration of the Hong-Ou-Mandel effect.** When two identical photons are passed through two inputs of the beam splitter, the photons show bunched behavior and exit through one of the output ports of the beam splitter. The coincidence graph plotted for various delays is given on the right side. At zero delay, the coincidence between the detectors D1 and D2 is zero, resulting in HOM interference. Reproduced from **(55)** under the CC BY 4.0 license.

2.4 Quantum walk

Quantum walks (56, 57) are the quantum mechanical counterparts of classical random walks, where the evolution is governed by quantum superposition and interference effects. Quantum walks have found applications in diverse fields such as quantum computation (58–60), topological phases (61), and quantum simulation (62). A quantum walk comprises two essential components: a walker and an environment that serves as a processing platform for the walker. Atoms, ions, photons, and quasi-particles like excitons are potential walkers (63), capable of exhibiting a wave-like propagation in the quantum environment.

A quantum walk essentially include the integration of the actual detection process into the theory involving correlating each potential shift with another degree of freedom, serving as a quantum coin (56). Consider the evolution of a two-level quantum state $|c\rangle$ with basis $\{|\updownarrow\rangle, |\leftrightarrow\rangle\}$ (56). When the walker is in the state $|\leftrightarrow\rangle$, it takes one direction and when the walker is in the state $|\updownarrow\rangle$, it takes the opposite direction. Thus, the internal state can exist in superposition of both states, $|c\rangle = \alpha_1|\updownarrow\rangle + \alpha_2|\leftrightarrow\rangle$. Moreover, the final probability distribution of the walker (after a large number of iterations) in a quantum walk can be predicted by utilizing its wave function. When the walker is in the initial state $|\leftrightarrow\rangle$, its evolution demonstrates an asymmetrical probability distribution, where the walker's final position is more likely to reside in one direction (Fig. 2.8 (a)); and similarly, when the walker is in the state $|\updownarrow\rangle$, it shows a higher probability of occupying the opposite direction. However, if the walker's initial state exists in a superposition of both bases given by $|c\rangle = \alpha_1|\updownarrow\rangle + \alpha_2|\leftrightarrow\rangle$, its probability distribution spreads in both directions leading to a superposition of the wave function in position space (Fig. 2.8 (b)).

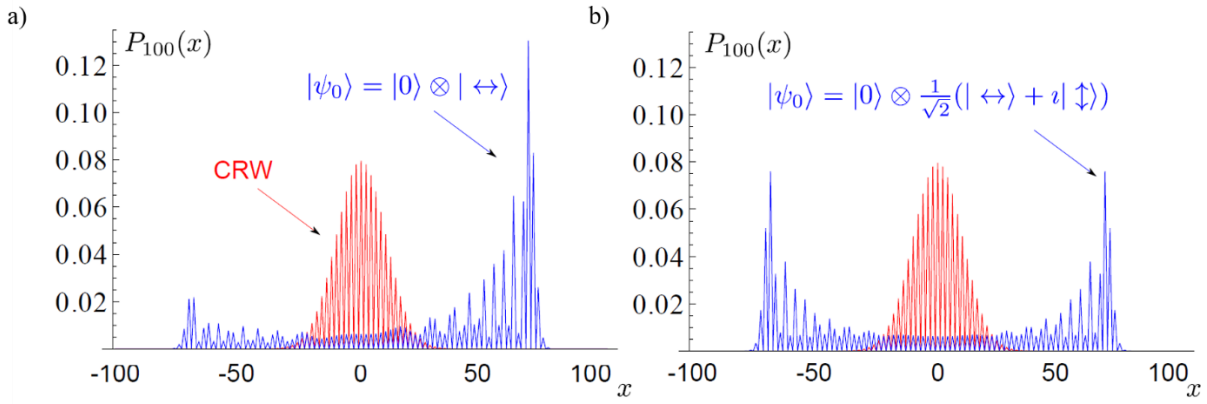

Fig. 2.8: **Probability distribution.** An example that presents a comparison between the probability distributions for quantum walks (blue) and a classical random walk (red) after 100 steps. a) The asymmetric probability distribution due to asymmetric initial state. b) The symmetric probability distribution due to symmetric initial state. Reproduced from **(63)** under the CC BY-NC-ND 3.0 license.

There are three key properties that distinguish quantum walks: firstly, the quantum walker explores all feasible paths simultaneously, resulting in an accelerated spread of the probability distribution of the

walker (64). Secondly, in a quantum walk, the quantum coin and the movement of the walker are unitary transformations, which ensures that the quantum walk process is reversible (64, 65). Thirdly, unlike classical random walks where randomness arises from transitions between states, quantum walk randomness stems solely from measurement operations on the quantum system (64). These unique properties have enabled the development of quantum algorithms known as probabilistic algorithms (66). In these algorithms, the quantum system exists in a distribution across various states, each with a specific probability, therefore the evolution of the system can be predetermined (66). Also, with knowledge of the initial quantum state distribution and the state transition matrix, the distribution after a certain time evolution can be calculated theoretically (66). Apart from quantum algorithms, quantum walks also find several applications in the field of quantum communication (67), computation (68) and other quantum information technologies (57, 64, 69).

One-dimensional discrete-time quantum walk

There are two types of quantum walks: 1) discrete-time quantum walk (DTQW) and 2) continuous-time quantum walk (CTQW) (57). DTQW employs a discrete quantum coin which governs the operations performed on the walker during its propagation, while CTQW involves the continuous transition of the walker without the help of a quantum coin (57). This thesis focuses solely on DTQW, and CTQW is beyond its scope.

The wave function of a walker, $|\psi\rangle = \sum_x \sum_c A_{x,c} |x\rangle \otimes |c\rangle$, where $A_{x,c} \in \mathbb{C}$ denotes the complex amplitude of the wave function, is a vector in a complex vector space called the Hilbert space, $\mathcal{H}$, (2) and the quantum walk is dictated by $\mathcal{H} = \mathcal{H}_x \otimes \mathcal{H}_c$, where $\mathcal{H}_x$ and $\mathcal{H}_c$ are the Hilbert spaces of the position space ($|x\rangle$) and the quantum coin ($|c\rangle$), respectively. In DTQW, the evolution of the quantum walk is described in discrete steps by two unitary operations given by the coin ($\hat{C}$) and the shift operators ($\hat{S}$) (63, 70). The $\hat{C}$ impacts the internal state of the walker, such as spin of an electron or polarization of a photon, while the $\hat{S}$ moves the walker to a nearby site or lattice position.

For the general mathematical description of a one-dimensional DTQW (71, 72), we first initialize the quantum walker at the position state $|0\rangle$ with the coin state $|\updownarrow\rangle$.

$$|\psi_0\rangle = |0\rangle \otimes |\updownarrow\rangle \tag{2.4.1}$$

The bases of the quantum coin state can be written in the matrix form as $|\updownarrow\rangle = \begin{pmatrix}1\\0\end{pmatrix}$ and $|\leftrightarrow\rangle = \begin{pmatrix}0\\1\end{pmatrix}$, representing a two-level quantum system. The coin operation on the walker, denoted as $\mathbb{I} \otimes \hat{C}$, transforms the initial coin state of the walker, but not its position state. The quantum coin operation can be represented as,

$$\hat{C} = \begin{pmatrix} e^{i(\phi_1+\phi_2)}cos\alpha & e^{i\phi_1}sin\alpha \\ e^{i\phi_2}sin\alpha & -cos\alpha \end{pmatrix} \tag{2.4.2}$$

where $\phi_{1,2}$ are the phases of the walker and α is the rotation parameter (63). When $\phi_1 = \phi_2 = 0$ and $\alpha = \frac{\pi}{4}$, it becomes the Hadamard coin $\hat{C}_H$. The Hadamard operation transforms each of the coin basis states into an equal superposition state, making it highly similar to a classical coin toss with a balanced coin. This operation can be expressed as follows:

$$\hat{C}_H|\updownarrow\rangle = \frac{1}{\sqrt{2}}(|\updownarrow\rangle + |\leftrightarrow\rangle)$$

$$\hat{C}_H|\leftrightarrow\rangle = \tfrac{1}{\sqrt{2}}(|\updownarrow\rangle - |\leftrightarrow\rangle). \tag{2.4.3}$$

Applying the coin operation to our initial state we obtain,

$$\mathbb{I} \otimes \hat{C}|\psi_0\rangle = |0\rangle \otimes \tfrac{1}{\sqrt{2}}(|\updownarrow\rangle + |\leftrightarrow\rangle). \tag{2.4.4}$$

After the coin operation, the next step is to perform the shift operation, which moves the walker along the lattice positions defined by the quantum environment or platform. The shift operator performs the following one-dimensional propagation,

$$\hat{S} = \sum_x |x+1\rangle\langle x| \otimes |\leftrightarrow\rangle\langle\leftrightarrow| + |x-1\rangle\langle x| \otimes |\updownarrow\rangle\langle\updownarrow| \tag{2.4.5}$$

This means that the shift operator moves a particle that resides at x either to $x-1$ or $x+1$ in accordance with the coin state, i.e., $|\updownarrow\rangle$ or $|\leftrightarrow\rangle$, respectively.

The complete evolution of a quantum walker after n steps is given by a consecutive iteration of, $\hat{C}$ and $\hat{S}$ applied to the initial state $|\psi_0\rangle$. This is expressed through the evolution operator, $\hat{U} = \left(\hat{S}\hat{C}\right)^n$ and the final state is then given by,

$$|\psi_n\rangle = \left(\hat{U}\right)^n|\psi_0\rangle = \left(\hat{S}\hat{C}\right)^n|\psi_0\rangle. \tag{2.4.6}$$

Several numerical, analytical, and experimental findings have greatly enriched and solidified the field of DTQW. Shikano et al. (73) proposed employing DTQW as a tool for exploring quantum foundations, presenting an analytical expression for the limit distribution of DTQW with periodic position measurements and delved into the concept of randomness. Kurzynski and Wójcik (74) demonstrated the feasibility of quantum state transfer in DTQWs by introducing position-dependent coins. Stang et al. (75) introduced a history-dependent DTQW, incorporating memory effects into the walk's evolution, and proposed a correlation function to measure such effects. Additionally, DTQWs have been harnessed for entanglement generation. Chandrashekhar (76) proposed leveraging entanglement generated during DTQW

execution as a resource for entangling spatially-separated systems. Allés et al. (77) introduced a shift operator for DTQW involving two walkers, offering conditions for maximal entanglement generation, albeit with a low degree of probability. Moreover, DTQWs find application in quantum metrology, as demonstrated by Annabestani et al. (69), who showcased its potential as a probe in multi-parameter estimation studies. Thus, DTQWs serve as a versatile framework for studying quantum dynamics, leveraging superposition and interference to explore fundamental and applied quantum phenomena.

2.5 Photon detection

Single photon detection plays a crucial role in photonic quantum technologies by enabling high-accuracy and high-efficiency measurement, as well as the study of individual photon properties. There are several types of single photon detectors available, each with its own strengths and limitations. These include avalanche photodiodes, photomultiplier tubes, and superconducting nanowire single photon detectors (SNSPDs).

Among these, SNSPDs are the most promising technology in the field of quantum optics and high-speed optical communications. These detectors operate by applying a DC bias current slightly below a threshold switching current. When a photon is absorbed, the nanowire switches from a low-resistance superconducting state to a high-resistance non-superconducting state, resulting in a rapid increase in the output voltage. The detector then recovers during a dead-time before it is ready to detect another photon. SNSPDs require stable electronic biasing and low-noise amplification for efficient performance.

The projects described in the thesis have utilized SNSPDs with 90 ± 5 % detection efficiency, 1 kHz dark count rate, and 80 ns dead time (Quantum Opus, Opus1). When a single photon is detected, both systems generate an electronic pulse that is sent to precise timing electronics (a time-to-digital converter, TDC), which allocates a time-tag (i.e., the measurement time) to each detection event (PicoQuant, HydraHarp400). While the resolution of the TDC is 1 ps, the timing accuracy of the full system is lower due to timing jitter of the detectors and their electronics.

By saving a time-tag for each event, it becomes possible to perform different types of post-processing. In each measurement, the photons are sent to two different single photon detectors either using beam splitters (nanolaser output, see chapter 3) or frequency filters (time-bin entangled states, see chapter 4). The events for each detector are gathered on a different channel of the TDC. After collecting data for a long period of time (15 minutes for nanolaser output, see chapter 3 and 15 minutes each for time-bin entangled photons, see chapter 4), the arrival times of multiple single photon detection events were collected and sorted to build up a histogram over different relative arrival times (between two photons, or a single photon event and a trigger). This histogram can then be used to characterize the temporal waveform or to extract information about

a) The emission characteristics of a light source.
b) The purity of entangled states, and to assess the efficiency of the quantum system in processing those states.

3 CHARACTERIZATION OF METALLIC COAXIAL NANOLASER

Chapter abstract:

In this chapter, we delve into the realm of application of photon statistics for the characterization of nanolaser cavities. Reduced cavity sizes relative to the emission wavelength give rise to unique physical phenomena known as cavity quantum electrodynamics effects, stemming from the interaction between matter and electromagnetic fields in subwavelength structures (32). These effects lead to the generation of coherent radiation, due to the quantum electrodynamic properties inherent to small volumes. These devices hold great potential for various future applications, including on-chip optical communication, ultrahigh resolution imaging, sensing, and spectroscopy (32, 78).

The chapter starts with an overview, covering the background, the issue addressed, and the proposed solutions. Subsequently, we expound on the fundamental principles underlying the project and the experimental methods employed. Then, we present and discuss the results obtained and then summarize the chapter.

Chapter content:

3.1 Overview

The progress and functioning of modern society heavily rely on the continuous advancement of information generation, transmission, reception, and processing. While electronic devices with complex integrated circuits have played a crucial role in this advancement, they do have limitations, notably in the form of thermal issues and resistor-capacitor (RC) time delays (79). In response, photonic devices and circuits are seen as a promising complement to, and potentially a replacement for, electronic circuits. Moreover, as the field of microelectronics has experienced exponential growth in the number of transistors per chip, known as Moore's law, with the number doubling approximately every two years over the past four decades (80), photonics has also witnessed progress, although it is still in its early stages. For example, Fig. 3.1 illustrates the development of complexity in InP-based photonic integrated circuits, measured by the number of integrated components on a single chip.

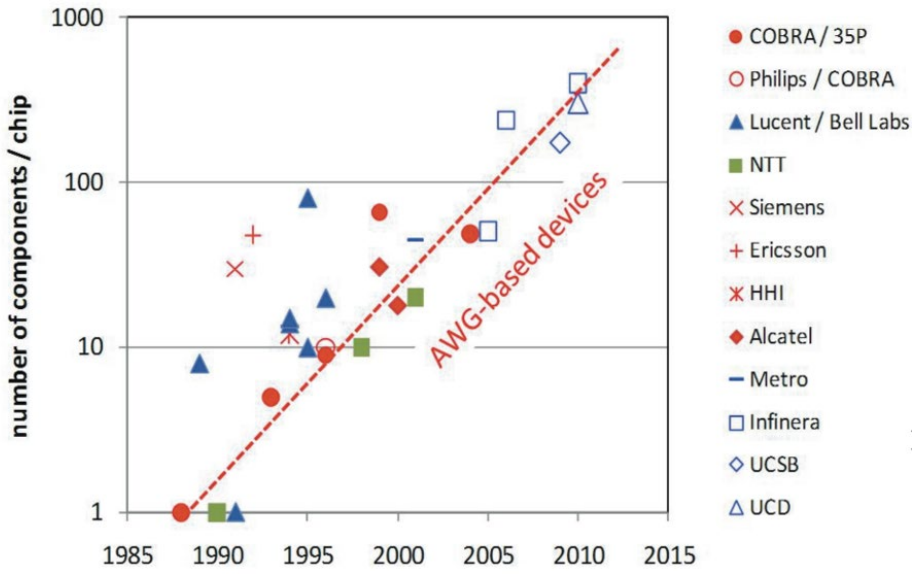

Fig. 3.1: **The progression of chip complexity over time, quantified by the number of components integrated per chip.** AWG in the figure stands for Arrayed waveguide grating. Reproduced from **(81)** with permission from John Wiley and Sons, © 2011 John Wiley and Sons.

For any photonic system, light sources, such as lasers, are the fundamental element. Similarly to the first transistors, early lasers were macroscopic devices occupying a significant physical footprint ranging from centimeters to decimeters. When the size of an electromagnetic cavity is reduced relative to the emission wavelength, fascinating physical phenomena, specific to such cavities, emerge. Early experiments conducted in the radio and microwave frequencies demonstrated the Purcell effect, where the spontaneous emission rate of atoms within a cavity could be either enhanced or inhibited compared to their emission

rate in free space (82). This change in the spontaneous emission rate was found to be influenced by the cavity's geometry in addition to the orientation and spectra of the atoms (82).

In the 1990s, the concept of the Purcell effect, which had been only observed in the radio and microwave domains, was extended to the optical regime. Experiments were conducted on dyes and semiconductors placed in optical micro-cavities, revealing modified spontaneous emission rates (83–86). The Purcell effect has since found significant applications, including diode lasers with improved modulation bandwidth (87–89), enhanced energy efficiency (90, 91), and thresholdless lasing (34, 92). Moreover, the observation of the Purcell effect in semiconductor cavities has resulted in demonstrating lasing in various wavelength and sub-wavelength scale structures.

Laser miniaturization

The process of laser miniaturization began with the introduction of solid-state laser diodes (93), which reduced device sizes from meters to millimeters. Subsequent advancements led to the development of vertical-cavity surface-emitting lasers (VCSELs) (94), further reducing the size to tens of micrometers. Additionally, micro-scale whispering-gallery mode (WGM) lasers have been achieved using micro-pillars/disks (95, 96) and micro-spheres (97). In parallel, efforts have been made to miniaturize the optical modes using 2D photonic crystals in laser designs (98). Fig. 3.2 illustrates the timeline of laser miniaturization progress over the last few decades.

A desirable nanolaser must exhibit subwavelength dimensions in all three directions, both in its physical size and the confinement of its optical mode. Such devices are crucial for various practical applications, including highly integrated chip-scale photonic circuits, displays, and sensors. However, the majority of dielectric laser cavities fail to meet this criterion due to their large physical footprint or mode volume. For instance, micro-disk lasers with diameters smaller than the free-space emission wavelength exist, however, they suffer from poor mode confinement, making it impractical to pack a large number of such lasers with dielectric cavities in a small region (99, 100). Distributed Bragg resonators and photonic crystal cavities, on the other hand, while they achieve localized energy distribution and small effective mode volumes, these structures require tens to hundreds of Bragg layers or lattice periods to effectively confine the mode, thus resulting in physical footprints that are still many wavelengths in size.

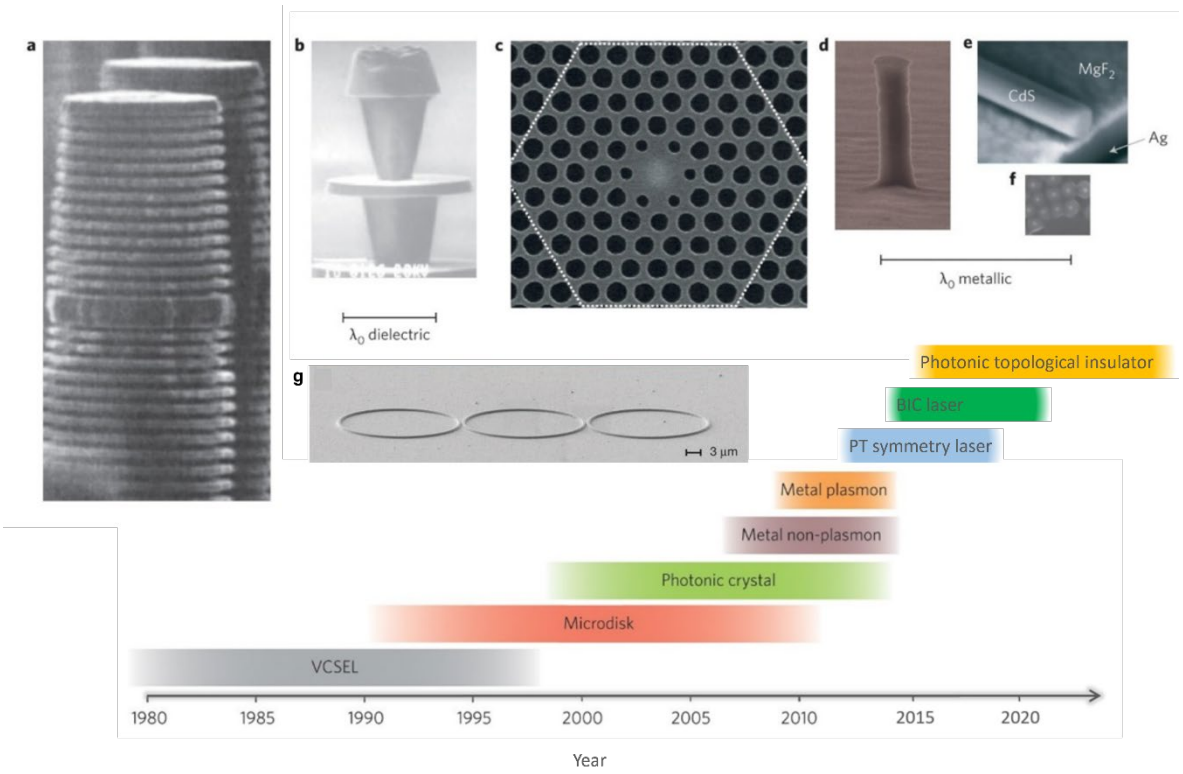

Fig. 3.2: **Small-scale laser evolution, from the first demonstration.** Electron microscopy pictures of different lasers are scaled to their respective free-space emission wavelength ($\boldsymbol{\lambda_0}$): (a) Vertical-Cavity Surface-Emitting Laser (VCSEL), (b) Microdisk Laser, (c) Photonic Crystal Laser, (d) Metallic Non-Plasmon Mode Laser, (e) Metallic Propagating Plasmon Mode Laser, (f) Localized Plasmon Mode Laser, and (g) PT-symmetric microring laser. A size comparison of various types of small lasers is also shown. Reproduced from **(101, 102)** with permission from Springer Nature, © 2014 Springer Nature, © 2017 Springer Nature.

Metal-clad nanolasers, introduced in the late 2000s, have revolutionized this field by enabling both subwavelength physical footprints and mode volumes. Fig. 3.3 highlights the significance of metal-based lasers in terms of their operating speed and device dimensions. In a metal-dielectric interface, the excited modes are known as surface plasmon polaritons (SPPs), which consist of a photon coupled with a collective oscillation of electrons (32). SPPs have an effective wavelength that is shorter than the wavelength in free space allowing for the confinement of electric fields at subwavelength scales, although it comes with the drawback of increased loss (103). Moreover, the metal cladding effectively guides optical modes, allowing for precise design of the cavity to channel most of the spontaneous emission into the lasing mode (34). This mitigates unwanted emission into non-lasing modes, and the efficiency below the lasing threshold is limited only by non-radiative recombination (34).

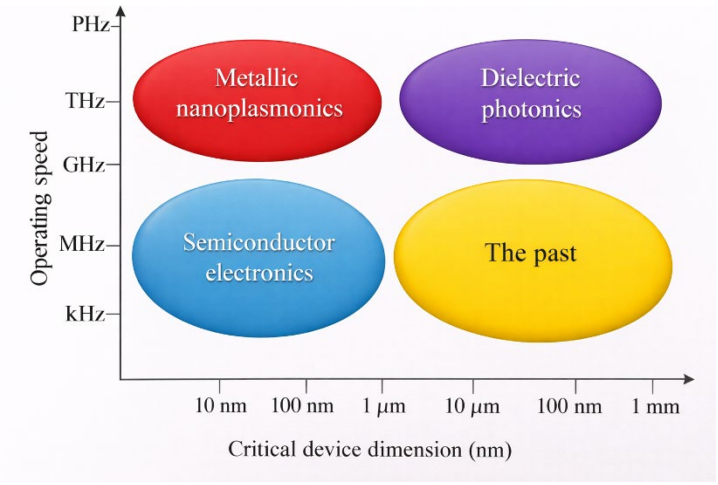

Fig. 3.3: **Advantages of metallic nanoplasmonics.** Different domains in terms of operating speed and device sizes are determined by the unique material properties of semiconductors (electronics), insulators (photonics), and metals (plasmonics). The dashed lines in the figure represent the physical limitations of different technologies. Semiconductor electronics faces limitations in speed due to heat generation and interconnect delay time issues, typically reaching around 10 GHz. On the other hand, dielectric photonics is limited in size by the fundamental laws of diffraction. Plasmonics, however, offers a promising solution as it can act as a bridge between photonics and nanoelectronics. It combines the advantages of both fields, providing enhanced operating speeds and enabling smaller device dimensions beyond the limitations of traditional semiconductor electronics and dielectric photonics. Adapted from **(104)**.

Recently, PT-symmetric microring lasers based on the concept of PT symmetry accessed by judiciously incorporating optical gain and loss in a coupled microring cavity system have been developed (102, 105, 106). When the gain and loss that are defined by optical pumping are closely controlled to be identical, i.e. at the so-called exceptional point, a transition among lasing modes occurs providing better performance and robustness (105). More recently, it has been discovered that the optical modes of topological insulators are immune to the obstacles or perturbations caused by defects or disorders in cavities. These unique properties of topological insulators, when harnessed within the boundaries of a cavity, can be used to create what is known as a "photonic topological insulator laser" (107). Additionally, the concept of Bound States in the Continuum (BIC) has been introduced as a means of confining light within an open system, achieved through the elimination of radiation states due to destructive interference between resonant modes. BIC modes exhibit extremely high quality (Q) factors, which become infinitely large at a specific wavevector within the continuous spectrum range (108). All these strategies for light confinement hold significant promise for enabling strong interactions between light and matter and for the development of ultra-compact, low-threshold lasers.

Among various micro and nanolaser architectures, we will focus, in the upcoming sections, on metallic coaxial nanolasers and their lasing properties. These lasers have the remarkable capability to eliminate threshold constraints, achieving a "thresholdless" lasing (34). The concept of thresholdless

operation, a topic that continues to be a subject of debate and investigation, is extensively evaluated through classical characterization techniques and photon statistics analysis. However, it is important to note that nanolasers do have a threshold and should not be confused with a hypothetical zero threshold. Additionally, to evaluate the threshold of these lasers, one should perform photon statistics analysis. This chapter focuses on evaluating the lasing behavior of metallic coaxial nanolasers at various input powers and finding the actual threshold that cannot be determined through classical characterization techniques.

3.2 Theory and Method

In this section, we describe the architecture of the metallic coaxial nanolaser, along with the characterization techniques employed to study its emission properties. These techniques include an investigation of photoluminescence, analysis of $L-L$ curves, and the implementation of second-order correlation measurements, all aimed at investigating and understanding the thresholdless behavior exhibited by metallic coaxial nanolasers.

3.2.1 Metallic coaxial nanolasers

Quantum well – The dielectric cavity

A quantum well is formed when a semiconductor with thickness (L_z) comparable to the de Broglie wavelength ($\lambda = \frac{h}{p} \sim L_z$, where h and p are Plank's constant and momentum, respectively) is sandwiched between barriers made of semiconductor materials with higher bandgap (109, 110). The quantum well structure consists of a series of energy levels and associated sub-bands formed due to the quantization of electrons in the direction of the quantum well thickness (Fig. 3.4). This is an example of the famous particle-in-the-box problem in quantum mechanics (109).

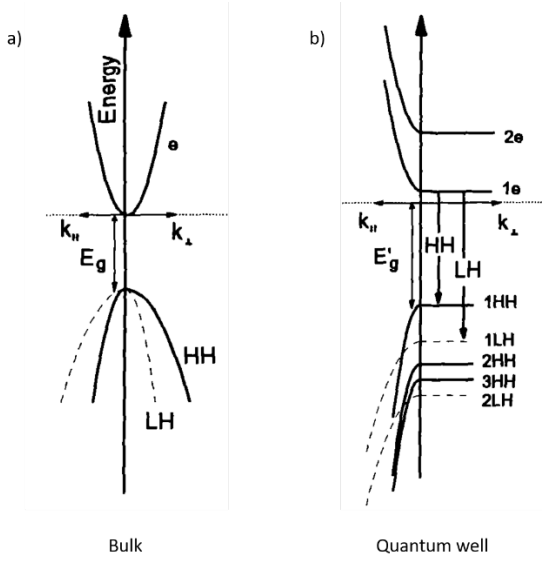

Fig. 3.4: **Schematic diagram illustrating the energy band shapes of bulk and quantum well structures.** Reproduced from **(109)** with permission from Springer Nature, © 1993 Springer Nature.

.

The energy of electrons in a quantum well, confined in the $x-y$ plane is given by:

$$E(n, k_x, k_y) = E_n + \frac{\hbar^2}{2m}\left({k_x}^2 + {k_y}^2\right) \tag{3.2.1}$$

Here, E_n is the energy eigenvalue of the n^{th} confined particle, m is the effective mass of the electron, $\hbar = \frac{h}{2\pi}$, and $k_{x(y)}$ are the $x(y)$ components of the crystal "momentum" (110). The density of states of the confined electrons is given by,

$$\rho_c(E) = \sum_{n=1}^{\infty} \frac{m}{\pi\hbar^2} H[E - \epsilon_n] \tag{3.2.2}$$

where $H[x]$ is a Heaviside function, which describes discontinuities in the density of states, taking values of 0 for negative arguments and unity for positive arguments. Here ϵ_n is energy for the quantized energy level of electrons in the n^{th} sub-band of the quantum well (111). When the barriers are sufficiently high and the barrier thickness is sufficiently large,

$$\epsilon_n = \frac{(n\pi\hbar)^2}{2m{L_z}^2} \tag{3.2.3}$$

where L_z is the thickness of the quantum well (111).

Interestingly, the density of states can be modified through a multi-quantum well structure. When the barrier layers between quantum wells are thick enough, each quantum well operates independently. This modification results in the density of states being expressed as follows, where N represents the number of quantum wells (111)

$$\rho_c(E) = N \sum_{n=1}^{\infty} \frac{m}{\pi\hbar^2} H[E - \epsilon_n]. \tag{3.2.4}$$

On the other hand, if the barrier is sufficiently thin or its barrier height is small enough such that coupling between adjacent wells is substantial, the quantized energy levels are no longer degenerate, and each single well level splits into N different energy levels. In this case, the density of states is expressed by,

$$\rho_c(E) = \sum_{n=1}^{\infty} \sum_{k=1}^{N} \frac{m}{\pi\hbar^2} H[E - \epsilon_{nk}] \tag{3.2.5}$$

where ϵ_{nk} $(k = 1, \dots, N)$ are the energy levels which split from a single well energy level (111).

Thus, by leveraging the capability to grow semiconductor layers with atomic scale precision in thickness, it becomes possible to engineer the material bandgap, confining electrons within the structure. This quantum confinement along the growth direction significantly modifies the semiconductor's band structure and can potentially alter every property of the material (112). In the case of quantum well lasers, confinement alters the wave functions of electrons and holes, leading to modifications in the optical gain of the material, thus improving the lasing characteristics (112). The widespread interest in the application of these lasers stems from their fascinating physical properties and outstanding characteristics, including low threshold current density, tunability of lasing wavelength, and excellent dynamic performance (111). However, the development of small-scale lasers faces two primary challenges: improving mode

confinement and surpassing the fundamental diffraction limit (32). One effective solution to address these challenges is to incorporate metals into dielectric cavities.

Metallo-dielectric cavity

Metals can effectively suppress leaky optical modes and isolate them from the surrounding environment. The modes in metallo-dielectric cavities can be classified into two types: (i) resonant optical modes resulting from the light guiding operation within the metal cavity owing to total internal reflection and (ii) surface-bound resonant modes known as surface plasmon polaritons (32).

In classical electromagnetic theory, a surface plasmon polariton refers to an electromagnetic mode that exists at the interface between a metal and a dielectric, typically characterized by the electrical permittivity functions of the materials. In the context of condensed matter physics, a surface plasmon polariton can be understood as a collective oscillation of the "electron sea" against a stationary background of positively charged ions (113). This oscillation can be excited by an incident radiation that matches the frequency and momentum of the collective motion (113). The unique characteristic of surface plasmon polaritons helps to achieve higher spatial confinement compared to modes found in purely dielectric materials (114).

In addition, in metal-dielectric interfaces, the optical density of states experiences a significant enhancement compared to systems composed solely of dielectric materials. This enhancement is directly linked to the capability of plasmonic modes to surpass the limitations imposed by diffraction (32, 113, 114). Furthermore, metals possess negative permittivity; therefore, can act as efficient mirrors, leading to the second class of metallo-dielectric cavity modes. These modes exhibit higher quality factors (Q factors) and lower lasing gain thresholds compared to plasmonic modes.

However, metal shield introduces Joule losses (energy loss in the form of heat) and the high refractive index of the dielectric core exacerbates the problem, resulting in increased plasmonic and Fresnel reflection losses (115). Hence, achieving a purely plasmonic dielectric laser at telecommunication wavelengths becomes challenging due to the substantial increase in the gain threshold. Nevertheless, these issues can be rectified to an extend by lowering the operating temperature. This helps to overcome metal losses by reducing Joule losses and increasing the achievable semiconductor gain (115).

The ultra-small mode volumes offered by these resonators have significant implications in nanolaser design, facilitating lasing effects. By carefully designing the cavity to enhance the spontaneous emission rate through the Purcell effect and ensuring a single mode within the gain bandwidth, it becomes possible to achieve a nearly perfect spontaneous emission coupling ratio (i.e., close to unity) thus realizing 'thresholdless' lasing (34).

Purcell effect and Spontaneous emission factor

Spontaneous emission, which arises from the interaction between atoms and the vacuum field, is irreversible due to the infinite number of vacuum states available to the emitted photon. Also, modifying the geometry of the cavity can enhance spontaneous emission from atoms by altering the mode structure of the vacuum field (116, 117). For example, by carefully designing the cavity of a subwavelength laser, it is possible to direct a significant portion of the spontaneous emission into the lasing mode (34, 92, 118). This effect is called the Purcell effect, and it describes the enhancement or inhibition of the spontaneous emission rate of a radiating dipole (emitter) by manipulating the dipole-field interaction and density of available photon modes using a cavity (116, 119).

Let us consider a scenario where a single radiating dipole is localized within a medium of refractive index, n (86). This dipole is weakly coupled to the field and is placed inside a monomode cavity. When the emission line of the dipole is significantly narrower than the cavity resonance, we can treat the cavity as a continuum of modes. This allows to compute its spontaneous emission using the Fermi Golden rule (86). The average spontaneous emission rate for an electric dipole transition, considering the various modes experienced by the emitter, can be expressed as:

$$\frac{1}{\tau} = \frac{2\pi}{\hbar^2}\rho(\omega_e).\langle|\langle\bar{d}.\bar{\varepsilon}(\bar{r_e})\rangle|^2\rangle. \tag{3.2.6}$$

Here, $\rho(\omega_e)$ represents the density of photon modes at the angular frequency of the emitter, ω_e. The terms $\bar{d}$, $\bar{\varepsilon}$ and $\bar{r_e}$ are the transition dipolar matrix element, electric field operator and emitter location, respectively (86). The electric field operator for the cavity mode can be defined as:

$$\bar{E}(\bar{r},t) = i\varepsilon_{max}\bar{f}(\bar{r})\hat{a}^{\dagger}(t) + h.c. \tag{3.2.7}$$

In this expression, ε_{max} is the maximum field per photon, $\hat{a}^{\dagger}$ is the photon creation operator, $h.c.$ represents the Hermitian conjugate and $\bar{f}$ characterizes the spatial function of the mode that describes the local field polarization and relative field amplitude (86). ε_{max} can be estimated by equating that the vacuum-field energy for effective cavity volume V_{eff}, to $\frac{\hbar\omega}{2}$ for each mode of frequency, ω, as:

$$\varepsilon_{max} = \left(\frac{\hbar\omega}{2\varepsilon_0 n^2 V_{eff}}\right)^{\frac{1}{2}}. \tag{3.2.8}$$

Introducing the radiating dipole into the cavity modifies its spontaneous emission rate in three distinct ways: the spectral density of modes, amplitude of the vacuum field, and the orientation of the field relative to dipole (86). Here, the mode density of the mono-mode cavity, ρ_{cav}, observed by the emitter $\left(\frac{1}{\omega_c}\right)$ follows a normalized Lorentzian and is given by

$$\rho_{cav}(\omega) = \frac{2}{\pi\Delta\omega_c} \cdot \frac{{\Delta\omega_c}^2}{4(\omega-{\omega_c}^2)+{\Delta\omega_c}^2} \tag{3.2.9}$$

And

$$\rho_{cav}(\omega_c) = \frac{2}{\pi\Delta\omega_c} = \frac{2Q}{\pi\omega_c} \tag{3.2.10}$$

Where Q is the quality factor, $\frac{\omega_c}{\Delta\omega_c}$ and $\Delta\omega_c$ is the linewidth of the cavity mode (32, 86). Additionally, the mode density in free-space is given by

$$\rho_{free}(\omega) = \frac{\omega^2 {V_{eff}}^3}{\pi^2 c^3}. \tag{3.2.11}$$

Thus, the enhancement of the spontaneous emission rate compared to free space is determined as

$$\frac{\tau_{free}}{\tau_{cav}} = \frac{3Q\left(\lambda/n\right)^3}{4\pi^2 V_{eff}} \cdot \frac{{\Delta\omega_c}^2}{4(\omega-{\omega_c}^2)+{\Delta\omega_c}^2} \cdot \frac{|\bar{\varepsilon}(\bar{r_e})|^2}{|\bar{\varepsilon}_{max}|^2} \eta^2 \tag{3.2.12}$$

for $\eta = \bar{d}.\bar{\varepsilon}(\bar{r_e})/|\bar{d}|.|\bar{\varepsilon}(\bar{r_e})|$. The first term of this equation relates to cavity properties and is considered the figure-of-merit for maximizing the Purcell effect, which represents the spontaneous emission enhancement (31, 40). The other terms depend on the spectral detuning, and are always smaller than one (86). The figure-of-merit, thus, takes the form

$$F_p = \frac{\tau_{free}}{\tau_{cav}} = \frac{3Q\left(\lambda/n\right)^3}{4\pi^2 V_{eff}}. \tag{3.2.13}$$

In nanolasers, the interplay between enhanced emission and a reduced number of cavity modes compared to larger lasers has significant implications, particularly for subthreshold behavior. These effects are generally favorable as they promote the efficient utilization of spontaneous emission in the lasing mode, thereby, lowering the laser threshold. The degree of utilization of spontaneous emission into the lasing mode is quantified by the spontaneous emission factor, β (84, 85). It represents the ratio of spontaneous emission channeled into the lasing mode ($F_{p,lasing}$) to the total spontaneous emission across all modes ($\sum_m F_{p,m}$).

$$\beta = \frac{F_{p,lasing}}{\sum_m F_{p,m}} \tag{3.2.14}$$

The value of β is, therefore, a measure of the efficiency of the carrier photon dynamics below threshold and is often considered a performance indicator for nanolasers. Experimentally, spontaneous emission factor can be determined by analyzing the spectral measurements of the laser output at cryogenic temperatures ($\sim 4.5\,K$) (32). At such low temperatures, non-radiative recombination processes are

suppressed, allowing the spontaneous emission factor to be extracted as the fitting parameter in the rate equation analysis.

3.2.1.1 Designing metallic coaxial nanolasers

The miniaturization of laser resonators in three dimensions, using dielectric or metallic material structures, presents two challenges. Firstly, it requires ensuring the scalability of the (eigen-) modes, ensuring the existence of a self-sustained electromagnetic field regardless of the cavity size. Secondly, there is a need to address the relationship between optical gain and cavity loss, which often leads to a large and potentially unattainable lasing threshold as the resonator volume is reduced (120). Therefore, the design of nanolasers that overcome these challenges focuses on two objectives.

The first objective is to design subwavelength-sized nanocavities with modes significantly smaller than the operating wavelength (121). This is achieved by utilizing coaxial resonators that support the cut-off-free TEM mode (122). Coaxial cavities, commonly found in microwave frequencies, consist of a central cylindrical metal piece surrounded by a symmetric dielectric piece, which is further surrounded by a hollowed-out cylindrical metal structure (34, 123). The resonator length or height is chosen to be $\frac{l\lambda}{2n_{eff}}$, where l is an integer greater than zero. At microwave frequencies, the metal behaves as a perfect conductor, and n_{eff} is equal to the refractive index of the dielectric. On the other hand, at optical wavelengths, the metal deviates from perfect conductivity, and surface plasmon polaritons form along the metallic and dielectric interfaces. This plasmonic property enables confinement of optical wave into dimensions much lower than the diffraction limit, allowing for simultaneous size reduction in all three dimensions of the coaxial cavity. The second objective is to reduce the high lasing threshold inherent to small resonators by utilizing cavity quantum electrodynamics (QED) effects to maximize the coupling of spontaneous emission into the lasing mode (121).

A metallic coaxial nanolaser is an example of such a design (34) and is illustrated in Fig. 3.5. It consists of a metallic rod (silver) at the center of the cavity, surrounded by a ring of semiconductor gain (quantum wells), which is then encapsulated by silver. The top and bottom sides are terminated by a SiO_2 plug and air, respectively, to enhance mode confinement. The SiO_2 layer prevents the formation of unwanted plasmonic modes at the interface, while the lower air plug enables optical pumping and out-coupling of light. The silver acts as an effective heat sink, aiding the lasing process under optical pumping. This coaxial cavity exhibits several promising properties of an “ideal” nanolaser, including the capability to support ultra-small confined modes despite being subwavelength. This results in a large Purcell factor and a significant portion of spontaneous emission being coupled into the laser mode. The small cavity size,

high Purcell factor, F_p, and lower Q-factor associated with these cavities are expected to provide a large direct modulation bandwidth, eliminating the need for standalone on-chip modulators (34). Additionally, the reduced radiative lifetime due to the Purcell factor decreases the total carriers available for recombination through non-radiative channels, reducing the sensitivity to Auger and surface recombination processes intrinsic to semiconductor lasers (34).

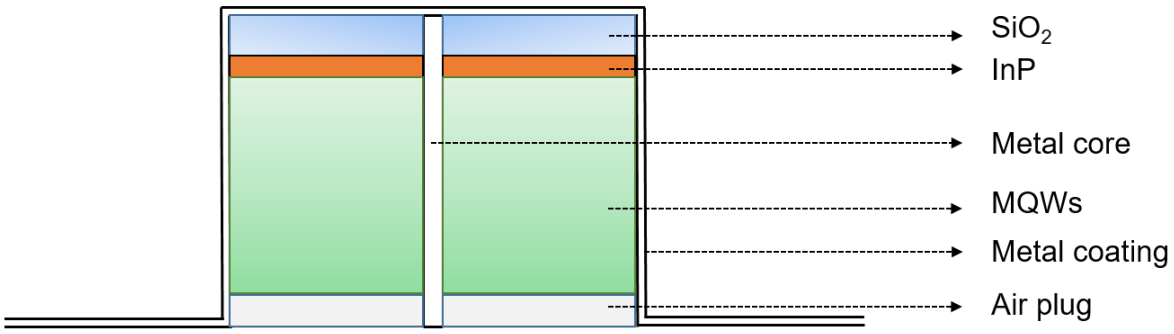

Fig. 3.5: **Schematic of metallic coaxial nanolaser.** It comprises multi-quantum-wells (MQWs) that encircle a plasmonic metal core. The plasmonic metal core provides enhanced light-matter interaction and facilitates confinement of the optical modes. The top and bottom sides are terminated by a SiO_2 plug and air, respectively, to enhance mode confinement. The metal cladding helps to confine the light within the pillar and provides effective heat dissipation, enabling the nanolaser to operate under optical pumping conditions.

Rate equations for high- $\boldsymbol{\beta}$ *coaxial nanolasers*

The rate equations are a commonly used approach for analyzing the steady state and dynamic behavior of lasers. While studying nanolasers, additional considerations must be considered, specifically, the Purcell effect needs to be incorporated into the rate equations. Proper normalization of the optical field and the dispersive nature of materials, particularly metals commonly used in nanolaser design, must also be considered.

Taking into account these factors and the carrier density dependence of various parameters, the rate equations can be expressed as follows (32, 123):

$$\frac{dn}{dt} = \eta_i \frac{I}{qV_a} - R_{nr}(n) - R_{sp}(n) - R_{st}(n)S \tag{3.2.15}$$

$$\frac{dS}{dt} = -\frac{S}{\tau_p} + \beta R_{sp}(n) + \beta R_{st}(n)S \tag{3.2.16}$$

Here, n represents the carrier density, I denotes the injection current, η_i represents the current injection efficiency, q is the unit charge of an electron, V_a stands for the active volume, S represents the photon density, and β is the spontaneous emission coupling factor. The non-radiative recombination rate, $R_{nr}(n)$,

is given by $\frac{n}{\tau_{nr}}$. The total spontaneous emission rate, $R_{sp}(n)$, is given by $\frac{nF_p}{\tau_{sp}}$. The stimulated emission coefficient, $R_{st}(n)$, is given by $\frac{n\beta\Gamma F_p}{n_{sp}\tau_{sp}}$, where Γ is the mode confinement factor that accounts for plasma dispersion and the negative permittivity of metals, ensuring positive optical energy (124). Also, the spontaneous and non-radiative lifetimes are denoted as τ_{sp} and τ_{nr}, respectively. n_{sp} is determined by

$$n_{sp} = \frac{(f_c(1-f_v))}{f_c - f_v}, \tag{3.2.17}$$

where f_c and f_v are Fermi-Dirac functions in the conduction and valence bands (85, 125). At steady state, the photon density, S, and the threshold current, I_{th}, can be expressed as:

$$S = \frac{\Gamma\beta R_{sp}(n)}{\frac{1}{\tau_p} - \Gamma R_{st}(n)} \tag{3.2.18}$$

And

$$I_{th} = \frac{n_{sp}}{\omega_k} \cdot \frac{q}{\Gamma\beta Q}\left(1 + \frac{\tau_{sp}}{F_p\tau_{nr}}\right) \tag{3.2.19}$$

Where τ_p, the photon lifetime, is given by

$$\frac{1}{\tau_p} = \frac{\omega_k}{Q} = \frac{\omega_k}{Q_{rad}} + \frac{\omega_k}{Q_{abs}} \tag{3.2.20}$$

here, ω_k is the resonant angular frequency of the k^{th} mode and Q_{rad} is the Q factor due to radiation and Q_{abs} is the Q factor due to absorption and scattering loss.

It can be observed that the threshold is inversely proportional to the product of β, Γ, and Q. Additionally, the Purcell factor contributes to threshold reduction by increasing the decay rate of spontaneous emission relative to non-radiative processes. In most semiconductor gain systems where $\frac{\tau_{sp}}{\tau_{nr}} \gg 1$, a significant Purcell factor is expected to play a crucial role in determining the threshold value.

3.2.1.2 Micro-photoluminescence characterization

When stimulated emission dominates the output power, a light-emitting device is classified as a laser. Generally, the Light-Injection ($L-I$) or Light-Light ($L-L$) curve, which are plotted between the light input/ current injection versus output light, are utilized to study the emission properties of a laser (32). The $L-L$ curve exhibits three distinct regions (Fig. 3.6), showing a visible "kink" for the curve with a small β value. At low pump intensities, the device operates in the photoluminescence (PL) regime, functioning as a thermal source similar to a LED, with a unitary slope in the $L-I$ or $L-L$ curve (32, 34, 126). As the pump intensity increases, there is a sudden power surge allocated to the 'future' lasing mode,

resulting in a nonlinear kink known as the amplified spontaneous emission regime (ASE), where the slope of the log-log curve exceeds one (32, 34, 126). Further increasing of the pump energy causes the slope to return to unity, indicating operation in the lasing mode (32, 34, 126).

Fig. 3.7 illustrates the influence of β on both the linear light-light curve and the log-log plot of the $L-L$ curve, along with the threshold condition. The kink in the curve is commonly referred to as the lasing threshold (32). However, as β increases, the kink gradually transforms into a smoother feature and eventually disappears completely in the extreme case of $\beta = 1$. While conventional semiconductor lasers typically have β values around 1×10^{-5}, the range of values used in Fig. 3.7 is typical for nanolasers (32). To better observe the subthreshold behavior, nanolaser $L-L$ curves are usually plotted in logarithmic scale, as shown in Fig. 3.7 (b). Since the kink region is associated with the lasing threshold, it is argued that the threshold decreases as β increases (assuming all other factors remain constant), ultimately leading to a thresholdless behavior when β reaches unity (32).

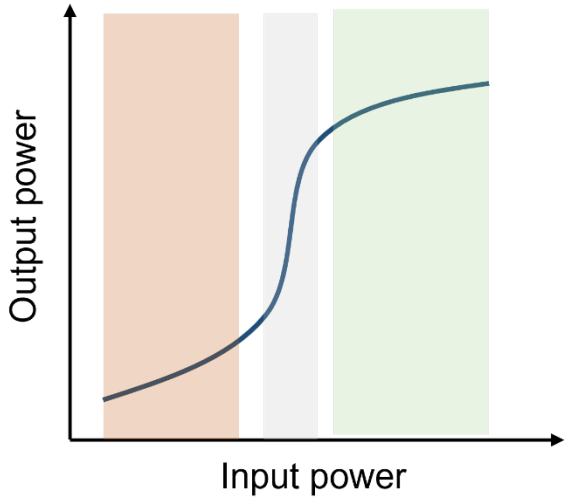

Fig. 3.6: **Illustration of $L-L$ curve for a laser in logarithmic scale.** The input power is represented on the x-axis, while the output power is represented on the y-axis. In the low pump intensity regime (indicated by the orange shading), the device operates in the PL region. As the pump power is gradually increased, there is a sudden rise in the output power, implying the onset of amplified spontaneous emission (ASE; indicated by the grey shading). With further power increase, the device enters the lasing regime, characterized by sustained and coherent emission, which is depicted by the green shading.

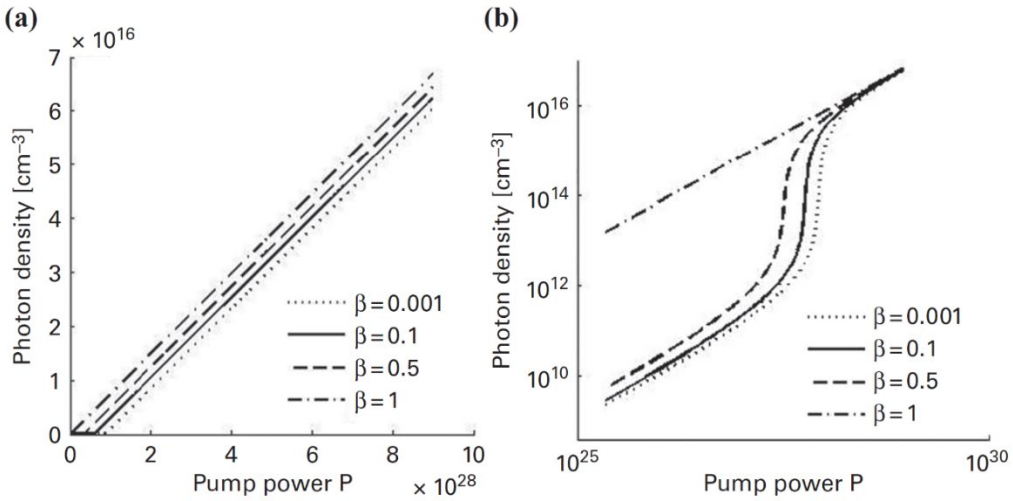

Fig. 3.7: ***L − L* curve for various *β* values.** The light-in vs. light-out curve is simulated for various values of the spontaneous emission factor ***β***, and it is presented in two different scales: (a) linear scale and (b) logarithmic scale. Reproduced from **(32)** with permission from Cambridge University Press, © 2014 Cambridge University Press.

3.2.2 Correlation measurements

Though the $L-L$ or $L-I$ curve is the most common characterization technique to study the emission properties of a semiconductor laser, improved insights into the threshold and emission properties at the micro/nano scale lasers can be obtained by studying the photon statistics. Hanbury Brown and Twiss experimental setup (6) leads to the determination of second-order correlation function and can be used for the classification of light properties as coherent, bunched, or antibunched (5).

Hanbury Brown and Twiss experiments with photons

In the HBT setup, a stream of photons enters a 50-50 beam splitter, dividing the photons equally between two output ports so as to reach the detectors, D_1 and D_2 as shown in Fig. 3.8. By measuring the time interval between pulses from the two detectors and counting the number of pulses at each input, we can analyze the second-order correlation function in terms of photon counts. The degree of second-order coherence, $g^2(\tau)$, in this experimental setting can be expressed as:

$$g^2(\tau) = \frac{\langle n_1(t) n_2(t+\tau)\rangle}{\langle n_1(t)\rangle \langle n_2(t+\tau)\rangle} \tag{3.2.21}$$

Here, $n_i(t)$ represents the number of counts registered on the detector i at time t. This formulation allows the HBT measurements to provide a direct measurement of the second-order correlation function (5).

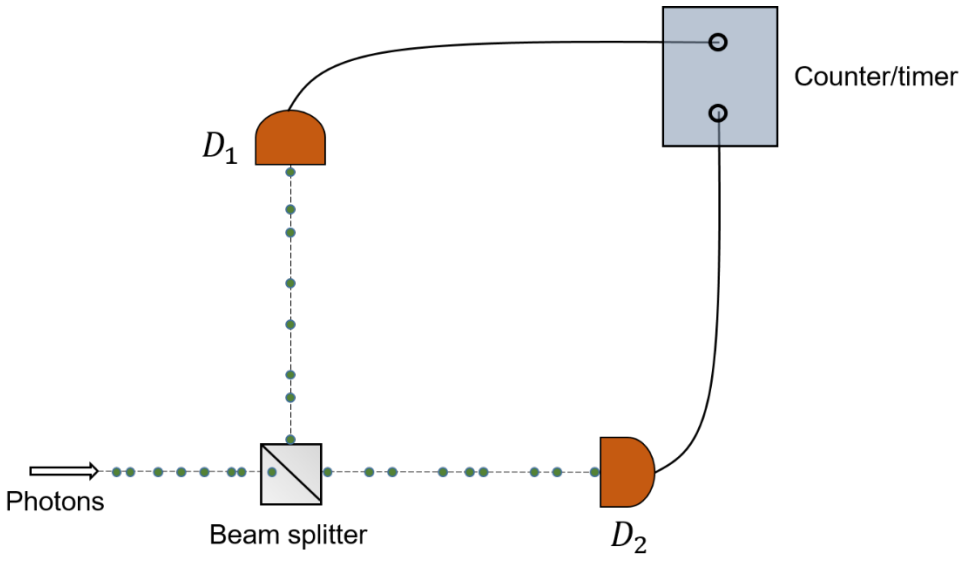

Fig. 3.8: **Hanbury Brown and Twiss experiment with photons.** A stream of photons incident a 50-50 beam splitter, where is equally divided between the two output ports. The photons then impinge on the detectors $\boldsymbol{D_1}$ and $\boldsymbol{D_2}$ and the resulting output pulses are timed utilizing an electronic counter/timer.

3.3 Results and Discussion

This section presents the experimental setup and main results concerning the emission properties, in particular, the thresholdless behavior of nanolaser via $L-L$ curve and second-order correlation function. In addition, we will utilize the second-order correlation function to investigate the temporal dynamics of the photon statistics associated to the nanolaser emission.

3.3.1 Experimental setup for emission characterization

Micro-PL optical characterization is a commonly employed method to study the laser performance. It offers valuable insights into the spectroscopic properties of active devices across different excitation levels and provides data on light emission as a function of input power ($L-L$ curve). While this method is straightforward for conventional electrically/optically pumped semiconductor lasers with high output power, it poses challenges for nanolasers due to their low output power, making both excitation and detection more difficult in micro-PL measurements.

In Micro-PL excitation, several factors need consideration. Firstly, the specific design of the metal-cladding and bottom aperture demands that the measurement be conducted in reflection mode. This means using the same optical setup for both optical pumping of the nanolaser and collecting the emitted light. Secondly, achieving effective illumination and imaging of the sample requires high magnification to identify and test specific lasers. Thirdly, despite the low signal strength, spectral measurements with high resolution are necessary. Taking these constraints into account, the design depicted in Fig. 3.9 was adopted for micro-PL characterization.

During the characterization process, the sample was initially illuminated using an Amplified Spontaneous Emission source (ASE source) in the infrared (IR) region. To ensure uniform illumination and reduce spatial coherence, the ASE output was passed through a diffuser. Subsequently, the ASE output, after crossing the rotating diffuser, was directed towards the sample via a kinematic mirror. A cooled InGaAs CCD camera was employed to image the sample, facilitating the identification and positioning of the specific laser device of interest at the center of the field of view.

In the experiment, a pulsed 1064 nm laser was used to pump the nanolaser sample. Pulsed excitation was chosen to minimize heating effects within the laser cavity design. The pulse width and repetition rate were carefully selected to achieve a high enough peak power to reach the lasing threshold while maintaining the average power low enough to prevent thermal damage to the device under test. The pump beam was directed through a dichroic beam splitter and focused onto the sample using a microscope objective (Mitutoyo 50× objective with a numerical aperture of 0.42), resulting in a spot size of 150 μm on the sample.

The same objective was utilized to collect the emitted light from the nanolaser. To selectively collect the emitted light from the nanolaser and eliminate any residual power from the pump laser, a bandpass filter was employed, ensuring that the detected signal originated solely from the nanolaser emission.

Following the removal of the kinematic mirror, the collected nanolaser light was directed towards a monochromator for micro-PL characterization. The monochromator enabled the acquisition of spectral information and the measurement of the total output power emitted by the nanolaser.

Additionally, the experimental setup included a removable mirror that redirected the coupled output towards the Hanbury Brown and Twiss (HBT) setup. The HBT configuration comprised a pair of highly sensitive QuantumOpus SNSPDs, which were read out with the PicoQuant Hydraharp 400 system. To ensure accurate correlation measurements and eliminate pump laser interference, nanolaser emission was again passed through a diffraction grating and slit before reaching the detectors, filtering out the nanolaser output to maintain the coherence time to be 200 ps, exceeding the detector resolution. This also made sure the effective removal of any residual pump leakage. Furthermore, a polarizer integrated into the setup maintained the required polarization component throughout the measurement.

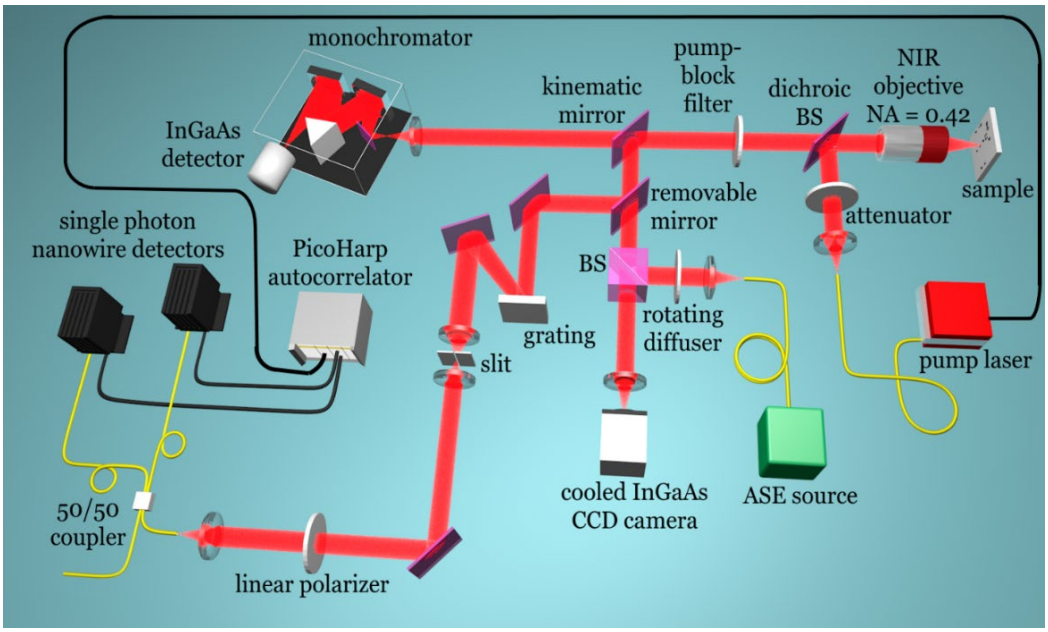

Fig. 3.9: **Experimental setup for photon statistical coherence and spectral measurements**. The sample containing the nanolasers is held at the focus of an objective lens. The emission from the metallic coaxial nanolaser is directed to three separate beam lines (CCD near-infrared camera, spectrometer or single photon detectors). The sample is cooled down to 77 K (cryo chamber and cooling feed not shown). The optical pumping scheme could be varied between CW operation or pulsed mode with various pulse repetition rates, durations and shapes. **(30)**

Metallic coaxial nanolasers

The metallic coaxial nanolaser sample was cooled to cryogenic temperatures (77 K) and maintained at a pressure of 10^{-2} mbar, enhancing its performance, particularly in terms of output power, to ensure a sufficient number of emitted photons for detection.

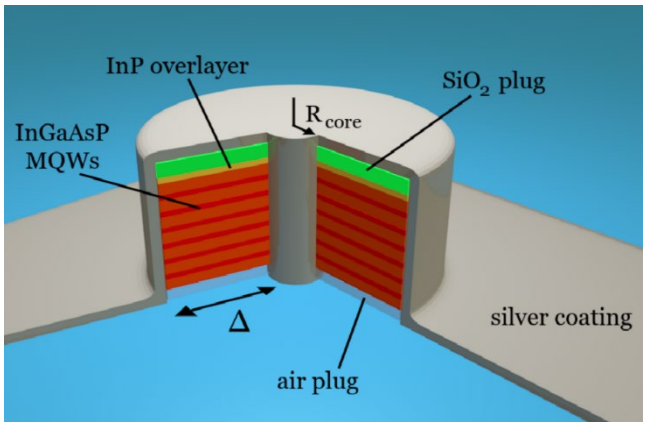

Fig. 3.10: **Schematic of a metallic coaxial nanolaser.** The system is shaped like a pillar consisting of InGaAsP multi-quantum-wells, surrounding a plasmonic metal core. The top and bottom sides are terminated by a SiO_2 plug and air, respectively, to enhance mode confinement. **(30)**

Throughout our experiments, we utilized a metallic coaxial nanolaser with core radius, R_{core} = 65 nm and thickness, Δ = 285 nm (the nanolaser schematic is depicted in Fig. 3.10). The fabrication details of this metallic coaxial nanolaser using nanofabrication techniques are outlined in Reference (34). The nanolaser comprised a metallic rod (R_{core}) surrounded by a silver metal-coated semiconductor ring and gain medium featuring six vertically stacked alternating layers in the form of rings composed of $In_{x=0.56}Ga_{1-x}As_{y=0.938}P_{1-y}$ and $In_{x=0.734}Ga_{1-x}As_{y=0.57}P_{1-y}$ with thicknesses of 10 nm and 20 nm, respectively. The quantum well system, with a total height of $h = 260$ nm, was protected by SiO_2 (30 nm), and InP (10 nm) for the top layer, and an air plug (20 nm) at the bottom. During excitation, the pump pulse was introduced into the gain medium through the air plug and the emission from the nanolaser was extracted using the same air plug. The function of each layer is described in Section 3.2.1.1.

3.3.2 Classical characterization of coaxial nanolasers

In the experiment, a pulsed laser emitting at 1064 nm with 5 ns pulses and 1 MHz repetition rate was used as the pump laser for excitation. Compared to continuous wave (CW), pulsed pumping enables the delivery of a larger number of photons for the same average power, promoting a more efficient build-up of optical gain in the metallic coaxial nanolaser while reducing sample heating due to the inter-pulse cooling time of 1 microsecond (127). The peak fluence at the nanolaser per pump pulse was estimated at 310 W/cm^2, for an average input power of 150 μW at 1 MHz.

Spectral characterization

To fully characterize the spectral output characteristics of the metallic coaxial nanolaser emission, we varied the input average power between 45 μW and 750 μW, accounting for all losses from both the steering optics and the objective. The images of metallic coaxial nanolasers when excited at 250 μW and 630 μW are depicted in Fig. 3.11.

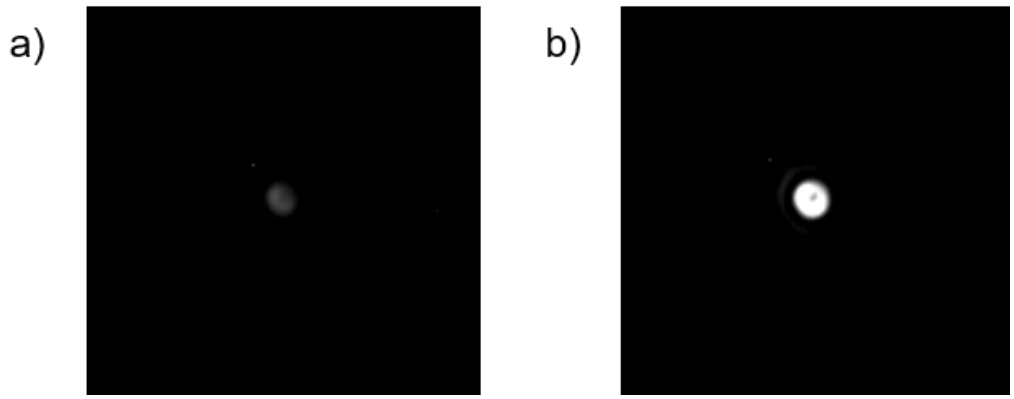

Fig. 3.11: **Images of metallic coaxial nanolasers.** The images are captured by an InGaAs CCD camera when excited by the pump laser of powers 250 μW (a) and 630 μW (b).

The spectral emission of the metallic coaxial nanolaser for various input powers is given in Fig. 3.12. As the pump power increased, the peak emission shifted towards shorter wavelengths, starting from a resonance of 1302 nm at 60 μW and dropping to a resonance of 1296 nm at 600 μW. This blue-shift with increasing input power was attributed to the saturation of energy states in the quantum well induced by the localized carriers. With increasing input powers, along with the saturation of the quantum states, free carriers tend to spill out from these states, which resulted in a blue-shift of the PL emission (128). Wavelength shifts in MQW based structures have been previously reported by Wang et al. (128) and Rosencher et al. (129).

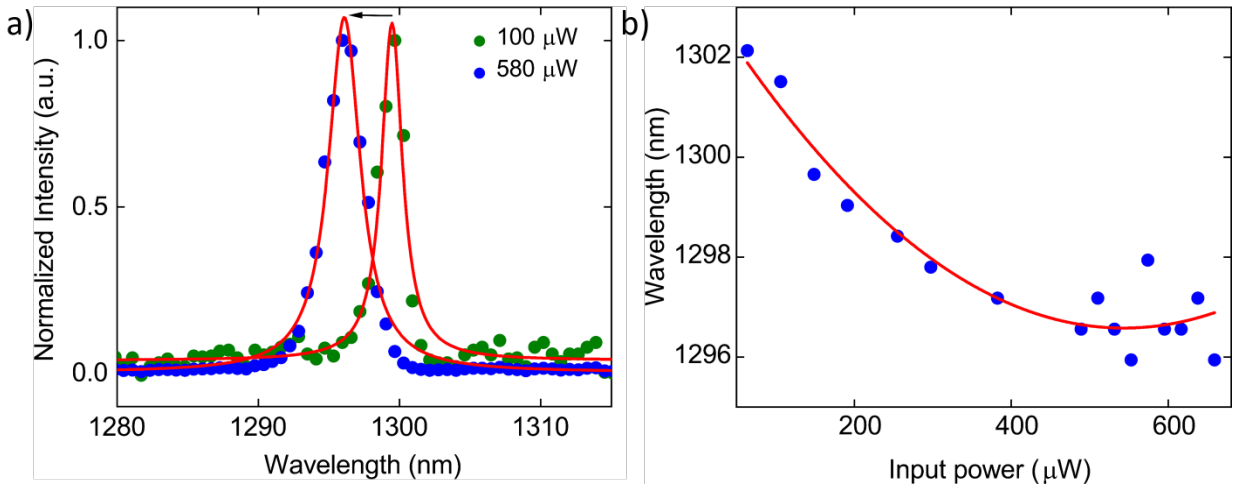

Fig. 3.12: **Blue-shift in metallic coaxial nanolaser as the input power increases.** a) The figure shows the PL spectra at both 100 μW input pump power (green dots, experimental points; red line, Lorentzian fit) and 580 μW input pump power (blue dots, experimental points; red line, Lorentzian fits). b) Decrease of the central wavelength for increasing values of the average input power (blue dots), where a polynomial fit (red line) has been used as an optical guidance.**(30)**

Additionally, the linewidth of the spectrum, determined through Lorentzian fitting, exhibited an increase with input pump powers, as illustrated in Fig. 3.13. Specifically, for the metallic coaxial nanolaser under examination, the measured linewidth, without spectral filtering, ranged from 1.6 nm for lower input powers to 2.6 nm as the pump power increased. At the lowest input power, an isolated data point exhibits a deviation from the general trend, showing a larger linewidth. This discrepancy is likely due to measurement noise, which can arise from fluctuations in the detection system or the limited signal-to-noise ratio at low excitation power.

Several factors contributed to the linewidth broadening in nanolasers. Among them, fluctuations in the refractive index with carrier density played a significant role (33). Spontaneous emission induced phase and intensity changes in the laser field, leading to changes in the imaginary part of the refractive index, thereby causing additional phase fluctuations and line broadening. Furthermore, Padrotti et al. predicted that the expected decrease in linewidth with increasing power would not occur in high-beta lasers (130), emphasizing the dependence of the laser linewidth on the ratio of decay rates from the lower and upper lasing levels. Moreover, they highlighted the fact that the enhancement in spontaneous emission into the lasing mode could elevate the linewidth floor. Consequently, our results reflected the increased number of spontaneous emission events associated with a single pump event as the photon number rose.

Furthermore, the self-heating in metallic coaxial nanolasers could have played a role. Beyond a pump power of approximately 600 μW, the surrounding substrate began to heat up significantly, making it impractical to maintain the nanolaser in the focus of the objective due to excessive thermal drifts. Moreover,

the pump laser operates at 1064 nm, while the resonance wavelength is near 1300 nm, which means that the system is pumped well above the absorption band, leading to substantial energy dissipation as heat. Therefore, we believe that a combination of these factors likely caused the slight increase in linewidth and blueshift with increasing input power in our metallic coaxial nanolasers.

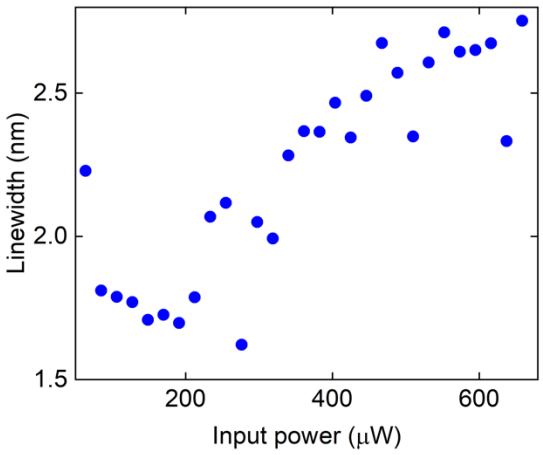

Fig. 3.13: **Linewidth vs input power.** The linewidth value with respect to the input power was determined via a Lorentzian fit. As the input power increases, the linewidth also increases. The measured linewidth, without spectral filtering, was found to be 1.6 nm for lower input powers and increased to 2.6 nm as the pump power was increased. **(30)**

Light-light characterization

The $L-L$ curve, where the output power as a function of average input power is plotted in log-log scale, for the metallic coaxial nanolaser is reported in Fig. 3.14. It is important to note that the output power was normalized and calculated by integrating the spectral power density across the entire PL peak. Typically, the $L-L$ graph of a nanolaser exhibits an S shaped curve, revealing the laser threshold (32, 34, 126), however, in the case of thresholdless lasers, the $L-L$ graph is linear. Our results demonstrated a linear $L-L$ behavior in the fit, with no pronounced kink, which aligns well with the characteristics of high-β nanocavity lasers and supports the hypothesis of thresholdless lasing (131, 132).

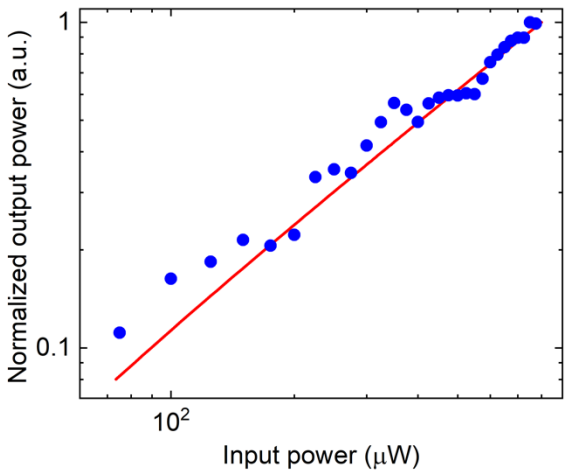

Fig. 3.14: ***L − L* plot for metallic coaxial nanolaser.** Normalized input-output power graph of the metallic coaxial nanolaser in a logarithmic scale (blue dots) and best theoretical fit with $\boldsymbol{\beta}$=0.9 (red line). Notably, there is no threshold-like lasing behavior emerging from these measurements. **(30)**

To determine the β of the nanolaser under investigation, we employed the semi-classical coupled rate equations (34, 126) to fit the data. The coupled rates are given by:

$$\frac{dS}{d\Gamma} = \Gamma g_0(N - N_0)S - \frac{S}{\tau_p} + \frac{\Gamma\beta N}{\tau_{rr}} \tag{3.3.1}$$

$$\frac{dN}{dt} = I_{\mathrm{p}} \exp\left[\frac{(t-t_0)^2}{\Delta^2}\right] - g_0(N - N_0)S - \frac{N}{\tau_{rr}} - \frac{N}{\tau_{rn}}, \tag{3.3.2}$$

where S represented the photon density of the lasing mode and N denoted the carrier density. I_p was the total pump injected carrier density, accounting for factors such as the pump intensity, the thermal effect arising from optical pumping and the effect of drift/diffusion. τ_p represented the photon lifetime, and τ_{rr} and τ_{nr} denoted the radiative and non-radiative recombination lifetimes, respectively. Γ was the energy confinement factor, while the spontaneous emission coupling factor β was defined as the fraction of spontaneous emission coupled into the lasing mode, and written as

$$\beta = \frac{SE_L}{SE_L + SE_{NL} + SE_{FSC}} \tag{3.3.3}$$

where SE_L, SE_{NL} and SE_{FSC} represented the spontaneous emission into the lasing mode, other non-lasing cavity modes, and the free space continuum, respectively. Small-scale lasers, such as nanolasers, exhibit β values ranging from 0.1 to unity. In our study, the estimated β for the metallic coaxial nanolaser under pulsed optical pumping conditions was ~0.9. Also, the coupled rate-equation parameters resulting from the best fit to the measured data for the $L - L$ curve were: $\lambda = 1.30$ μm, $Q = 350$, and $\Gamma = 0.65$. However, $L - L$ curve alone could not determine the thresholdless properties of a nanolaser. Hence, we utilized photon statistics to estimate the true threshold value of our metallic coaxial nanolaser.

3.3.3 Photon statistics of coaxial nanolaser emission

The photon statistics of the metallic coaxial nanolasers are discussed in this section. The nanolaser was excited by the pump pulse with an input average power between 45 μW and 750 μW, accounting for losses from both the steering optics and the objective. The photon statistics were collected using SNSPDs coupled with an electronic time-tagger with a resolution of 128 ps. For all quantum measurements, the coherence time of the nanolaser, 200 ps, was tailored to exceed the detector resolution. This was achieved by passing the nanolaser emission through a diffraction grating and slit before reaching the detectors. A resolution of 128 ps was chosen because it was well below the coherence time of the nanolaser output, allowing the collection of photon arrival times over a longer time window after each trigger event compared to 4 ps resolution. This extended window enabled the generation of a more comprehensive time histogram without affecting the results. Moreover, to prevent both multiphoton events and any nonlinear effects in the $g^2(0)$ measurements, we ensured that the single photon count rate on the detectors was between 3×10^3 and 1×10^4 counts per second corresponding to <0.01 photons/pulse.

Second-order correlation measurements

Following the classical laser characterization, we performed pulsed HBT measurements to determine the second-order correlation function for various pump powers. We averaged the second order correlation function over the full pump pulses as previously done in the literature (133–135).

To determine the threshold and coherence properties of the metallic coaxial nanolaser, we measured the transition from thermal to coherent photon statistics for increasing optical pump powers (Fig. 3.15). The figure reveals that for ~420 μW, the value of $g^2(0)$ approached unity, signifying the threshold and onset of coherent emission. This indicated that the threshold of the coaxial nanolaser occurred at ~420 μW. However, we found a slight deviation of ~0.02 for $g^2(0)$ from unity, which we primarily attributed to amplitude fluctuations in the pump pulse (126).

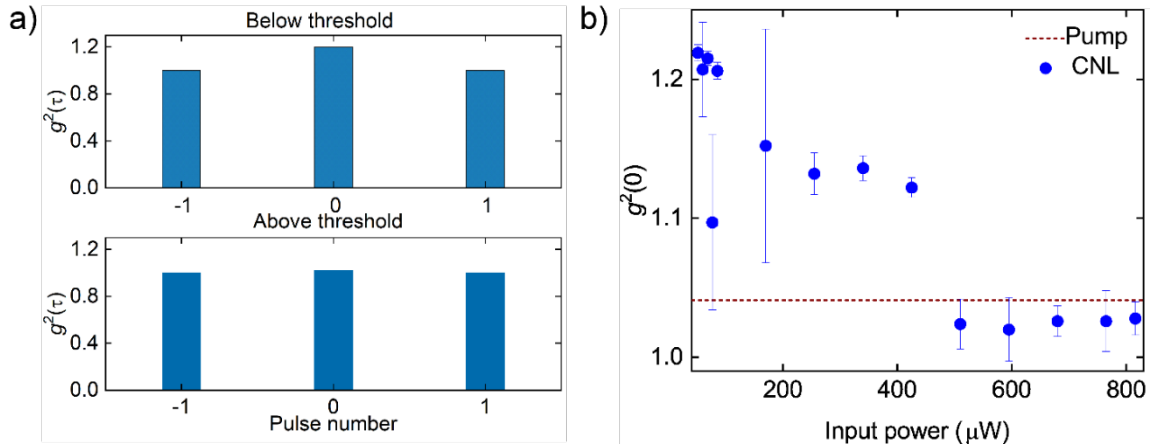

Fig. 3.15: **Second order correlation function.** a) Example of coincidence histograms for $\boldsymbol{g^2(\tau)}$ above and below threshold. b) Second-order correlation function values $\boldsymbol{g^2(0)}$ plotted for varying pump powers. The dotted line is the $\boldsymbol{g^2(0)}$ value of the pump pulse, which is constant over all input powers. The transition of the output radiation from thermal to coherent is clearly seen in the $\boldsymbol{g^2(0)}$ values, which vary from ~ 1.25 to ~ 1 as a function of increasing pump power. **(30)**

Examples of the coincidence histograms for $g^2(\tau)$ as a function of delay τ between different pulses with respect to the trigger are presented in Fig. 3.15 (a) for both the below and above threshold scenarios. In the former case (top panel), an increase of 0.2 in the peak height was observed at zero delay compared to neighboring pulses. This increase, which was absent in the above threshold (lower panel) case was due to photon bunching emerging from the spontaneous emission (SE) regime (126).

The full width half maximum (FWHM) of a correlation peak for the nanolaser emission served as another metric for monitoring the transition from thermal to coherent states. This was attributed to the FWHM being influenced by several factors, including (i) the input pump pulse temporal duration, (ii) the photon lifetime in the upper excited electronic states and (iii) the radiative recombination lifetime. Fig. 3.16 (a) illustrates the measured correlation peak for pump powers of 300 μW and 600 μW, while Fig. 3.16 (b) displays the corresponding determined FWHM for different pump powers.

Initially, as the pump intensity increased in the spontaneous emission (SE) regime, the width of the correlation peak narrowed, reaching a minimum in the amplified spontaneous emission (ASE) regime (126), as shown in Fig. 3.16 (b). Beyond approximately 350 μW, the FWHM initially increases in the lasing regime, reaching a peak around 600 μW, before decreasing at higher pump powers. This behavior is likely influenced by the self-heating effect, which becomes significant beyond 600 μW (126). The error bars remain relatively constant across the pump power range, as they primarily reflect the temporal resolution of the detection system rather than variations in the measured correlation width.

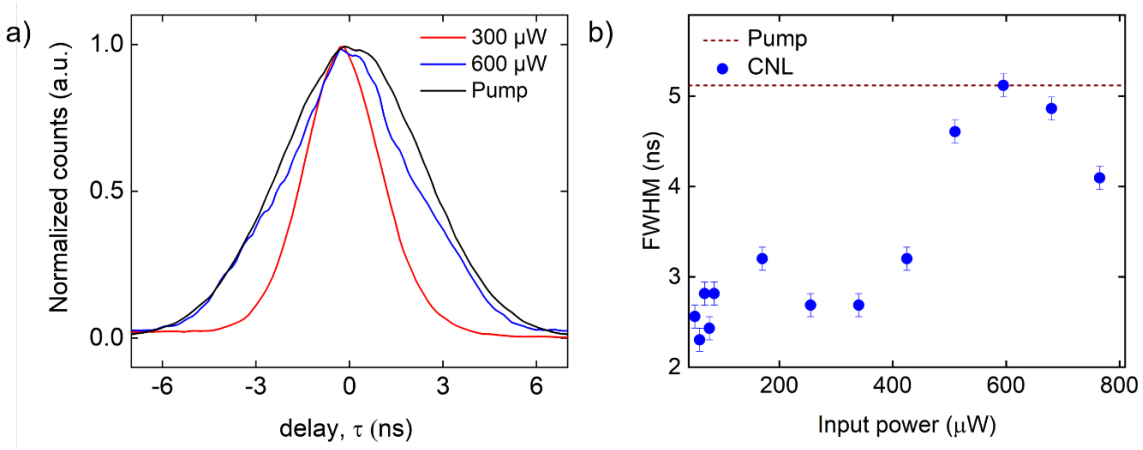

Fig. 3.16: **FWHM of the correlation peak.** a) The measured correlation peak for 300 µW, 600 µW and pump pulse. b) FWHM of the correlation peaks as a function of average power. The brown dotted line represents the FWHM of the pump. We note that around the threshold, i.e. ~350 µW, the FWHM of the correlation peak begins to increase, before falling off again above 600 µW. **(30)**

To describe the broadening of the FWHM as a function of pump power, we employed the semi-classical coupled rate equations, Eq. 3.3.1 and Eq. 3.3.2. By numerically solving the coupled rate equations, we simulated the carrier density and the emission photon density for a single pulse. Our analysis of the measured data revealed variations in both coherence properties and output pulse profiles for different pump intensities, even with the same input pulse temporal profile. Consequently, varying pump carrier densities, denoted as I_p influenced both the autocorrelation peak width and profile.

Considering the impact of thermal effects induced by high pump photon density (126) as well as the attenuation and defocusing introduced by the cryostat, perfect agreement between the experimentally measured FWHM and simulation data was challenging. To address this, we refined the pump intensity parameter I_p in the rate equations for a realistic fit. Specifically, we introduced a modulation factor $m(P)$, to account for different degrees of thermal influence on I_p. Assuming a linear relationship between the input average pump power P and thermal effects, we calculated an effective $I_{p,eff}$, where $m(P_{max})$ ranged from 0.30 to 0.60, and $I_{p,eff}$ was calculated as $m(P) \cdot I_p(P)$. The resulting parameters are presented in Table 3.1.

To illustrate the impact of thermal effects on the width of the autocorrelation peak, we generated two traces from the model: one without modulation (red curve) and another with modulation (blue curve), as shown in Fig. 3.17 (a). The thermal effects in the cavity and the surrounding medium led to a decrease in the number of injected carriers in the cavity, consequently decreasing the FWHM for higher pump powers (126). Indeed, similar outcomes have been reported in reference (136).

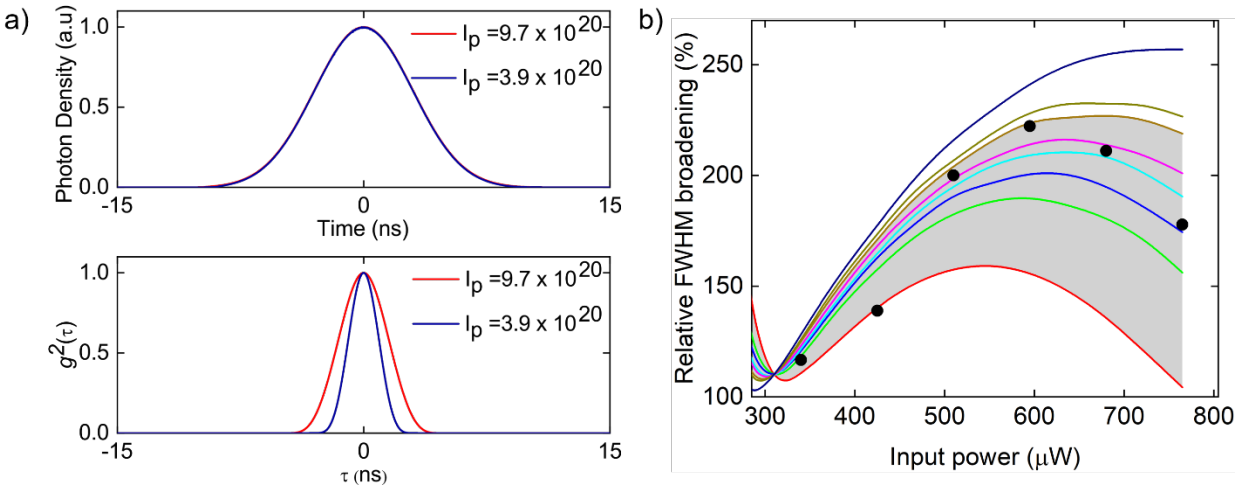

Fig. 3.17: **Photon density and FWHM.** a) Example of simulated carrier density (top panel) and the corresponding autocorrelation traces (bottom panel) for two different injected carrier densities $\boldsymbol{I_p} = 9.7 \times 10^{20}$ (red) and $\boldsymbol{I_p} = \boldsymbol{I_{p,eff}} = 3.9 \times 10^{20}$ (blue) with $\boldsymbol{\beta = 0.9}$. The narrowing of the autocorrelation peak is interpreted here as a result of pump-induced thermal effects. b) The FWHM of the autocorrelation trace as a function of the pump power obtained from the rate equation model with varying modulation factors $\boldsymbol{m}$ at maximum power, $\boldsymbol{m(P_{max})}$ = 0.30, 0.3107, 0.3643, 0.3857, 0.4071, 0.4179, 0.4393, 0.45 (from red to violet). The measured data are presented as black circles, and lie within the range $0.3107 \leq \boldsymbol{m(P_{max})} \leq 0.4071$. **(30)**

Table 3.1: Carrier density I_p values and corresponding $I_{p,eff}$.

$\boldsymbol{P}$ (μW)	$\boldsymbol{I_p}$	$\boldsymbol{I_{p,eff}}$
51	1.26E+19	1.26E+19
85	2.10E+19	2.03E+19
128	3.16E+19	2.94E+19
170	4.20E+19	3.76E+19
213	5.26E+19	4.54E+19
255	6.30E+19	5.21E+19
298	7.36E+19	5.84E+19
340	8.39E+19	6.37E+19
383	9.46E+19	6.85E+19
425	1.05E+20	7.24E+19
468	1.16E+20	7.58E+19
510	1.26E+20	7.82E+19
553	1.37E+20	8.02E+19
595	1.47E+20	8.12E+19
638	1.58E+20	8.16E+19
680	1.68E+20	8.12E+19
723	1.79E+20	8.02E+19
765	1.89E+20	7.84E+19

Time-resolved second-order correlation measurements

In principle, a nanolaser emission comprises time-independent, statistical mixture of coherent and incoherent modes (126). To understand this better, we studied the temporal dynamics of nanolaser emission within a pulse, with respect to the temporal profile of the pump pulse. The temporal profile of the pump pulse obtained from single-photon detector measurements is shown in Fig. 3.18.

To evaluate the thermal/coherent behavior with respect to the temporal envelope of the pump pulse, we systematically scanned the entire pulses' time window in steps of 128 ps. The sub-window size, spanning 33% of the entire pulse, allowed us to gather sufficient statistics. It is worth noting that similar results were obtained with a 20% sub-window size, albeit with no qualitative difference. The $g^2(0)$ was determined for each sub-window position, so as to compute the $g^2(t, \tau = 0)$ across the entire pulse duration as illustrated in Fig. 3.19. In the case of pulsed excitation, where the pump power changed over time (Fig. 3.18), the output of the metallic coaxial nanolaser exhibited, as expected, a delayed but rapid transition from thermal to coherent behavior based on the instantaneous value of the pump pulse temporal envelope (Fig. 3.19 (a)).

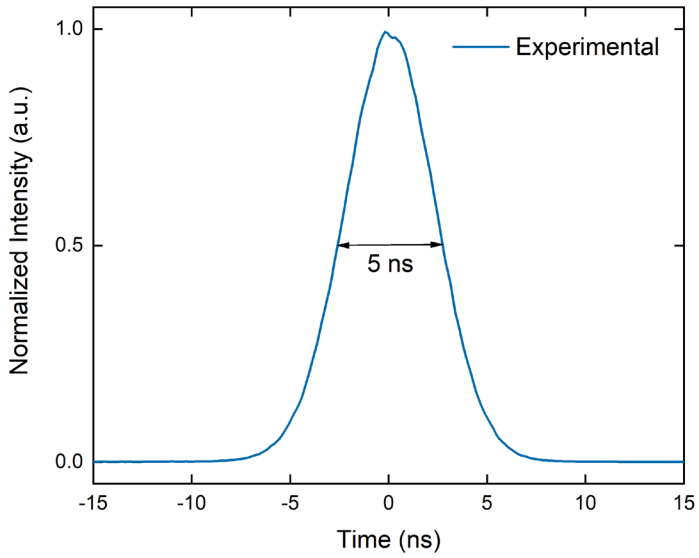

Fig. 3.18: **Temporal profile of the pump pulse.** Pump pulse at 1064 nm and1 MHz repetition rate, featuring a Gaussian profile with FWHM = 5 ns obtained from single-photon detector measurements. **(30)**

In the below-threshold regime (~ 170 μW), the response was mostly thermal at the wings of the pulse, with $g^2(t, \tau = 0) > (1.6 \pm 0.05)$, whereas towards the center it reached values close to $g^2(t, \tau = 0) = (1.25 \pm 0.01)$ (see Fig. 3.19 (b), black curve). In the above-threshold regime (~ 595 μW), the $g^2(t, \tau = 0)$ decreased from (1.5 ± 0.06) to (1.01 ± 0.01) (see Fig. 3.19 (b), green curve), still exhibiting a thermal

behavior at the edges, which was notably less pronounced than in the below-threshold regime (green and yellow curves).

The leading edge of the pump pulse generated carriers in the higher quantum well (QW) or barrier states, which rapidly relax into the lower QW states yielding spontaneous emission ($g^2(0) > 1$) (137, 138). As the intensity of the pump pulse increased over time, population became sufficiently strong, driving the system into the regime of coherent emission ($g^2(0) = 1$) (137, 138). Since nanolaser cavities have an ultrafast response, at the trailing edge of the pulse envelope (where the intensity of the pump pulse is low), SE dominated over coherent emission, leading to $g^2(0) > 1$ (137, 138). Moreover, for higher excitation densities, stimulated emission was maintained for a longer time, hence resulting in an asymmetry in the time resolved data. It was also influenced by the amplitude fluctuations in the pump pulse train.

To visualize the difference in $g^2(t, \tau = 0)$ for the temporal edges and the center of the pulse, cross sections for various t are shown as a function of pump power as dashed, dotted and solid blue lines, respectively (see Fig. 3.19 (c)). It can be noted that the error margin for the $g^2(t, \tau = 0)$ at the pulse start and end was generally higher, as fewer number of photon coincidence events were recorded compared to the center of the pulse, where photon brightness was generally larger. While integrating for longer periods can enhance accuracy, it came at the expense of increased thermal effects on the metallic coaxial nanolaser.

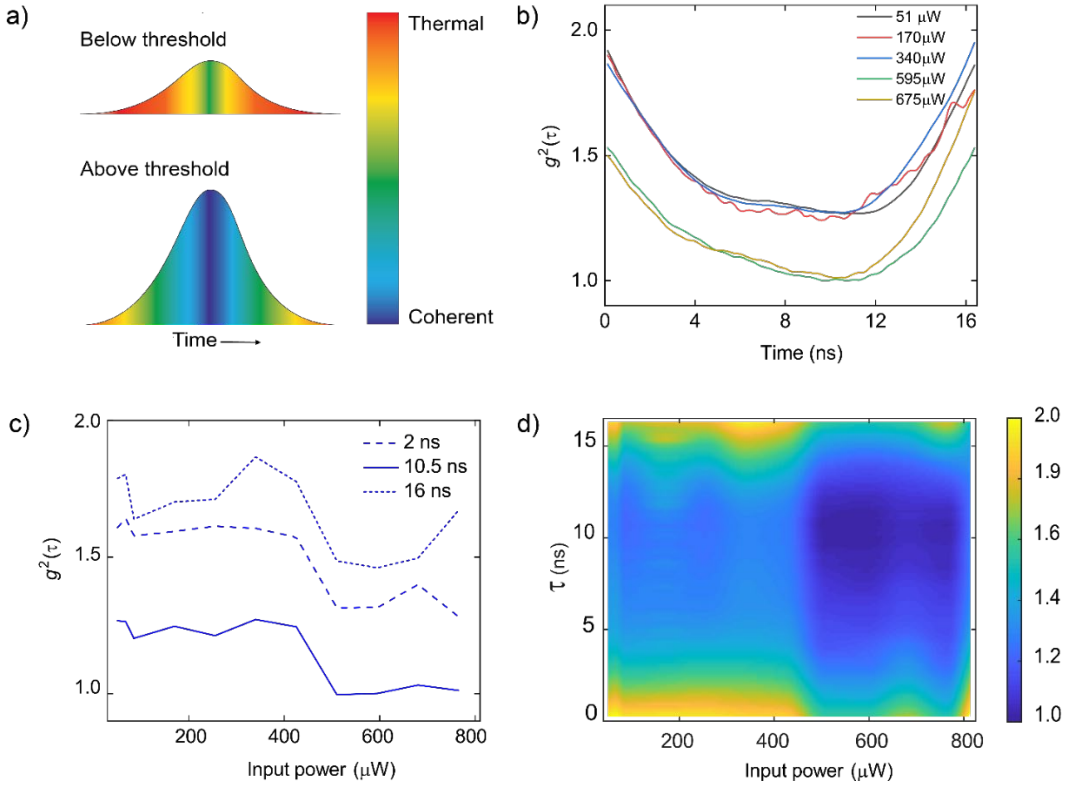

Fig. 3.19: **Time-resolved second-order correlation measurements.** a) Schematic of the expected photon statistic as a function of the emitted pulse's temporal envelope shown for two cases, above and below threshold. b) $g^2(t,\tau=0)$ evolution from a thermal (photon bunching) to a coherent behavior scanned over the emitted pulse length. c) $g^2(t,\tau=0)$ as a function of input power at various timings t. The edges of the pulse are shown in dashed and dotted lines (t= 2 ns, t =16 ns) while the center of the pulse (t = 10.5 ns), where the intensity of the pump pulse is maximum) is shown as a solid line. d) Color plot of $g^2(t,\tau=0)$ vs. the emitted pulse's temporal envelope for increasing pump powers. We note that, below threshold and for low pump powers, the response is mostly thermal. Above threshold, the output still presents a thermal behavior around the wings of the pump but is coherent in the center, as depicted in panel a). **(30)**

Thus, there exists a close relationship between the temporal profile of the pump laser and the emission characteristics of the metallic coaxial nanolaser. Using time-resolved second-order coherence measurement, we i) studied the nature of the nanolaser emission with respect to the temporal profile of the pump pulse and ii) mapped out the threshold as a function of both average pump power and instantaneous intensity (Fig. 3.19 (d)). The experimental results demonstrate that it is possible to switch the nanolaser emission between thermal and coherent by simply altering the temporal profile of the pump laser.

3.4 Conclusion

This project focuses on elucidating the fundamental emission properties of metallic coaxial nanolasers. Due to the specific architecture, the size of these lasers was reduced to subwavelength dimensions, which enhanced the Purcell effect with a large spontaneous emission factor, resulting in a thresholdless behavior. However, in a practical scenario, one should not confuse this feature with a hypothetical zero threshold. This encouraged us to conduct an elaborate study on metallic coaxial lasers in the classical and quantum domain under pulsed pumping conditions. The key objectives of this project were to 1) Demonstrate the limits of classical characterization in describing the emission behavior, 2) Determine the threshold of nanolasers via photon statistics, and 3) Study the emission behavior within the nanolaser output by performing time-resolved photon statistics.

For classical characterization, we studied spectral properties such as the emission wavelength, the linewidth narrowing and the $L-L$ curve of the nanolaser emission. The emission wavelength of the metallic coaxial nanolaser was found to be at ~1300 nm. However, in the metallic coaxial nanolaser, the linewidth of the emission increased with the power due to refractive index fluctuations and self-heating effects, which is not typical for a semiconductor laser. Moreover, a blue-shift of the emission wavelength was observed with increasing power, which was attributed to the saturation and spill out of free carriers from the energy states in the quantum well. Furthermore, the $L-L$ curve obtained for the metallic coaxial nanolaser was a straight line demonstrating a thresholdless behavior. This uncertainty and ambiguity in the determination of the nanolaser threshold via classical characterization techniques motivated us to perform second-order correlation measurements via Hanbury Brown and Twiss experimental setup. We determined $g^2(0)$ for various input powers and found that the value of $g^2(0)$ reached near unity at ~420 μW, marking the threshold of the nanolaser. In addition, we characterized the width of the normalized correlation peak for different pump powers so as to track the transition from thermal to coherent behavior because the FWHM was influenced by the pump pulse and photon lifetime (126). To investigate the dynamics of emission within the nanolaser output, we studied the time-resolved second-order correlation function ($g^2(t,\tau=0)$) by sliding narrower time windows across the entire pulse temporal envelope. This time-resolved study demonstrated that the emission from the metallic coaxial nanolaser, even at higher input powers, was comprised of spontaneous and stimulated emission. Furthermore, it was possible to switch between thermal and coherent within the nanolaser, by simply altering the temporal profile of the pump laser.

The experimental results presented in this chapter are a step towards the development of photonic integrated circuits, which is envisioned to replace electronic circuits. However, practical applications of these devices are still limited due to immature fabrication technologies. One of the biggest challenges is the

integration of nanolasers into photonic integrated circuits, particularly achieving efficient coupling between the nanolaser output and silicon waveguides. This process is hindered by insertion losses stemming from the highly divergent emission profile and the broadband nature of the near-IR output. An interesting solution involves incorporation of solid immersion lenses (139), which are commonly used to enhance the coupling between nano-emitters and integrated devices (139), and yet have never been used in combination with nanolasers. Adapting this technique to nanolasers could facilitate precise focusing of their strongly divergent emission cone into silicon waveguides, thereby overcoming key integration barriers and paving the way for a new class of compact, high-performance on-chip light sources.

4 CHARACTERIZATION OF TIME-BIN ENTANGLED STATES

Chapter abstract:

In this chapter, we delve into the application of photon statistics in quantum technologies. We generate high-dimensional time-bin entangled states in a synthetic photonic lattice, which has practical applications in quantum communication, computation, sensing, and other areas. The chapter starts with an overview, covering the background, the issues addressed, and the proposed solutions. Subsequently, we expound on the fundamental principles underlying the project and detail the experimental methods employed in the project. Then, we present the results obtained and conclude with a discussion and summary of our work.

Chapter content:

4.1 Overview

Approximately half a century ago, extensive investigations into the quantum properties of light began, resulting in notable progress that allows for precise control of quantum optical systems and sets the stage for quantum state engineering. Significant developments in quantum optical techniques have enabled the practical implementation of conceptual experiments that are tailored to probe the core principles of quantum theory. This enhanced control over quantum phenomena offers exciting opportunities to explore novel information processing approaches, with the potential to revolutionize technologies rooted in quantum information science.

One of the most important resources in quantum technology is entanglement, a purely quantum phenomenon which refers to the correlation between two or more quantum systems, where the state of one system cannot be described independently of the other (140, 141). This phenomenon offers unique advantages in quantum information science, including quantum computation (25, 26, 142), quantum communication (16, 17), quantum simulation (70), and quantum metrology (25). Entanglement provides the key to achieve 'quantum supremacy' (25, 140, 143–145), particularly in systems utilizing qubits. A qubit, a two-level system, is the basic unit of information in quantum technology (146).

Quantum information can be encoded in various physical systems, such as Rydberg atoms (147), trapped ions (148), defects in solid-states (149), polar molecules (150), and photons (151). Among these, photons are particularly suitable due to their advantageous properties such as high speed, minimal interaction with the environment, long coherence times, and well-established technologies for the generation, manipulation, and detection of photons (152–154). Moreover, they possess several internal as well as external degrees of freedom. Internal degrees of freedom include polarization (12, 155), orbital angular momentum (156), frequency (157) and generation time (158), while the external degrees of freedom include the spatial position and the path traveled by a photon (76, 159, 160).

Early experiments exploring quantum entanglement employed polarization, optical paths, and orbital angular momentum modes in free space. However, advancements in fiber-based telecommunications have shifted focus to more robust and fiber-compatible degrees of freedom, such as frequency (151) and time (16, 158, 161, 162). The concept of using time-bins to carry quantum information was first proposed in 1989 (163) and subsequent experiments successfully demonstrated two-dimensional time-bin entanglement (16, 164). To create entanglement between two photons and encode quantum information in the time-bin domain, two indistinguishable laser pulses separated by a fixed time difference are utilized (16). Each laser pulse generates photon pairs using nonlinear light sources base on, e.g., spontaneous parametric down-conversion (SPDC) (165, 166) and spontaneous four-wave mixing (SFWM) (167, 168), as well as on other

platforms, such as quantum dots (169–174), ions (175, 176), color centers (177–179) and ensemble of atoms (180–182).

For applications like quantum communication or quantum computation, high-dimensional quantum systems, or qudits, offer advantages over qubits due to their higher information capacity, enhanced security and resilience to noise (183, 184). Consequently, high-dimensional quantum entanglement provides a rich area for both fundamental research and technological innovation (Fig. 4.1) (146, 151).

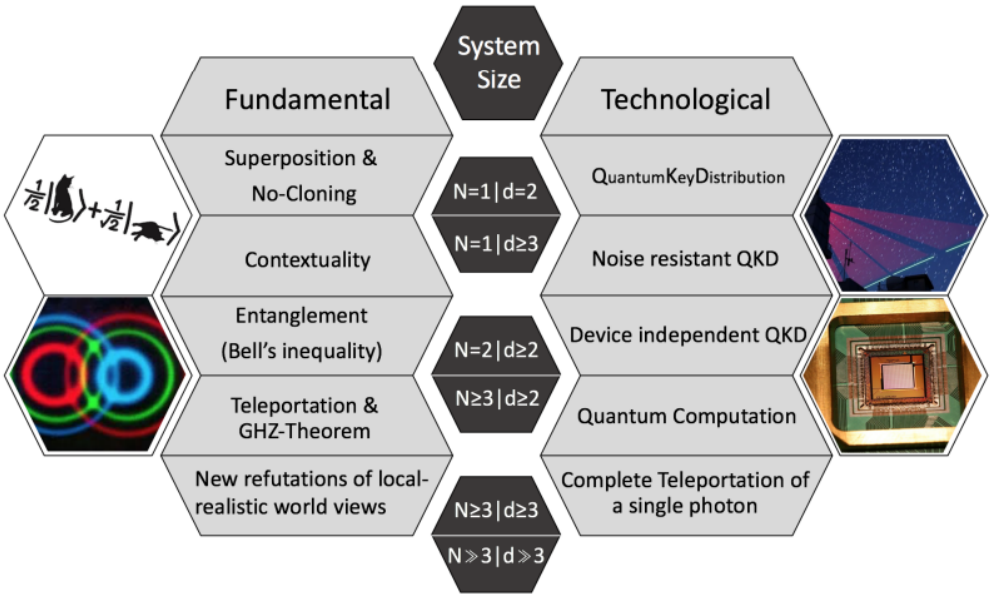

Fig. 4.1: **Fundamental quantum properties and associated technological applications as a function of system dimensionality.** Reproduced from **(146)** with permission from Springer Nature, © 2020 Springer Nature.

In principle, the dimensionality of the time-bin entangled states can be scaled up by increasing the number of indistinguishable pulses (185) as demonstrated in Fig. 4.2. For example, eight distinguishable pulses can create an eight-dimensional time-bin entangled state. Higher-dimensional time-bin entangled states have been realized in free-space (186–188), on-chip platforms (167), and optical fiber systems (31, 189–191). This scalability offers exciting possibilities for quantum information processing, making it a valuable approach for quantum communication.

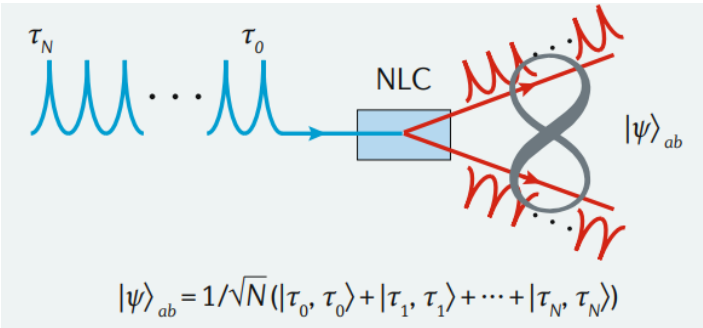

Fig. 4.2: **Generation of high-dimensional time-bin entangled states.** Here, N indistinguishable pulses produce N-dimensional entangled states. Each pulse probabilistically generates a photon pair at time τ_i, resulting in a high-dimensional time-bin entangled state $|\psi\rangle_{ab}$. Reproduced from **(146)** with permission from Springer Nature, © 2020 Springer Nature.

However, characterization of these entangled states requires estimation of numerous parameters, such as the multiple phase values that arise from delays between pulses. The estimation process demands a large number of measurements, which becomes impractical as dimensionality increases. Experimental limitations further constraints efficient entanglement processing. Characterization of a high-dimensional time-bin entangled state typically involves the utilization of cascaded unbalanced interferometers (192, 193), where each interferometer measures the phase between two time-bins. Thus, the realization of a N-dimensional time-bin entangled state requires $N - 1$ interferometers, which becomes infeasible for large N (Fig. 4.3). Moreover, this results in significant experimental complexity and cost. Therefore, efficient and innovative methods to generate and process high-dimensional time-bin entangled states, particularly in optical fibers, are crucial for practical quantum communication.

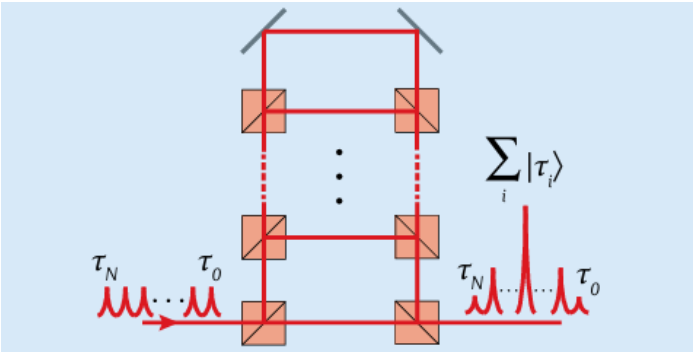

Fig. 4.3: **Characterization of high-dimensional time-bin entangled states.** The characterization of high-dimensional time-bin entangled states requires multiple unbalanced Mach–Zehnder interferometers, enabling the coherent superposition of time bins at the central bin of the interferometer output. **(146, 163)**. Reproduced from **(146)** with permission from Springer Nature, © 2020 Springer Nature.

In our work, we implement a fiber-based unbalanced interferometer to generate and process high-dimensional time-bin entangled states through quantum walks. Quantum walks, the quantum analog of the classical random walks, rely on interference and superposition (56, 57, 63, 76). As a generalized measurement device, they effectively describe the transport of entangled photons in optical fiber networks (54, 56). For example, a coupled fiber loop system, which simulate a synthetic photonic lattice (SPL), has been extensively employed to study the nonlinear propagation of light through quantum walks (194–197). However, the application of such systems in quantum information processing and quantum technologies remains largely unexplored, presenting an opportunity to further investigate how time-bin entangled states and quantum walks can be integrated within optical fiber networks. This approach will potentially unlock new capabilities in quantum communication and processing.

In this chapter, we focus on three main objectives: first, to simulate SPL using a coupled fiber-loop system; second, to generate high-dimensional time-bin entangled states in the SPL; and finally, to process these entangled states through various quantum walk protocols. Our work aims to provide significant applications in quantum technologies, offering new pathways for generating and processing quantum information.

4.2 Theory and Method

This section covers the employed theory and methods to gather and analyze the experimental results presented in section 4.3. We begin with the generation of photonic entangled states, in particular, time-bin entangled states, via spontaneous parametric down conversion process. We also describe the basics of quantum walk in synthetic photonic lattice (SPL) through which we process the generated entangled state.

4.2.1 Generation of time-bin entangled states

Time-bin entanglement

Entanglement-based quantum information protocols including quantum communication, teleportation, and entanglement swapping for long distance communication are mainly mediated through optical fibers (158, 161, 162, 198, 199). Among various types of entanglement, time-bin entanglement are both known for their robust nature, and immunity to polarization mode dispersion that causes decoherence during transmission, particularly in fibers (158). Time-bin entangled states are a discrete version of energy-time entanglement (16, 200), which typically comprises two qubits that are in a superposition of two temporal modes (bins). However, a necessary condition to be satisfied for entanglement generation using time qubits is that the temporal separation between the two time modes must be larger than the coherence time of the interacting photons. This typically requires a pulsed operation of quantum photonic sources like PPLN (11).

Pumping scheme: A standard pumping method involves the use of an unbalanced Mach-Zehnder interferometer (MZI), which is injected with either a picosecond or femtosecond pulse. Standard unbalanced MZIs feature two beam-splitters coupled together by a long and a short arm. The first beam-splitter divides an input pulse into two pulses of equal amplitude, one of which travels through the long path and the other through the short one. This induces a relative phase θ between the two paths. The two pulses are then recombined by the second beam-splitter to produce a pulse doublet, $\alpha|E\rangle + \beta e^{i\theta}|L\rangle$, where $|E\rangle$ and $|L\rangle$ denotes the early and late pump pulses, and α and β are their corresponding probability amplitudes. In an ideal system, the beam-splitters will possess a perfect coupling ratio, thereby resulting in $\alpha = \beta$, meaning both output pulses are perfect copies of each other in terms of amplitude.

Interferometers are used to perform phase-sensitive measurements; hence it is a common practice to introduce an element for phase tuning such as a phase-shifter or an electro-optic phase modulator (157, 200, 201). This is illustrated in Fig. 4.4, where an additional phase ϕ is applied between the two pulses (16). The output from the interferometer then takes the form,

$$\alpha|E\rangle + \beta e^{i(\theta+\phi)}|L\rangle. \tag{4.2.1}$$

For simplicity, the overall phase term is denoted as φ, where $\varphi = \theta + \phi$.

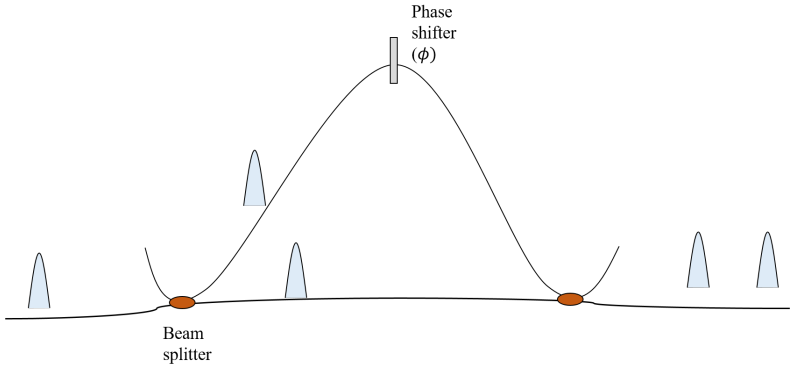

Fig. 4.4: **Schematic of a Mach-Zehnder interferometer to generate twin pulses.** The laser pulse is sent to the device (left to right in the figure) and is split to travel both a short and along arm. By adjusting the coupling ratio in the beam splitter and the phase $\boldsymbol{\phi}$ of the phase shifter, any superposition of the basic states $|\boldsymbol{E}\rangle$ and $|\boldsymbol{L}\rangle$ can be prepared and analyzed. The delay between the pulses is equal to the difference in the length of the arms.

Entanglement generation: When a twin pump pulse passes through a nonlinear medium, for example, a PPLN waveguide, SPDC process generates signal and idler photons that exist in a superposition of two time modes. The resultant state is time-bin entangled, and is given by $|\psi\rangle = \alpha|E\rangle_s|E\rangle_i + \beta e^{i\varphi}|L\rangle_s|L\rangle_i$, where s and i are the signal and idler photons, respectively (16). For the optimal generation of time-bin entangled states, the probabilities for generating early and late photon pairs are equal, resulting in the state,

$$|\psi\rangle = \frac{1}{\sqrt{2}}\left(|E\rangle_s|E\rangle_i + e^{i\varphi}|L\rangle_s|L\rangle_i\right). \tag{4.2.2}$$

Entanglement verification: The existence of entanglement in the generated quantum state (Eq. 4.2.2) can be verified through quantum interference measurements (163). The measurement involves sending a photonic quantum state into an interferometer and then performing coincidence measurements for various delay/phase values. It serves as the foundation for several applications leveraging optical quantum states. Moreover, it facilitates applications in quantum cryptography (18), quantum metrology (202), and quantum computation (142).

The two-photon time-bin entangled state, $|\psi\rangle = \frac{1}{\sqrt{2}}\left(|E\rangle_s|E\rangle_i + e^{i\varphi}|L\rangle_s|L\rangle_i\right)$, when passes through a MZI results in a quantum interference pattern with twice the periodicity compared to quantum interference with a single photon. The visibility, V_2, of the quantum interference can then be defined, and a function, $C_{D=2}(\phi) \propto 1 + V_2\, cos\,(2\phi)$, can be fitted to the measured quantum interference. The V_2 can also be determined via $(I_{max} - I_{min})/(I_{max} + I_{min})$, where I_{max} and I_{min} are the maximum and minimum intensity or coincidences obtained from the quantum interference fringes. If the measured visibility exceeds

$V_2 > \frac{1}{\sqrt{2}}$, it confirms the quantum properties of the qubit system as it violates the Bell's inequality threshold (203, 204).

For a four-dimensional time-bin entangled state, quantum interference $C_{D=4}(\phi) \propto 4 + 2V_4 \cdot [3cos\,(2\phi) + 2cos\,(4\phi) + cos\,(6\phi)]$. If $V_4 > 0.8170$, it violates the Collins-Gisin-Linden-Massar-Popescu (CGLM) inequality and confirms entanglement (205–207).

However, generating and processing four-dimensional states is not straightforward. To overcome this challenge, we turn to quantum walks, which provide a robust and efficient method for generating and manipulating high-dimensional entangled states. This technique allows us to explore the quantum properties of systems with dimensions beyond those easily achievable through conventional interference setups.

Discrete-time quantum walk (DTQW)

A DTQW is often implemented in the path degree of freedom (63, 208–210), where the walker's propagation leads to interference effects, resulting in interesting spatial distributions. This is achieved using a spatially organized pyramid of beam splitters, as shown in Fig. 4.5. Beam splitters within the pyramid act on the walker, transforming its initial state into a position-dependent probability distribution outcome. The final position of the walker is determined by its initial state as well as the transformations imposed by the platform, typically in the form of beam splitting operations (50–52). However, constructing such a pyramid of optical free-space beam splitters presents experimental challenges, due to the exponential increase in the number of components, such as detectors and beam splitters with each increasing step.

Quantum walks have also been realized using photonic structures, which are materials or devices that are utilized to manipulate the behavior of light depending on their geometric dimensionalities (35). A few examples for photonic structures are multi-path waveguides (211) as well as 2D photonic crystals and metamaterials (212, 213). Unfortunately, these structures are limited to a maximum of three spatial dimensions, constraining many technological applications to lower-dimensional devices. Therefore, a suitable alternative is to employ a synthetic photonic lattices (SPLs) for practical and scalable quantum walk implementations.

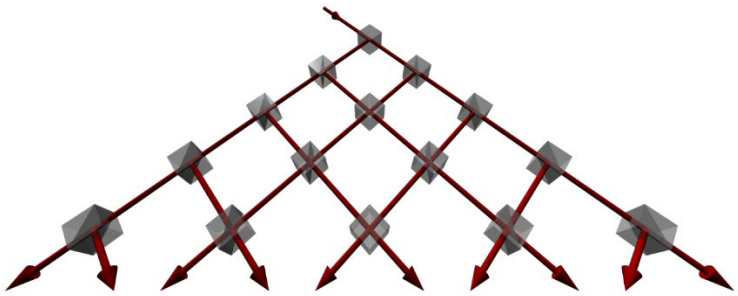

Fig. 4.5: **The beam splitter cascade.** Each beam splitter splits the incident beam equally in two different directions. When two light beams reach the beam splitter at the same time, they give rise to interference. This interference continues to influence the spatial distribution of the light beams from the third step onward. Reproduced from **(63)** under the CC BY-NC-ND 3.0 license.

4.2.2 Synthetic photonic lattice

A synthetic space is created by utilizing non-spatial/internal degrees of freedom of the walker either by replacing or integrating the geometrical degrees of freedom. Moreover, quantum walks in SPLs offer a powerful tool for exploring the complex interplay between quantum mechanics and optics, with implications in fundamental science, e.g., understanding quantum superposition and interference effects, as well as practical technologies such as quantum computation and simulation (214), providing a resource-efficient scalability in quantum information processing.

The creation of a synthetic space can be done in two ways, either forming a lattice or exploiting the parameter dependency of the system (35, 215). In the former way, the dimensionality of the SPL is determined by the coupling between a set of photonic states. For instance, these can be represented by red spheres as illustrated in Fig. 4.6 (a). A one-dimensional photonic lattice is formed when there is a nearest-neighbor coupling, i.e., the sphere labelled 1 is coupled to sphere 2, sphere 2 is coupled to sphere 3, etc., as shown in Fig. 4.6 (b). On the other hand, a higher-dimensional photonic lattice is formed when there is long-range coupling between the photonic states as illustrated in Fig. 4.6 (c). For example, if one considers optical modes at different frequencies as red spheres and they are coupled in such a way that the energy in one mode can be transferred to nearby modes or between them, along the frequency axis of light, it forms a one-dimensional lattice (215).

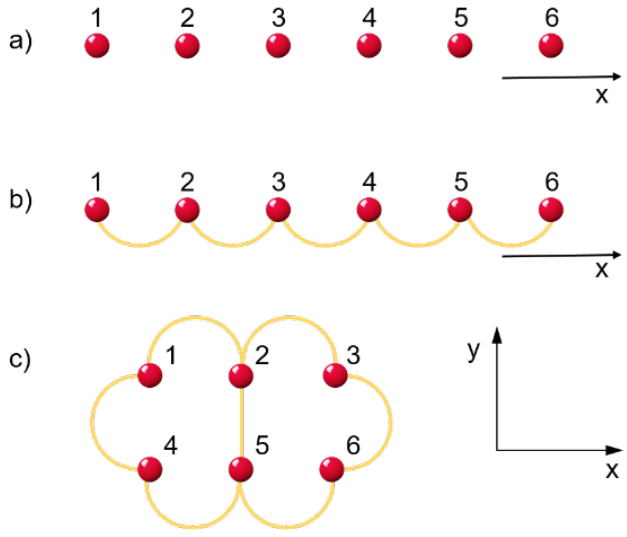

Fig. 4.6: **Synthetic lattice space:** (a) Consecutive integers are used to label photonic states. (b) One dimensional synthetic lattice is created by the between nearest-neighbor photonic states (coupling between 1 and 2, 2 and 3, and so on). (c) Two dimensional synthetic lattice is generated via long-range coupling between different photonic states (coupling between 1 and 2, 2and 3, 1 and 4, 3 and 6, etc.) **(35)**.

The second way of creating a synthetic space involves utilizing parameter degrees of freedom. Let us consider a physical system in n-dimensional space, which is described by the Hamiltonian, $H(p_1, p_2, \dots, p_m, r_1, r_2, \dots, r_n)$, where $p_1, p_2, \dots, p_m$ are external parameters and $r_1, r_2, \dots, r_n$ are spatial parameters. In this approach, each parameter in the Hamiltonian contributes to a synthetic dimension. This means that the parameter dependence of the system can be described with a new axis, the p-axis, as a supplementary synthetic dimension alongside the conventional physical space, resulting in a higher-dimensional synthetic space (35).

SPLs using photonic degrees of freedom

SPLs, realized by utilizing photonic states (Fig. 4.7), provide a diverse range of additional degrees of freedom that can be precisely manipulated, effectively serving as synthetic dimensions. By utilizing one or more of these degrees of freedom and by appropriately coupling the corresponding states, one can introduce enhanced dynamics in this space, expanding the effective dimensionality of the system. One of the accessible degrees of freedom is polarization, which introduces an additional dimension with two basis states (35, 36). The continuous conversion between these polarization directions during propagation results in the coupling between the two lattices by means of a superposition of polarization-entangled eigenstates[1] (36).

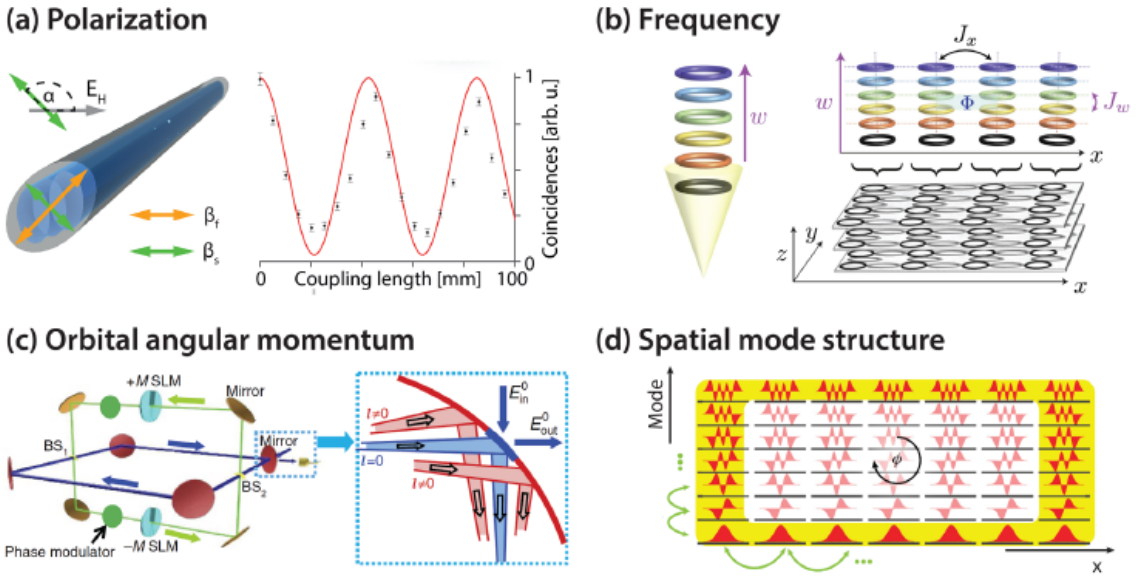

Fig. 4.7: **Synthetic photonic spaces.** a) Polarization of a photon employed for synthetic dimension generation. b) Equidistantly spaced modes of a ring resonator, coupled through periodic modulation synchronized with the

[1] If equation of the Hamiltonian is given by $\hat{H}|E_n\rangle = E_n|E_n\rangle$, then $\hat{H}$ is the operator, $|E_n\rangle$ is the eigenstate and E_n is the eigenvalue (216).

round trip time. c) Optical resonators enabling coupling of different orbital angular momentum modes through spatial light modulators. d) Equidistant energetic separation of spatial modes serving as a synthetic dimension. **(36, 217–219).** Reproduced from **(36)** under the CC BY-NC license.

The spectral degree of freedom is an another common way to enable SPLs due to the natural support of different frequency modes in photonic architectures, such as microring resonators (215). These modes can be coupled to create a lattice by dynamically modulating the structure using nonlinear optical methods (35, 215), for example, by incorporating electro-optic modulators (220). Waveguides are another platform which can be utilized to generate frequency synthetic dimensions, as they support the propagation of modes across a spectrum of frequencies (215). By combining input frequencies with traveling-wave modulation, it becomes possible to define the frequency grid for such systems (215). Furthermore, the orbital angular momentum introduces another avenue, where appropriately driven spatial light modulation enables selective conversion of portions of a beam into modes with higher or lower orbital angular momentum, thereby establishing a lattice model in this dimension (36). Additionally, the spin angular momentum of photons contributes to dynamics in this space through spin-orbit coupling (36). Utilizing the spatial degree of freedom available in optical modes can also generate synthetic dimensions (36).

In this study, SPLs have been implemented by harnessing the temporal degrees of freedom. The propagation of pulses within these lattices is modeled analogously to the movement of walkers navigating discrete lattice sites. Specifically, the roundtrip or iteration and arrival times of the pulses define the time-step (t) and synthetic position (x) in the synthetic photonic lattice, respectively. This temporal framework provides a unique perspective as it explores the dimensionality enhancement through the application of time-division multiplexing, a technique widely employed in optical telecommunication for bandwidth optimization (36, 63). The method involves organizing signals into distinct time slots and transmitting them through optical fibers. At the receiving end, pulse separation based on individual arrival times allows direct detection. This technique is a widely adopted approach in optical telecommunication aiming to increase the bandwidth of communication channels to meet the growing demand for higher information capacities (70, 221, 222).

4.2.2.1 Coupled fiber-loop system

A coupled fiber-loop system featuring two fiber loops of different lengths, connected with a dynamic optical switch (Fig. 4.9 (a)) has been utilized in this study to implement SPL to perform DTQW in the temporal domain (194). The optical switch is an electro-optic component that can control the proportion and direction of the light flow in accordance with an external voltage signal. The response of an

optical switch with respect to voltage was investigated by measuring the optical output at one of the ports using a fast photodiode, the results of which is shown in Fig. 4.8.

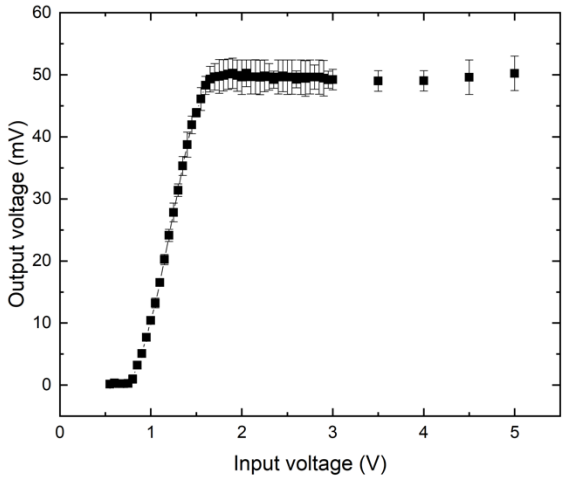

Fig. 4.8: **Response of an optical switch.** An external voltage (shown on the x-axis) is used to control the optical switch. The power output from one of the switch ports was directed to a photodiode, whose the output voltages were measured for different input voltages. The graph shows that for voltages below 0.9 V, no output is observed from this port, indicating that the light is directed through the other port. Conversely, for voltages above 1.8 V, the device completely switches to the opposite port. Around 1.6 V, the optical switch behaves like a 50-50 beam splitter.

In the coupled fiber-loop system, the time taken by light pulses to propagate through long and short loops are denoted by T_L and T_S, respectively, have a time difference of $T_L - T_S = \Delta T$ and average time of $\frac{T_L+T_S}{2} = \bar{T}$. The lengths of the loops are designed such that $\bar{T} > \Delta T$, which corresponds to a maximum number of pulses the system can accommodate, $N = \frac{\bar{T}}{\Delta T}$. N is tailored to the required dimensionality of the system, which is designed to a particular application, here, generation and processing of high-dimensional time-bin entangled states.

The propagation of the light pulse in the coupled fiber-loop system is illustrated in Fig. 4.9 (b) and (c). When a light pulse is injected to into the coupled fiber-loop system, for example, through the long loop, it reaches the optical switch, which acts as a 50-50 beam splitter. This results in the creation of two identical pulses with half the amplitude of the original pulse, of which one propagates in the long loop and the other in the short loop. The two pulses then return to the optical switch, however, at different times, owing to the length difference of ΔT between the long and short loops. The optical switch, still set to behave as a 50-50 splitter, divides each pulse into two pulses, providing a pulse doublet in both the long and short loops. Then, light undergoes another roundtrip in the fiber loops. On reaching the optical switch, the first pulse from the long loop and the second pulse from the short loop interfere, as they reach the coupler at the same time.

This interference results in the distribution of the constructive and destructive interference components over the long and short loops (194).

Thus, the number of pulses in each loop can be increased as a function of number of roundtrips, thereby allowing for the easy scalability of the system. Here, the time-step (t) corresponds to each roundtrip, while the synthetic position (x) is defined by the arrival time of the pulses within the lattice. This association establishes a temporal framework, where each roundtrip contributes to the progression of the synthetic position in the synthetic photonic lattice.

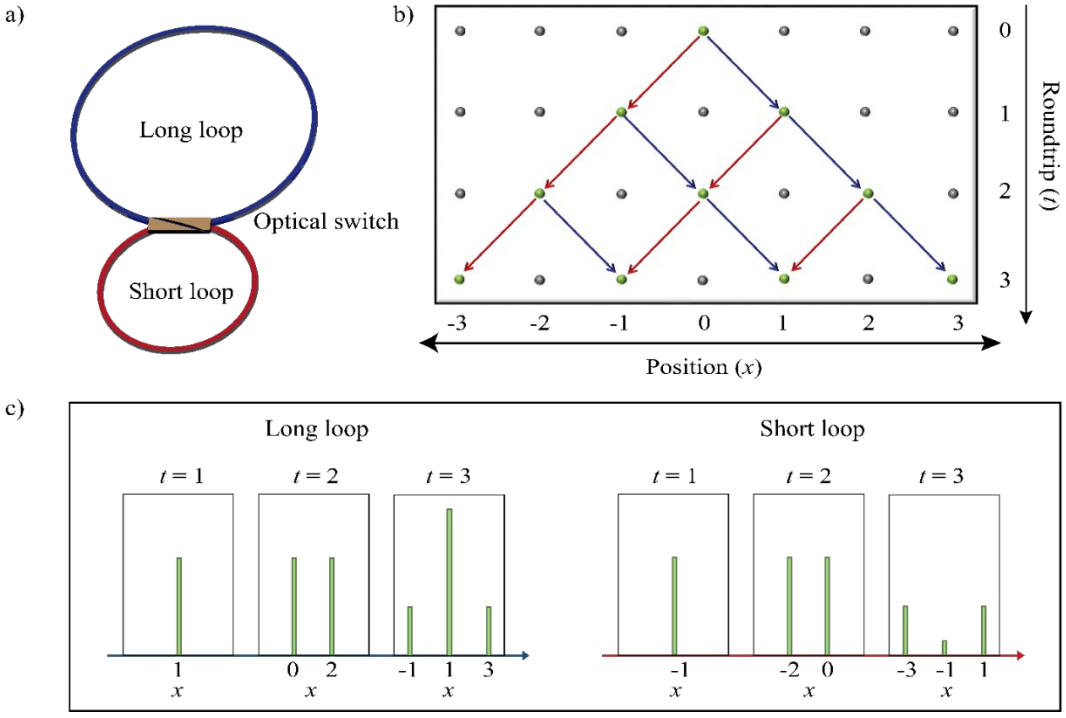

Fig. 4.9: **Coupled fiber-loop system and quantum walk** a) Coupled fiber-loop consisting of two fiber loops of different lengths coupled with an optical switch. b) Quantum walk describing the propagation of the light pulse in the coupled fiber-loop system when the optical switch is configured to a 50-50 beam splitter. c) A pictorial representation of pulses in the long and short loops in roundtrips, t = 1, 2 and 3.

Time-division multiplexing schemes in coupled fiber-loop exhibit significant potential for future extensions, offering exceptional scalability, stability, and flexibility. Through active modulation of both amplitude and phase, it becomes possible to introduce real and imaginary on-site terms into the associated Hamiltonian, allowing dynamic adjustments for individual sites across synthetic space and time. Leveraging these capabilities, photonic time-division multiplexing schemes have been used to provide diverse phenomena in the classical domain. For instance, the realization of parity-time (PT) symmetry in

such systems has been explored, where PT symmetry refers to a property wherein the Hamiltonian remains unchanged under combined parity and time reversal operations. The PT-symmetry in the coupled fiber-loop system was initially studied by A. Regensburger et al. (195) and A. L.M. Muniz et.al. (223), who extended it to a two-dimensional synthetic lattice. PT symmetry was implemented in the system by incorporating tunable gain, loss, and phase structure. Furthermore, experiments by A. Basinov et al. (224) have demonstrated anomalous Floquet interface states in such systems. Additionally, studies on photon-photon thermodynamic processes (225), superfluidity of light (197) and Bloch oscillations (196) were conducted in the coupled fiber-loop system.

Our group has initiated research into the potential of coupled fiber-loop systems for quantum applications. We have successfully generated and confirmed two-level and four-level time-bin entanglement using DTQW and controlled quantum walk techniques in (31, 226, 227) and is discussed in this thesis.

4.2.2.2 Quantum walks in the SPL

The wave function of the light pulse in this system is defined by

$$|\psi\rangle = \sum_x \sum_c A_{x,c} |x\rangle \otimes |c\rangle \tag{4.2.3}$$

where $A_{x,c}$ is the complex amplitude of the wave function in its position $|x\rangle$ and coin state $|c\rangle = \{|l\rangle, |s\rangle\}$. The states $|l\rangle$ and $|s\rangle$ describe the configurations in which the light pulse travels in the long and short loops, respectively. The full evolution of the controlled quantum walk in a coupled fiber-loop system can be represented by the coin and step operators, $\hat{C}$ and $\hat{S}$. The coin operation in the SPL on each step is described as $(|x\rangle\langle x| \otimes \hat{C})|\psi\rangle$, with general unitary coin operation,

$$\hat{C} = \begin{pmatrix} cos\alpha & isin\alpha \\ isin\alpha & cos\alpha \end{pmatrix} \tag{4.2.4}$$

where α is the rotation parameter that dictates the coin operation (57).The step operator is still given by Eq. 2.4.5, and depicted as follows using the notations of the coupled fiber-loop system.

$$\hat{S} = \sum_x |x+1\rangle\langle x| \otimes |l\rangle\langle l| + |x-1\rangle\langle x| \otimes |s\rangle\langle s| \tag{4.2.5}$$

Controlled quantum walk

A DTQW is considered as a generalized measuring device (228) that can provide Positive Operator-Valued Measures (POVMs) (25, 229). POVMs (25, 229) comprise a collection of positive operators, denoted as $\{\Pi_x\}$, which represent the potential outcomes of a measurement. For instance, when a measurement described by the operator M_x is applied to a quantum system in the state, $|\psi\rangle$, the probability

of obtaining the outcome x is calculated as $P(x) = \langle\psi|{M_x}^\dagger M_x|\psi\rangle$. Each operator, $\Pi_x = {M_x}^\dagger M_x$, corresponds to an outcome, and they collectively satisfy the condition $\sum_x \Pi_x = I$, where I is the identity matrix (25, 229). POVMs and their applications in quantum information processing (230), non-locality of quantum states (231), optimal quantum-state tomography (232), quantum state discrimination (233) as well as in quantum metrology (202) have been theoretically studied. However, implementing them experimentally in any optical system is still a challenge (234). In classical schemes, optimizing interference operations may not be essential because it is possible to increase light intensity via optical amplification. However, in the quantum realm, such optimizations are not possible. In such scenarios, engineering $\hat{C}$ or, in other words, controlled quantum walks, becomes important as it allows us to achieve quantum interference involving all the photons in the initial state, thus providing POVMs.

Here, we explore a controlled quantum walk, where the evolution of light pulse is influenced by an external control mechanism (coupling ratio of optical switch), to employ a measurement scheme and achieve quantum interference of high-dimensional time-bin entangled states. The term 'controlled' refers to the manipulation of external parameters to guide the evolution of the quantum walk, providing a programmable behavior compared to standard DTQW. A conventional DTQW in a coupled fiber loop system produces the characteristic pattern depicted in Fig. 4.9 (c). However, by exploiting the dynamic capabilities of an optical switch (Fig. 4.8), one can tailor the pulse propagation to investigate intriguing interference effects across various time modes.

The coin operator, which describes the optical switch, takes different settings based on the target quantum walk scheme. Recalling Eq. 4.2.4, these settings can be implemented by modifying the rotation parameter, α. To employ a controlled quantum walk, three coin operations are introduced, i.e., for $\alpha = \frac{\pi}{2}$, $\frac{\pi}{4}$, and 0, which gives the Reflection $\hat{R}$, Fourier $\hat{F}$, and Transmission $\hat{T}$ coin operations, respectively, such that:

$$\hat{R} = \begin{pmatrix} 1 & 0 \\ 0 & 1 \end{pmatrix} \qquad \hat{F} = \frac{1}{\sqrt{2}}\begin{pmatrix} 1 & i \\ i & 1 \end{pmatrix} \qquad \hat{T} = \begin{pmatrix} 0 & i \\ i & 0 \end{pmatrix} \tag{4.2.6}$$

When a light pulse residing in the long loop reaches the optical switch, if $\hat{C}(x,t) = \hat{T}$, a light pulse shifts from a long to a short loop, while for $\hat{C}(x,t) = \hat{R}$, it remains in the residing loop, that is, the long loop. Similarly, if the light pulse is in the short loop, $\hat{C}(x,t) = \hat{T}$ shifts it from a short to a long loop (Fig. 4.10 (a)), whereas $\hat{C}(x,t) = \hat{R}$, let the light pulse to remain in the short loop (Fig. 4.10 (b)). When the coin operator is set to $\hat{F}$, the optical switch functions as a 50-50 beam splitter and equally splits the light pulse into long and short loops (Fig. 4.10 (c)). The functions of operators are summarized in Table 4.1. These operations are utilized to control the quantum walk and to provide an optimal measurement for phase

sensing problems in quantum metrology. This contrasts with the scheme mentioned above where the optical switch acts solely as a 50-50 splitter, thus enabling the realization of only one coin operation, $\hat{F}$. After several time-steps (referred to as roundtrips in a coupled-fiber loop system), the evolution operator of the final state is given by,

$$|\psi_n\rangle = \left(\hat{U}\right)^t |\psi\rangle = \left(\hat{S}\hat{C}\right)^t |\psi\rangle. \tag{4.2.7}$$

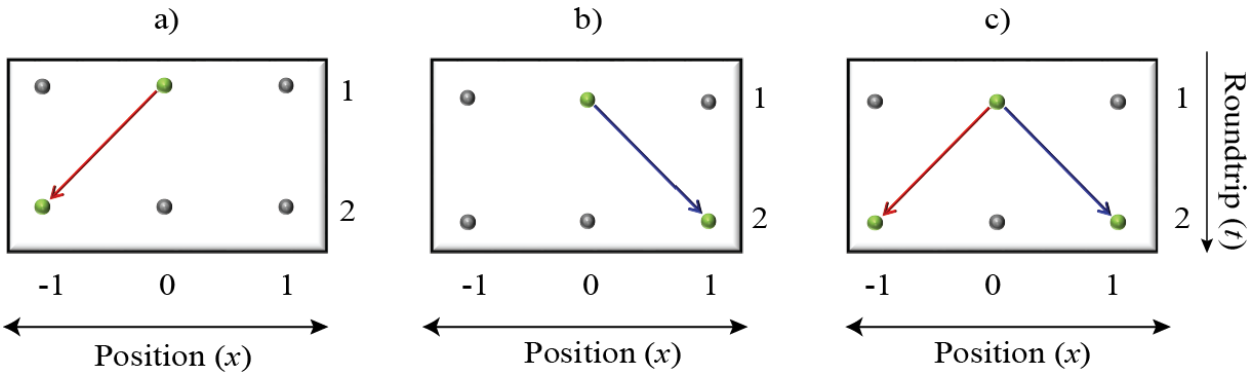

Fig. 4.10: **Operators and functions.** The panels above show the pulse shift when various operators act on them, where the red (blue) arrow indicates a short (long) loop. Here, we assume that the light pulse enters through the short loop. When the $\widehat{\boldsymbol{R}}$ (a) and $\widehat{\boldsymbol{T}}$ (b) operators act on the pulse in position $\boldsymbol{x = 0}$, the pulse moves to $\boldsymbol{x = -1}$ and $\boldsymbol{x = 1}$, respectively. c) When a light pulse acts under $\widehat{\boldsymbol{F}}$ (which resembles a 50-50 beam splitter), it splits equally and take the positions at $\boldsymbol{x = -1}$ and $\boldsymbol{x = 1}$.

Table 4.1: Operators and functions

Operator	**Function**
Transmission ($\hat{T}$)	Sends photons from one loop to the other
Reflection ($\hat{R}$)	Keeps photons in the same loop
Fourier ($\hat{F}$)	Acts as a 50-50 coupler, where 50% of photons is sent to both loops

4.3 Results and Discussion

This section presents the experimental setup and main results of the characterization of time-bin entangled states. The coupled-fiber loop system was utilized for the generation and processing of the entangled state, along with photon statistics to analyze the correlation of entangled photons.

4.3.1 Experimental setup

One of the most common methods to generate and characterize time-bin entangled states is via the use of MZIs. The wavefunction of a time-bin entangled quantum state is presented in Eq. 4.2.2. Interferometers allow for the creation of photonic superpositions, a key aspect for the measurement of entanglement in the temporal domain. This is enabled by mixing early and late time modes, via carefully engineering of the interferometric design such that the photons are temporally indistinguishable. The interferometers required for the generation and processing of time-bin and used in the experimental setup (Fig. 4.11) are realized using the coupled-fiber loop system described in Section 4.2.2.1. The procedure for entanglement generation is as follows: i) preparation of indistinguishable classical pulses to pump the nonlinear medium, here, PPLN; ii) generation of signal and idler photon pairs via SPDC in PPLN; iii) encoding of photon pair states and their subsequent processing for two-photon quantum interference measurements; and iv) detection of interferometric outcomes using state-of-the-art superconducting nanowire single-photon detectors in conjunction with high-speed time tagging modules.

The classical pump pulses were obtained from a tunable laser with a center wavelength of 1549.7 nm, a repetition rate of 10 MHz and a pulse width of~10 fs. The laser featured two outputs: the primary output was utilized as the pump, and the secondary output served as a trigger for an acousto-optic modulator (AOM). The AOM was connected in series with the laser for pulse picking, enabling tunability of the laser repetition rate. In this experiment, the repetition rate was tailored to match the length of the coupled fiber-loop system to allow for convenient quantum state processing, as well as to minimize crosstalk between the different temporal modes in the setup. The operation of the AOM was controlled by a cosine wave generated via an arbitrary function generator, which was amplified by an RF power amplifier at the required frequency for the desired repetition rate. The AOM was then attached to a 90-10 beam splitter, where the output of the 90% port was used for the experiment, while the 10% port was detected using a photodiode. The trigger from this photodiode was used for the time synchronization of all the active devices in the experiment.

The coupled fiber-loop system is described in Section 4.2.2.1. The main advantage of employing such a system lies in its ability to facilitate a controlled light walk which allows for the processing of quantum states. This is critical for lowering the losses of the scheme, a valuable benefit for realizing practical quantum photonic processing stages. A full description on the controlled light walk scheme is

described in Section 4.2.2.2. The system comprised two fiber-loops of different lengths, long (blue color) and short (brown color) loops of lengths of ~120 m and ~100 m, respectively. Therefore, photons in the long and short loops take 600 ns and 500ns, respectively, to complete a roundtrip. The two loops were coupled together with a dynamic optical switch (BATi). The light flow in and out of the loops were controlled by two additional dynamic optical switches, labeled as gates 1 and 2. The transmission and reflection ratios of all optical switches were tuned by an external applied voltage for them to either act as a full reflector or transmitter, or as a 50-50 beam splitter. We recall that reflection and transmission settings on the dynamical coupler cause the light to either transfer to the other loop or to stay in the residing loop, respectively. The signals controlling the optical switches were generated by function generators synchronized with the laser frequency and triggered by the 10% output of the AOM. For the generation of a classical pulse doublet, a single light pulse from the laser underwent two roundtrips with the optical switch set to operate as a 50-50 beam splitter. The pulse doublet exited the fiber-loop through gate 1, which was directed to a 90-10 beam coupler, where the output from the 10% port was used to monitor the output pulse, while that from the 90% port was employed to pump the source of entangled photons after amplification.

The classical pump doublet was injected into the entangled photon source after passing through a notch filter centered at 1549.7 nm. The source was a pair of PPLN waveguides: the first waveguide (PPLN1) served as an up-conversion module in the telecommunications C-band through SHG, and the second PPLN (PPLN2) behaved as a photon pair source due to SPDC. The SHG process in PPLN1 resulted in the generation of ~775 nm wavelength light which was used to excite PPLN2. The pump wavelength was mitigated by a 775 nm bandpass filter prior to the SPDC process. Here, owing to type-0 SPDC, broadband entangled signal and idler photon pairs were generated in the telecom band. The photons were filtered using a 1550 nm bandpass filter, which provided effective suppression of the SHG wavelength components. Note that both PPLN waveguides were optimized in terms of temperature to provide maximum nonlinear conversion efficiency in the classical (SHG) and quantum (SPDC) domains, confirmed via SHG power as well as single-photon detection measurements, respectively.

To enable the required encoding to the time-bin entangled states, a relative phase between the early and late temporal modes was applied using an electro-optic phase modulator to the classical pulse doublet. A reference signal which was configured as a step function ranging from 0 to 3.3 V imparted a phase difference from 0 to π rad onto the entangled state. This phase encoded quantum state was then directed back into the coupled-fiber loop system for processing, employing the controlled walk schemes outlined in Sections 4.3.2 and 4.3.3. The processed quantum state was then extracted through gate 2 for subsequent detection.

The detection part included a dense wavelength-division multiplexer (DWDM) featuring a channel bandwidth of 200 GHz. The DWDM separated the signal and idler photons according to their wavelengths through ITU channels H38.5 (1546.72 nm – 1549.32 nm) and H30.5 (1553.33 nm – 1552.52 nm), respectively. The photon states were detected by single-photon detectors backed with time-tagging electronics triggered by the AOM signal. It is important to note that the entanglement generation and processing setups were realized on an all-fiber platform using polarization-maintaining components and off-the-shelf fiber-optic telecom instrumentation.

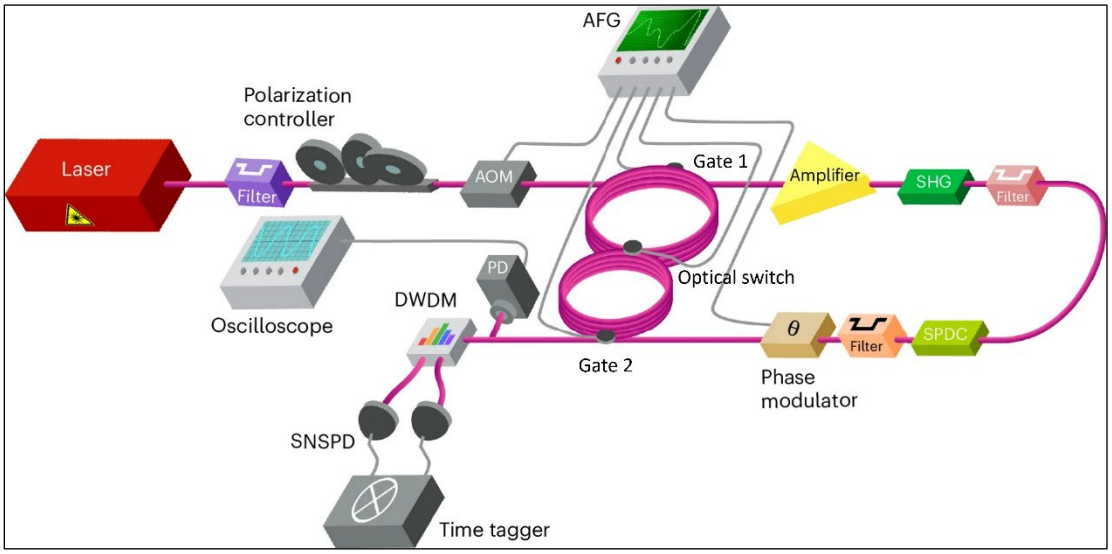

Fig. 4.11: **Experiment setup.** The repetition rate of the output from the fs laser is reduced to 181.81 kHz using an acousto-optic modulator (AOM). Such pulses are sent to the loop system to generate two classical pulses for state preparation. These are then propagated through the periodically poled lithium niobate (PPLN) crystals for the generation of a pair of correlated photons in two time bins, t_1 and t_2. The PPLN1 crystal generates second harmonic light that is used by the second PPLN2 crystal for spontaneous parametric down conversion (SPDC), from which correlated photon pairs are generated. The entangled state is then fed to the phase modulator for phase encoding. The phase encoded time-bin entangled photons are then allowed to interfere in the fiber-loop system. The interfered peaks at various phases are sent to a dense wavelength-division multiplexer (DWDM) to separate signal and idler photons. Such photons are detected by the state-of-art single photon detectors. **(31)**

4.3.2 Generation and processing of Two-dimensional time-bin entangled states

Preparation of classical pulses

The preparation of the classical pulses for the generation of time-bin entangled photons and the processing of the generated entangled state were done in the same coupled loop system. The repetition rate of the pump source was reduced to 181.81 kHz using the AOM to account for the beam propagation time through the long fiber loops. The pump pulse was then spectrally filtered to a bandwidth of $\Delta\tau = 0.208$ nm prior to its injection into the coupled fiber-loop system.

For its preparation, the classical double pulse was sent to the coupled fiber-loop system by opening gate 1, where it could be prepared through two different methods.

Method 1: As described in Sections 4.2.2 and 4.3.1, this method involved setting the optical switch at a constant 50:50 transmission-reflection (T-R) ratio. After two roundtrips, two classical pulses were extracted, while gates 1 and 2 remained closed throughout the process.

Method 2: This approach utilized a controlled quantum walk, incorporating Fourier ($\hat{F}$), Transmission ($\hat{T}$) and Reflection ($\hat{R}$) operations. When the initial light pulse entered the coupled fiber-loop system through gate 1, the optical switch was set at a 50:50 T-R ratio ($\hat{F}$), evenly splitting the pulse between the long and short loops. During the second roundtrip, the pulse in the short loop advanced by 100 ns relative to the pulse in the long loop, due to the inherent delay between the loops. By opening the optical switch ($\hat{R}$) and promptly closing it ($\hat{T}$), the pulse in the short loop was reflected into the long loop, while the pulse in the long loop continued its original propagation. The resulting pair of classical pulses in the long loop was then extracted through gate 1.

For both methods, the output state of the photon can be written as (200)

$$|\psi\rangle_P = \frac{1}{\sqrt{2}}(|1,0\rangle + |0,1\rangle) \tag{4.3.1}$$

The state $|1,0\rangle$ ($|0,1\rangle$) corresponds to the case where one photon is in the first (second) time bin. These classical double pulses were passed through an electro-optic phase modulator to encode phase information, $\phi \in (0, \pi)$. After phase encoding, the pulses were directed back into the coupled fiber-loop system for classical interference characterization, with the processed state subsequently detected by a photodetector.

To generate time-bin entangled state, instead of sending the classical doublet to phase modulator, the pulses were amplified, filtered, and then directed to the pair of PPLN waveguides.

Preparation of time-bin entangled state

A type-0 PPLN waveguide, where all the interacting photons have same polarization, was utilized to realize time-bin entanglement. The coherent superposition of a classical double pulse was directed through a pair of PPLN waveguides to generate the entangled state. The first PPLN waveguide (PPLN1) converted the pump wavelength to ~ 775 nm via second harmonic generation. The frequency doubled output was used to initiate a SPDC process in PPLN2. Photon pairs, i.e., signal and idler, were generated in the two temporal modes, corresponding to early and late time-bins, represented by t_1 and t_2. To eliminate the classical beams (pump and SHG light), suitable bandpass and notch filters were employed. The quantum state of the system can be represented by:

$$|\psi_0\rangle = \frac{1}{\sqrt{2}} \left(|t_1, t_1\rangle_{s,i} + e^{2i\phi}|t_2, t_2\rangle_{s,i}\right) \tag{4.3.2}$$

where ϕ is the relative phase encoded between time modes, t_1 and t_2.

One-dimensional discrete time quantum walk

Fig. 4.12 illustrates the uncontrolled and controlled schemes used in the experiment. Initially, the time-bin entangled state was injected into the coupled-fiber loop system through gate 2, as depicted in the experimental setup. The early and late time-bins were positioned at $x = -1$ and $x = 1$ in the synthetic photonic lattice, respectively.

In the uncontrolled scheme (Fig. 4.12 (a)), when the entangled state reached the optical switch, the operation $\hat{F}$ was applied to both the early time-bin, t_1, and late time-bin, t_2, for two roundtrips. After the first roundtrip, photons in the early time bin could be positioned either at $x = -2$ or $x = -1$, while photons in the late time-bin could be at either $x = 0$ or $x = 1$. In the following roundtrip, photons at positions $x = -1$ and $x = 0$ arrived at the optical switch simultaneously, resulting in quantum interference and distributing interference components between $x = -1$ and $x = 0$. The interfered component at $x = -1$, along with the side peaks at $x = -3$ and $x = 3$, was directed to the detection stage. The resulting single-photon histogram is demonstrated in Fig. 4.12 b). The middle peak, containing the coincidence events, was post-selected and analyzed to measure the quantum interference.

For the controlled scheme (Fig. 4.12 (c)), during the first roundtrip, the two coin operations, $\hat{T}$ and $\hat{R}$ governed the propagation of early time-bin, t_1, and late time-bin, t_2, at the optical switch. $\hat{T}$ directed t_1 to the long loop, while $\hat{R}$ directed t_2 to the short loop, positioning t_1 at $x = -1$ and t_2 at $x = 1$ in the synthetic photonic lattice. In the second roundtrip, the coin operator $\hat{F}$ acted on both t_1 and t_2. The impossibility to distinguish at which time the photons pass the optical switch led to quantum interference. The interfered components were distributed between the short loop at position $x = -1$ and the long loop at position $x = 1$. The interfered component in the short loop was then sent to the detection stage. The single-

photon histogram (Fig. 4.12 (d)) showed only one peak, indicating that all the photons contributed to quantum interference and that the coincidence events could be extracted without post-selection.

Subsequently, the signal and idler states were separated utilizing a DWDM from the evolved state and were detected by state-of-the-art single-photon detectors. The arrival times of the signal and idler photons were recorded by a time-tagging electronics (Hydraharp). The photon statistics were gathered for 15 minutes at each phase setting, $\phi \in (0, \pi)$ and the coincidence events were recorded for each phase value. The quantum interference fringes obtained in uncontrolled and controlled cases are shown in Fig. 4.12 c) and f), respectively.

We demonstrated that the uncontrolled scheme exhibited a significantly lower detection probability compared to the controlled scheme due to the distribution of photons across three time-bins. Consequently, the controlled scheme increased the coincidence counts from 21 to 77 per minute relative to the uncontrolled counterpart. The experimentally obtained data points were fitted using

$$CC_{d=2} = \frac{1+Vcos(2(\phi+b))}{c} \tag{4.3.3}$$

where V is the visibility accounting for the noise admixture, and a, b and c are constants. The visibilities of these fringes can also be computed using,

$$V = \frac{cc_{max}-cc_{min}}{cc_{max}+cc_{min}} \tag{4.3.4}$$

where cc_{max} and cc_{min} are maximum and minimum measured coincidences, respectively. The visibilities obtained for uncontrolled and controlled DTQW, estimated using the symmetric noise model (235), were found to be 97.82% and 96.83%, respectively. These values were well beyond the Bell inequality threshold value of 70.71% (203, 205), providing clear evidence of entanglement between the two time bins.

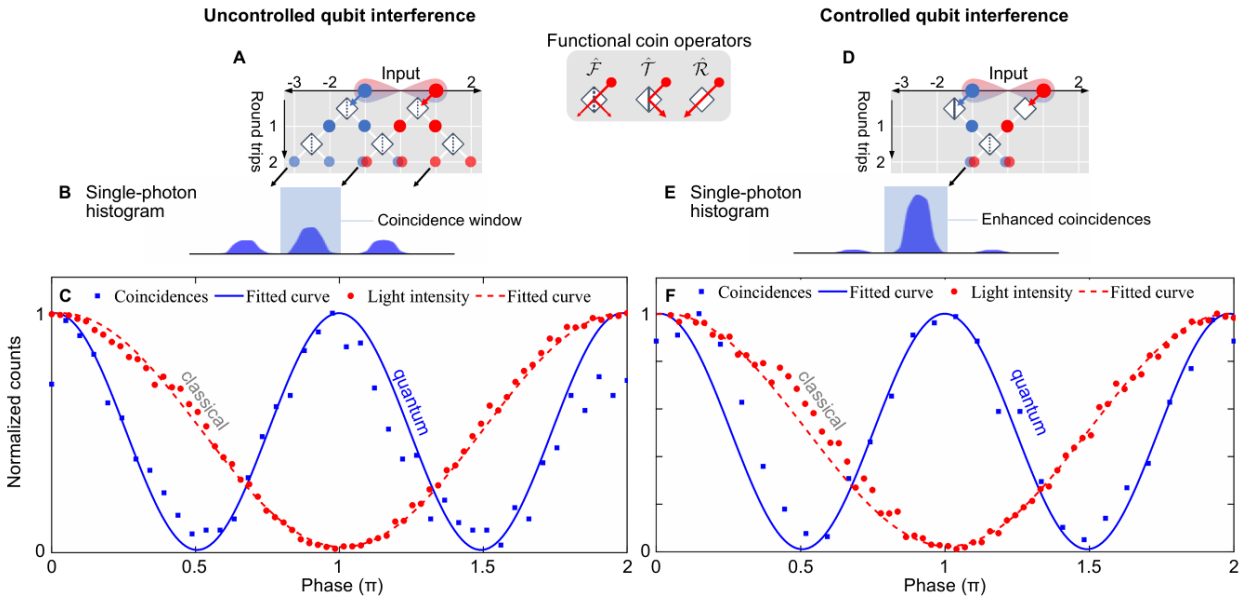

Fig. 4.12: **DTQW schemes for Two-dimensional time-bin entangled states** a), d), Spatial representations of two roundtrips of the DTQW in the coupled fiber-loop system under uncontrolled (a) and controlled (d) schemes. The legend in the center introduces the action of the three operators used in the experiment (Fourier (50:50), transmission and reflection). b), e), Single-photon histograms. The light-blue box in the single-photon histogram represents the interference coincidence window at zero relative time delay taken from the central interference bin. c), f), Normalized coincidence counts of entangled photons and classical light intensity (blue squares and red circles, respectively) as a function of the relative phase difference ($\boldsymbol{\theta}$) between the time bins. Experimental measurements are fitted with theoretical models (blue solid line for entangled qubits and dotted red line for classical light). From two-photon quantum interference measurements, raw visibility values of 97.82% and 96.83% were extracted for the uncontrolled (c) and controlled (d) schemes, respectively**. (31, 227)**

4.3.3 Generation and processing of Four-dimensional time-bin entangled states

After demonstrating the potential of the coupled fiber-loop system for generating and processing two-dimensional time-bin entangled states, the next challenge is to generate and process high-dimensional time-bin entangled states.

Preparation of classical pulses

Similar to the two-dimensional case, the first step is to generate four classical pulses that are in coherent superposition. For the preparation of four classical pulses, the initial seed pulse was sent to the coupled fiber-loop system through gate 1. The classical pulses could be prepared through two different methods.

Method 1: The optical switch was kept at a constant 50:50 T-R ratio. After four roundtrips, four classical pulses were extracted from the coupled fiber-loop system. To ensure uniform pulse amplitude, the T-R ratio of gate 1 (for the middle two pulses) was adjusted based on the amplitude of the pulses generated.

Method 2: In the second method, a controlled DTQW was employed. For the first two roundtrips, the optical switch was set to a 50:50 T-R ratio, generating four classical pulses—two in the long loop and two in the short loop. During the third roundtrip, the optical switch was set to $\hat{R}$, causing the pulses to continue in their respective loops, maintaining a 100 ns time difference between them. During the fourth roundtrip, the optical switch was opened ($\hat{T}$) to send the double pulse from the short loop to the long loop. The optical switch was then closed ($\hat{R}$) to allow the pulses to propagate within the long loop. Finally, the resulting four pulses in the long loop were extracted through gate 2.

Preparation of high-dimensional time-bin entangled state

Like the generation of two-dimensional time-bin entangled states, the four classical pulses in coherent superposition were directed through a pair of PPLN waveguides to create four-dimensional time-bin entangled states. The resultant quantum state can be represented by

$$|\psi_0\rangle = \frac{1}{2}\left(|t_1, t_1\rangle_{s,i} + e^{2i\phi}|t_2, t_2\rangle_{s,i} + e^{4i\phi}|t_3, t_3\rangle_{s,i} + e^{6i\phi}|t_4, t_4\rangle_{s,i}\right) \quad (4.3.5)$$

where ϕ is the relative phase encoded between different time modes.

One-dimensional discrete time quantum walk

To implement four-dimensional quantum interference measurements, we employed two controlled DTQW strategies, referred to as controlled scheme 1 and controlled scheme 2. Fig. 4.13 (a) and (b) illustrate the respective controlled schemes employed in the experiment.

Initially, the time-bin entangled state was injected into the coupled-fiber loop system through gate 2 (as shown in the experimental setup). The four time-bins, t_1, t_2, t_3 and t_4, were positioned at $x = -3, -1, 1$ and 3 in the synthetic photonic lattice, respectively.

Controlled scheme 1: In this scheme, only $\hat{F}$ and $\hat{R}$ were applied to various time bins during different roundtrips (Fig. 4.13 (a)). For the first two roundtrips, the optical switch was set to 50:50 ratio ($\hat{F}$), distributing photons in four time-bins at positions $x = -5, -4, -3, -2, -1, 0, 1, 2, 3,$ and 4. During the following roundtrip, the optical switch was set to full reflection ($\hat{R}$), positioning photons at $x = -6, -4, -3, -2, -1, 0, 1, 2, 3,$ and 5. However, the interfered components at each position were different due to the interference between different time-bins. In the final roundtrip, the optical switch was set at $\hat{F}$, resulting in a total of 14 time-bins, with interfered components of all four time-bins mixed at $x = -1$ and $x = 0$. The time-bins in the short loop were then extracted through gate 2 and directed to the detection stage, as shown in Fig. 4.13 (b). To measure coincidences between the signal and idler photons, the central mode of seven time-bins was post selected.

Controlled scheme 2: This controlled DTQW scheme, shown in Fig. 4.13 (c), used all three control operations. In the first roundtrip, the optical switch directed the first two time-bins (t_1 and t_2) into the long loop by applying $\hat{T}$, while the remaining two time-bins (t_3 and t_4) stayed in the short loop due to the application of $\hat{R}$. This positioned t_1 and t_2 at $x = -3$, and -1, respectively, while positioning t_3 and t_4 at $x = 0$ and 2. During the second roundtrip, the coupler was set to full reflection ($\hat{R}$), allowing the time-bins to propagate in their respective loops. During the final two roundtrips, $\hat{F}$ was applied to photons at all positions. This resulted in distributing the interfered components at positions $x = -3, -2, -1, 0, 1$ and 2, with interfered components at $x = -1$ and $x = 0$ containing the interference from all four time-bins. The components in the short loop were then extracted through gate 2 and sent to the detection stage. Finally, the central mode, containing the information, was post-selected from the three output modes.

The interference fringes obtained for both controlled schemes are shown in Fig. 4.13 (b and d). Controlled scheme 2 yielded 8.3 counts per minute, while controlled scheme 1 resulted in 4.5 counts per minute. This shows that the controlled scheme 2, increased the coincidence detection probability due to efficient mixing of photons, compared to controlled scheme 1.

We fitted the experimental data with the following equation:

$$CC_{d=4} = \frac{4+2V_{d=4}(3cos(2(\phi+b)+2cos(4(\phi+c)+\cos(6(\phi+d))}{e} \quad (4.3.6)$$

where $V_{d=4}$, $b, c, d,$ and e are fitting parameters. The controlled scheme 1 and 2 procedure yielded raw visibilities of 91.55% and 89.51%, respectively, both surpassing the threshold of 81.70% necessary to violate the Collins-Gisin-Linden-Massar-Popescu (CGLM) inequality (151, 205).

These results highlight a significant advantage of our system in generating and processing high-dimensional time-bin entangled states. By leveraging the programmability of the optical switch, we were able to manipulate and process entangled states, thus opening the door to investigating various quantum walk protocols, leading to more complex processing with promising applications in quantum technologies.

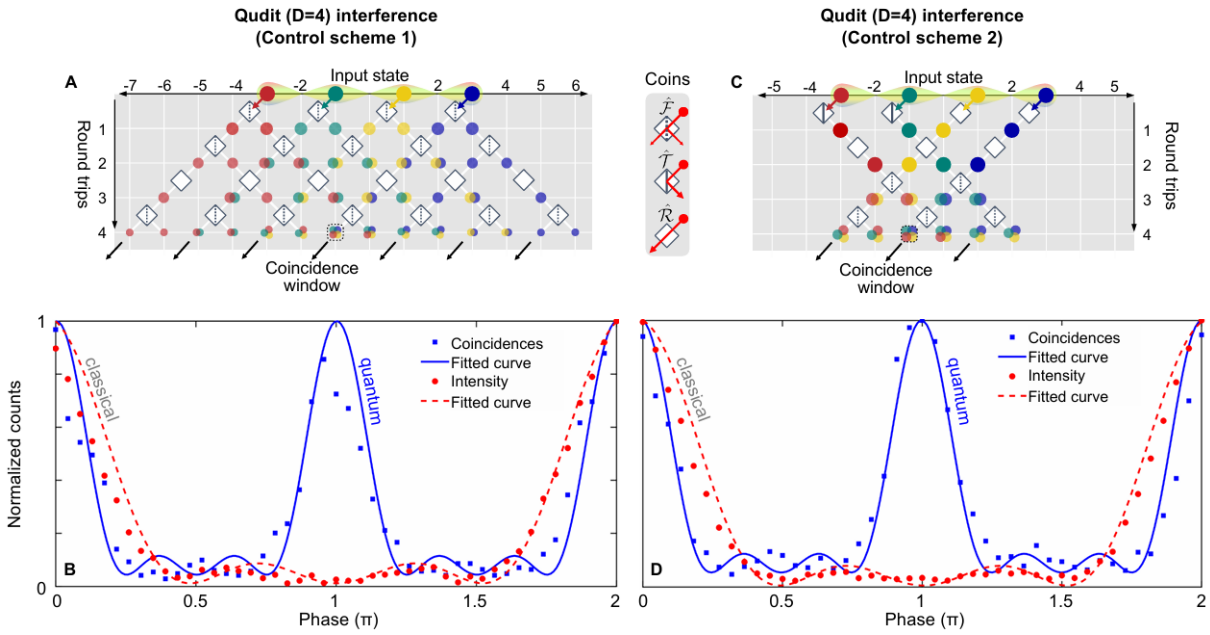

Fig. 4.13: **DTQW schemes for Four-dimensional time-bin entangled states** a) ,c), Spatial representations of four DTQW roundtrips: the coupled fiber-loop system under roundtrip-wise controlled scheme 1 (a) and roundtrip- and synthetic position-wise controlled scheme 2 (c). Coincidence counts are measured at the central time bin coincidence window of the fiber loop's interference output, and at zero photon time delay. b), d), Normalized coincidence counts of four-level entangled photons and classical light intensity (blue squares and red circles, respectively) as a function of the relative phase difference (θ) between the time bins. Experimental measurements are fitted with theoretical models (solid blue line for entangled qudits and dotted red line for classical light). From two-photon quantum interference measurements, raw visibility values of 91.55% and 89.61% were extracted for scheme 1 (b) and scheme 2 (d), respectively**. (31, 227)**

4.4 Conclusion

This chapter of the thesis focused on the experimental investigation of quantum interference by processing two and four-dimensional time-bin entangled states via quantum walk protocols. The main objective of this project was to demonstrate that quantum walk schemes in a synthetic photonic lattice with judiciously tailored coin operations can be used for generating high-dimensional quantum state and its (efficient) processing.

This objective was conceptualized and implemented through a controlled quantum walk within a synthetic photonic lattice in the temporal domain. The synthetic photonic lattice was realized through a coupled fiber-loop system, which served as the heart of the experiment. The experiment to investigate high-dimensional quantum interference consisted of four main steps: 1) generation of classical pulses, 2) generation of time-bin entangled states and phase encoding, 3) processing stage that involved various controlled quantum walks and finally, 4) the detection stage. After the processing of time-bin entangled state, the photon statistics of output signals were collected, and their respective visibilities were determined. Additionally, for the first time, a proof-of-concept experiment showcasing the potential of a synthetic photonic lattice in the temporal domain for quantum information processing was demonstrated through this study.

The experimental results presented in this chapter contribute to the development of photonic quantum technologies, as well as their real-world applications. The coupled fiber-loop system with controlled DTQW will provide a versatile platform for various quantum technologies, by enabling the implementation of POVMs. Apart from its application in quantum communication (16, 200), controlled quantum walk scheme will find a host of applications in quantum metrology (22, 23, 202), non-locality of quantum states (231), quantum state discrimination (236), quantum tomography (237), and coherent controls (238). For example, extending the presented controlled DTQW for two-level time-bin entangled state enables the construction of a POVM (Π_j) consisting of four positive operators that satisfy the condition $\sum_j \Pi_j = I$. In addition, the system could be tailored to obtain post-selection loop-hole free Bell violation as presented in (239) for two or higher dimensional time-bin entangled states. Furthermore, the results presented in this chapter will open new avenues, providing a compact and flexible tool, for studying a variety of different topological quantum walks, and for exploring rich quantum dynamics that have not yet been experimentally investigated.

5 Conclusion and Outlook

This thesis investigated the role of photon statistics in two key areas: the characterization of thresholdless nanolasers and the characterization of time-bin entangled states. Through second-order correlation measurements, we demonstrated the limitations of classical techniques in defining nanolaser threshold behavior and introduced a more precise method for assessing their emission properties. Similarly, by leveraging quantum walks in synthetic photonic lattices, we successfully generated and processed high-dimensional time-bin entangled states, enabling precise entanglement control via a programmable optical system.

These results contribute to both fundamental and applied research in photonics and quantum optics. The characterization of thresholdless nanolasers provides critical insights into the development of compact, energy-efficient laser sources for integrated photonic applications. Meanwhile, the generation and manipulation of time-bin entangled states offer a scalable approach to quantum information processing, with potential applications in secure communication, computation, and metrology.

A key future direction of this research is the integration of nanolasers into photonic integrated circuits (PICs) for quantum applications. By combining advanced photon statistics with innovative experimental platforms, this work lays the foundation for the realization of high-performance quantum and classical photonic systems, bridging the gap between nanophotonics and quantum optics. Therefore, future efforts could focus on overcoming current challenges in integrating nanolasers into PICs, optimizing their performance for quantum applications, and further exploring synthetic photonic lattices for quantum computing, metrology and communication systems. The continued development of these technologies will pave the way for more efficient, scalable quantum systems with a broad impact.

6 BIBLIOGRAPHY

Journal Publications

1. **Agnes George**, Andrew Bruhacs, Abdul Aadhi, William E Hayenga, Rachel Ostic, Erin Whitby, Michael Kues, Zhiming M Wang, Christian Reimer, Mercedeh Khajavikhan, Roberto Morandotti, "Time–Resolved Second–Order Coherence Characterization of Broadband Metallic Nanolasers," Laser and Photonics Reviews, vol. 15, pp. 2000593, October 2021.
2. Monika Monika, Farzam Nosrati, **Agnes George**, Riza Fazili, André Luiz Marques Muniz, Arstan Bisianov, Stefania Sciara, Mario Chemnitz, Rosario Lo Franco, Ulf Peschel, Roberto Morandotti, "Scaling Quantum Information Processing with TPLs," Optics & Photonics News, December 2024.
3. Monika Monika, Farzam Nosrati, **Agnes George**, Riza Fazili, André Luiz Marques Muniz, Arstan Bisianov, Stefania Sciara, Mario Chemnitz, Rosario Lo Franco, Ulf Peschel, Roberto Morandotti, "Generation and verification of high-dimensional entangled states via temporal photonic lattices," Nature Photonics, vol. 19, pp. 95-100, January 2025.
4. Nicola Montaut, **Agnes George**, Monika Monika, Farzam Nosrati, Hao Yu, Stefania Sciara, Benjamin Crockett, Ulf Peschel, Zhiming Wang, Rosario lo Franco, Mario Chemnitz, William J. Munro, David J. Moss, José Azaña, Roberto Morandotti, "Progress in integrated and fiber optics for time-bin based quantum information processing," Advanced Optical Technologies, Accepted.
5. **Agnes George**, Nicola Montaut, Kobra Mahdavipour, Farzam Nosrati, Stefania Sciara, Monika Monika, Mario Chemnitz, Ulf Peschel, Rosario Lo Franco, Roberto Morandotti, "Quantum-Enhanced Phase Estimation via Controlled-Discrete-time Quantum Walk in Synthetic Photonic Lattices," In preparation.

Conference contributions

1. Stefania Sciara, Hao Yu, Mario Chemnitz, Monika Monika, Farzam Nosrati, **Agnes George**, Nicola Montaut, Bennet Fischer, Benjamin Crockett, Robin Helsten, Benjamin Wetzel, Thorsten A. Goebel, Ria G. Krämer, Brent E. Little, Sai T. Chu, Stefan Nolte, Zhiming Wang, José Azaña, William J. Munro, David J. Moss, Ulf Peschel, Rosario Lo Franco, Roberto Morandotti, "Time-bin entangled photons for scalable quantum information processing," Advanced Photonics Congress, August 2024, Québec City, Canada.
2. **Agnes George**, Monika Monika, Farzam Nosrati, Riza Fazili, André Luiz Marques Muniz, Arstan Bisianov, Stefania Sciara, Mario Chemnitz, Nicola Montaut, Rosario Lo Franco, Ulf Peschel, Roberto

Morandotti, “Generation and Verification of High-Dimensional Entangled States in Synthetic Photonic Lattices,” Photonics North, May 2024, Vancouver, Canada.

3. Monika Monika, Farzam Nosrati, Riza Fazili, **Agnes George**, André Luiz Marques Muniz, Arstan Bisianov, Stefania Sciara, Mario Chemnitz, Rosario Lo Franco, Ulf Peschel, Roberto Morandotti, “Controllable and Scalable Quantum States in Fiber Loop Systems,” Quantum 2.0 2023, June 2023, Colorado, United States.
4. **Agnes George,** Andrew Bruhacs, Abdul Aadhi, Rachel Ostic, Erin Whitby, William E Hayenga, Zhiming M Wang, Michael Kues, Christian Reimer, Mercedeh Khajavikhan, Roberto Morandotti, “Temporal dynamics of second-order correlation function in nanolasers,” Integrated Photonics Research, Silicon and Nanophotonics, July 2021, Virtual presentation.
5. **Agnes George**, Abdul Aadhi, Andrew Bruhacs, Rachel Ostic, Erin Whitby, William E Hayenga, Zhiming M Wang, Michael Kues, Christian Reimer, Mercedeh Khajavikhan, Roberto Morandotti, “Time-resolved second-order correlation measurements nanolasers,” Photonics North, June 2021, Virtual presentation.
6. **Agnes George**, Abdul Aadhi, Andrew Bruhacs, Rachel Ostic, Erin Whitby, William E Hayenga, Zhiming M Wang, Michael Kues, Christian Reimer, Mercedeh Khajavikhan, Roberto Morandotti, “Time-resolved second-order correlation measurements of metallic coaxial nanolasers under pulsed optical excitation,” CLEO: QELS Fundamental Science, May 2021, Virtual presentation.

Reference list

1. G. R. Fowles, *Introduction to Modern Optics* (Courier Corporation, 1989).
2. M. Fox, *Quantum Optics: An Introduction* (Oxford University Press, 2006).
3. R. J. Glauber, Coherent and incoherent states of the radiation field. *Phys. Rev.* **131**, 2766 (1963).
4. R. J. Glauber, The quantum theory of optical coherence. *Phys. Rev.* **130**, 2529 (1963).
5. R. Loudon, *The Quantum Theory of Light* (OUP Oxford, 2000).
6. R. H. Brown, R. Q. Twiss, Correlation between photons in two coherent beams of light. *Nature* **177**, 27–29 (1956).
7. F. Diedrich, H. Walther, Nonclassical radiation of a single stored ion. *Phys. Rev. Lett.* **58**, 203–206 (1987).
8. R. E. Slusher, L. W. Hollberg, B. Yurke, J. C. Mertz, J. F. Valley, Observation of Squeezed States Generated by Four-Wave Mixing in an Optical Cavity. *Phys. Rev. Lett.* **55**, 2409–2412 (1985).

9. R. M. Shelby, M. D. Levenson, D. F. Walls, A. Aspect, G. J. Milburn, Generation of squeezed states of light with a fiber-optic ring interferometer. *Phys. Rev. A* **33**, 4008–4025 (1986).

10. L.-A. Wu, H. J. Kimble, J. L. Hall, H. Wu, Generation of Squeezed States by Parametric Down Conversion. *Phys. Rev. Lett.* **57**, 2520–2523 (1986).

11. S. Tanzilli, *et al.*, PPLN waveguide for quantum communication. *Eur. Phys. J. - At. Mol. Opt. Plasma Phys.* **18**, 155–160 (2002).

12. P. G. Kwiat, *et al.*, New High-Intensity Source of Polarization-Entangled Photon Pairs. *Phys. Rev. Lett.* **75**, 4337–4341 (1995).

13. A. Aspect, P. Grangier, G. Roger, Experimental realization of Einstein-Podolsky-Rosen-Bohm Gedankenexperiment: A new violation of Bell's inequalities. *Phys. Rev. Lett.* **49**, 91 (1982).

14. A. N. Boto, *et al.*, Quantum Interferometric Optical Lithography: Exploiting Entanglement to Beat the Diffraction Limit. *Phys. Rev. Lett.* **85**, 2733–2736 (2000).

15. R. W. Boyd, J. P. Dowling, Quantum lithography: status of the field. *Quantum Inf. Process.* **11**, 891–901 (2012).

16. J. Brendel, N. Gisin, W. Tittel, H. Zbinden, Pulsed Energy-Time Entangled Twin-Photon Source for Quantum Communication. *Phys. Rev. Lett.* **82**, 2594–2597 (1999).

17. N. Gisin, R. Thew, Quantum communication. *Nat. Photonics* **1**, 165–171 (2007).

18. A. K. Ekert, Quantum cryptography based on Bell's theorem. *Phys. Rev. Lett.* **67**, 661–663 (1991).

19. D. Bouwmeester, *et al.*, Experimental quantum teleportation. *Nature* **390**, 575–579 (1997).

20. J.-W. Pan, D. Bouwmeester, H. Weinfurter, A. Zeilinger, Experimental Entanglement Swapping: Entangling Photons That Never Interacted. *Phys. Rev. Lett.* **80**, 3891–3894 (1998).

21. J. P. Dowling, Quantum optical metrology – the lowdown on high-N00N states. *Contemp. Phys.* **49**, 125–143 (2008).

22. V. Giovannetti, S. Lloyd, L. Maccone, Quantum Metrology. *Phys. Rev. Lett.* **96**, 010401 (2006).

23. V. Giovannetti, S. Lloyd, L. Maccone, Advances in quantum metrology. *Nat. Photonics* **5**, 222–229 (2011).

24. J. C. Matthews, *et al.*, Towards practical quantum metrology with photon counting. *Npj Quantum Inf.* **2**, 1–7 (2016).

25. M. A. Nielsen, I. L. Chuang, *Quantum Computation and Quantum Information: 10th Anniversary Edition* (Cambridge University Press, 2010).

26. D. P. DiVincenzo, Quantum Computation. *Science* **270**, 255–261 (1995).

27. D. Aharonov, "QUANTUM COMPUTATION" in *Annual Reviews of Computational Physics VI*, (WORLD SCIENTIFIC, 1999), pp. 259–346.

28. A. Aspuru-Guzik, P. Walther, Photonic quantum simulators. *Nat. Phys.* **8**, 285–291 (2012).

29. S. Lloyd, Universal Quantum Simulators. *Science* **273**, 1073–1078 (1996).

30. A. George, *et al.*, Time-Resolved Second-Order Coherence Characterization of Broadband Metallic Nanolasers. *Laser Photonics Rev.* **15**, 2000593 (2021).

31. M. Monika, *et al.*, Quantum state processing through controllable synthetic temporal photonic lattices. *Nat. Photonics* **19**, 95-100 (2025).

32. Q. Gu, Y. Fainman, *Semiconductor Nanolasers* (Cambridge University Press, 2017).

33. C. Henry, Theory of the linewidth of semiconductor lasers. *IEEE J. Quantum Electron.* **18**, 259–264 (1982).

34. M. Khajavikhan, *et al.*, Thresholdless nanoscale coaxial lasers. *Nature* **482**, 204–207 (2012).

35. L. Yuan, Q. Lin, M. Xiao, S. Fan, Synthetic dimension in photonics. *Optica* **5**, 1396–1405 (2018).

36. M. Ehrhardt, S. Weidemann, L. J. Maczewsky, M. Heinrich, A. Szameit, A Perspective on Synthetic Dimensions in Photonics. *Laser Photonics Rev.* **17**, 2200518 (2023).

37. E. Wolf, L. Mandel', Coherence properties of optical fields. *Uspekhi Fiz. Nauk* **87**, 491–520 (1965).

38. B. E. Saleh, D. Stoler, M. C. Teich, Coherence and photon statistics for optical fields generated by Poisson random emissions. *Phys. Rev. A* **27**, 360 (1983).

39. B. Bai, *et al.*, Hanbury Brown-Twiss effect without two-photon interference in photon counting regime. *Sci. Rep.* **7**, 2145 (2017).

40. X. Ma, *et al.*, Enhanced Hanbury Brown and Twiss interferometry using parametric amplification. *EPJ Quantum Technol.* **7**, 1–9 (2020).

41. R. W. Boyd, A. L. Gaeta, E. Giese, "Nonlinear optics" in *Springer Handbook of Atomic, Molecular, and Optical Physics*, (Springer, 2008), pp. 1097–1110.

42. E. Timurdogan, C. V. Poulton, M. J. Byrd, M. R. Watts, Electric field-induced second-order nonlinear optical effects in silicon waveguides. *Nat. Photonics* **11**, 200–206 (2017).

43. S. Tanzilli, *et al.*, Highly efficient photon-pair source using periodically poled lithium niobate waveguide. *Electron. Lett.* **37**, 26–28 (2001).

44. PPLN Guide-Overview. *HC Photonics Corp - PPLN PPLT MgOPPLN PPMgOLN SHG SFG SPDC DFG MIR OPO Waveguide Ridge Waveguide Mix.* https://www.hcphotonics.com/ppln-guide-overview.

45. I. A. Ghambaryan, *et al.*, Periodically poled structures in lithium niobate crystals: growth and photoelectric properties. *J. Optoelectron. Adv. Mater.* **5**, 61–68 (2003).

46. How to Use PPLN • Covesion • MgO:PPLN crystal and waveguide. *Covesion*. https://covesion.com/en/resource/how-to-use-ppln/.

47. S. Castelletto, *et al.*, Comparison of photon counting and analog techniques for the measurement of photon pair generation in a PPLN waveguide. *JOSA B* **25**, 7–14 (2008).

48. R. H. Brown, Correlation between photons in two coherent beams of light.

49. R. H. Brown, The intensity interferometer; its application to astronomy. *London* (1974).

50. J.-W. Pan, *et al.*, Multiphoton entanglement and interferometry. *Rev. Mod. Phys.* **84**, 777–838 (2012).

51. F. Bouchard, *et al.*, Two-photon interference: the Hong–Ou–Mandel effect. *Rep. Prog. Phys.* **84**, 012402 (2020).

52. R. Ghosh, L. Mandel, Observation of nonclassical effects in the interference of two photons. *Phys. Rev. Lett.* **59**, 1903 (1987).

53. C. K. Hong, Z. Y. Ou, L. Mandel, Measurement of subpicosecond time intervals between two photons by interference. *Phys. Rev. Lett.* **59**, 2044–2046 (1987).

54. L. Sansoni, *et al.*, Two-Particle Bosonic-Fermionic Quantum Walk via Integrated Photonics. *Phys. Rev. Lett.* **108**, 010502 (2012).

55. A. Nomerotski, M. Keach, P. Stankus, P. Svihra, S. Vintskevich, Counting of Hong-Ou-Mandel Bunched Optical Photons Using a Fast Pixel Camera. *Sensors* **20**, 3475 (2020).

56. Y. Aharonov, L. Davidovich, N. Zagury, Quantum random walks. *Phys. Rev. A* **48**, 1687–1690 (1993).

57. S. E. Venegas-Andraca, Quantum walks: a comprehensive review. *Quantum Inf. Process.* **11**, 1015–1106 (2012).

58. A. M. Childs, Universal Computation by Quantum Walk. *Phys. Rev. Lett.* **102**, 180501 (2009).

59. N. B. Lovett, S. Cooper, M. Everitt, M. Trevers, V. Kendon, Universal quantum computation using the discrete-time quantum walk. *Phys. Rev. A* **81**, 042330 (2010).

60. M. S. Underwood, D. L. Feder, Universal quantum computation by discontinuous quantum walk. *Phys. Rev. A* **82**, 042304 (2010).

61. T. Kitagawa, M. S. Rudner, E. Berg, E. Demler, Exploring topological phases with quantum walks. *Phys. Rev. A* **82**, 033429 (2010).

62. N. Shenvi, J. Kempe, K. B. Whaley, Quantum random-walk search algorithm. *Phys. Rev. A* **67**, 052307 (2003).

63. A. Schreiber, *Quantum Walks in Time* (FAU University Press, 2014).

64. K. Kadian, S. Garhwal, A. Kumar, Quantum walk and its application domains: A systematic review. *Comput. Sci. Rev.* **41**, 100419 (2021).

65. T.-L. Feng, Y.-S. Zhang, G.-M. Zhao, S. Liu, G.-C. Guo, Quantum Random Walks of Waves. [Preprint] (2010). http://arxiv.org/abs/1010.5295.

66. L. K. Grover, A fast quantum mechanical algorithm for database search in *Proceedings of the Twenty-Eighth Annual ACM Symposium on Theory of Computing - STOC '96*, (ACM Press, 1996), pp. 212–219.

67. S. S. Panda, P. A. A. Yasir, C. M. Chandrashekar, Quantum direct communication protocol using recurrence in k-cycle quantum walks. *Phys. Rev. A* **107**, 022611 (2023).

68. F. Wang, B. Cheng, Z.-W. Cui, M.-H. Yung, Quantum Computing by Quantum Walk on Quantum Slide. [Preprint] (2023). http://arxiv.org/abs/2211.08659.

69. M. Annabestani, M. Hassani, D. Tamascelli, M. G. A. Paris, Multiparameter quantum metrology with discrete-time quantum walks. *Phys. Rev. A* **105**, 062411 (2022).

70. A. Schreiber, *et al.*, A 2D Quantum Walk Simulation of Two-Particle Dynamics. *Science* **336**, 55–58 (2012).

71. A. Nayak, A. Vishwanath, Quantum Walk on the Line. [Preprint] (2000). http://arxiv.org/abs/quant-ph/0010117.

72. A. Ambainis, E. Bach, A. Nayak, A. Vishwanath, J. Watrous, One-dimensional quantum walks in *Proceedings of the Thirty-Third Annual ACM Symposium on Theory of Computing*, (ACM, 2001), pp. 37–49.

73. Y. Shikano, K. Chisaki, E. Segawa, N. Konno, Emergence of randomness and arrow of time in quantum walks. *Phys. Rev. A* **81**, 062129 (2010).

74. P. Kurzyński, A. Wójcik, Discrete-time quantum walk approach to state transfer. *Phys. Rev. A* **83**, 062315 (2011).

75. J. B. Stang, A. T. Rezakhani, B. C. Sanders, Correlation effects in a discrete quantum random walk. *J. Phys. Math. Theor.* **42**, 175304 (2009).

76. C. M. Chandrashekar, S. K. Goyal, S. Banerjee, Entanglement generation in spatially separated systems using quantum walk. *J. Quantum Inf. Sci.* **02**, 15–22 (2012).

77. B. Allés, S. Gündüç, Y. Gündüç, Maximal entanglement from quantum random walks. *Quantum Inf. Process.* **11**, 211–227 (2012).

78. R.-M. Ma, R. F. Oulton, Applications of nanolasers. *Nat. Nanotechnol.* **14**, 12–22 (2019).

79. S. Bozhevolnyi, *Plasmonic Nanoguides and Circuits* (Pan Stanford Publishing, 2009).

80. G. E. Moore, Cramming More Components onto Integrated Circuits. *Proc. IEEE* **86** (1998).

81. M. Smit, J. van der Tol, M. Hill, Moore's law in photonics. *Laser Photonics Rev.* **6**, 1–13 (2012).

82. E. M. Purcell, "Spontaneous Emission Probabilities at Radio Frequencies" in *Confined Electrons and Photons: New Physics and Applications*, NATO ASI Series., E. Burstein, C. Weisbuch, Eds. (Springer US, 1995), pp. 839–839.

83. H. Yokoyama, S. D. Brorson, Rate equation analysis of microcavity lasers. *J. Appl. Phys.* **66**, 4801–4805 (1989).

84. H. Yokoyama, *et al.*, Enhanced spontaneous emission from GaAs quantum wells in monolithic microcavities. *Appl. Phys. Lett.* **57**, 2814–2816 (1990).

85. Y. Yamamoto, S. Machida, G. Björk, Microcavity semiconductor laser with enhanced spontaneous emission. *Phys. Rev. A* **44**, 657–668 (1991).

86. J.-M. Gerard, B. Gayral, Strong Purcell Effect for InAs Quantum Boxes in Three-Dimensional Solid-State Microcavities. *J. Light. Technol.* **17**, 2089 (1999).

87. E. K. Lau, A. Lakhani, R. S. Tucker, M. C. Wu, Enhanced modulation bandwidth of nanocavity light emitting devices. *Opt. Express* **17**, 7790–7799 (2009).

88. C.-Y. A. Ni, S. L. Chuang, Theory of high-speed nanolasers and nanoLEDs. *Opt. Express* **20**, 16450–16470 (2012).

89. T. Suhr, N. Gregersen, K. Yvind, J. Mørk, Modulation response of nanoLEDs and nanolasers exploiting Purcell enhanced spontaneous emission. *Opt. Express* **18**, 11230–11241 (2010).

90. B. Ellis, *et al.*, Ultralow-threshold electrically pumped quantum-dot photonic-crystal nanocavity laser. *Nat. Photonics* **5**, 297–300 (2011).

91. P. Bhattacharya, B. Xiao, A. Das, S. Bhowmick, J. Heo, Solid state electrically injected exciton-polariton laser. *Phys. Rev. Lett.* **110**, 206403 (2013).

92. S. Noda, Seeking the ultimate nanolaser. *Science* **314**, 260–261 (2006).

93. R. N. Hall, G. E. Fenner, J. D. Kingsley, T. J. Soltys, R. O. Carlson, Coherent light emission from GaAs junctions. *Phys. Rev. Lett.* **9**, 366 (1962).

94. H. Soda, K. Iga, C. Kitahara, Y. Suematsu, GaInAsP/InP surface emitting injection lasers. *Jpn. J. Appl. Phys.* **18**, 2329 (1979).

95. F. Albert, *et al.*, Whispering gallery mode lasing in electrically driven quantum dot micropillars. *Appl. Phys. Lett.* **97** (2010).

96. S. L. McCall, A. F. J. Levi, R. E. Slusher, S. J. Pearton, R. A. Logan, Whispering-gallery mode microdisk lasers. *Appl. Phys. Lett.* **60**, 289–291 (1992).

97. V. Sandoghdar, *et al.*, Very low threshold whispering-gallery-mode microsphere laser. *Phys. Rev. A* **54**, R1777 (1996).

98. O. Painter, *et al.*, Two-dimensional photonic band-gap defect mode laser. *Science* **284**, 1819–1821 (1999).

99. D. J. Gargas, *et al.*, Whispering gallery mode lasing from zinc oxide hexagonal nanodisks. *ACS Nano* **4**, 3270–3276 (2010).

100. F. Albert, *et al.*, Directional whispering gallery mode emission from Limaçon-shaped electrically pumped quantum dot micropillar lasers. *Appl. Phys. Lett.* **101** (2012).

101. M. T. Hill, M. C. Gather, Advances in small lasers. *Nat. Photonics* **8**, 908–918 (2014).

102. H. Hodaei, *et al.*, Enhanced sensitivity at higher-order exceptional points. *Nature* **548**, 187–191 (2017).

103. J. B. Khurgin, M. A. Noginov, How Do the Purcell Factor, the *Q* -Factor, and the Beta Factor Affect the Laser Threshold? *Laser Photonics Rev.* **15**, 2000250 (2021).

104. M. L. Brongersma, V. M. Shalaev, The Case for Plasmonics. *Science* **328**, 440–441 (2010).

105. K.-Y. Jeong, *et al.*, Recent Progress in Nanolaser Technology. *Adv. Mater.* **32**, 2001996 (2020).

106. B. Qi, H. Chen, L. Ge, P. Berini, R. Ma, Parity–Time Symmetry Synthetic Lasers: Physics and Devices. *Adv. Opt. Mater.* **7**, 1900694 (2019).

107. B. Bahari, *et al.*, Nonreciprocal lasing in topological cavities of arbitrary geometries. *Science* **358**, 636–640 (2017).

108. A. Kodigala, *et al.*, Lasing action from photonic bound states in continuum. *Nature* **541**, 196–199 (2017).

109. E. S. Koteles, Optical Characterization of Quantum Well Structures. *MRS Online Proc. Libr. OPL* **326** (1993).

110. N. Holonyak, R. Kolbas, R. Dupuis, P. Dapkus, Quantum-well heterostructure lasers. *IEEE J. Quantum Electron.* **16**, 170–186 (1980).

111. Y. Arakawa, A. Yariv, Quantum well lasers--Gain, spectra, dynamics. *IEEE J. Quantum Electron.* **22**, 1887–1899 (1986).

112. S. W. Corzine, R.-H. Yan, L. A. Coldren, Optical gain in III-V bulk and quantum well semiconductors. *Quantum Well Lasers* **23** (1993).

113. C. Kittel, *Introduction to solid state physics* (John Wiley & sons, inc, 2005).

114. S. A. Maier, *Plasmonics: fundamentals and applications* (Springer, 2007).

115. M. P. Nezhad, *et al.*, Room-temperature subwavelength metallo-dielectric lasers. *Nat. Photonics* **4**, 395–399 (2010).

116. E. M. Purcell, Spontaneous emission probabilities at radio frequencies. *Phys. Rev.* **69**, 681 (1946).

117. K. H. Drexhage, IV Interaction of Light with Monomolecular Dye Layers. *Progess Opt.* **12**, 163,192a,193-192,192a,232 (1974).

118. J. S. Smalley, Q. Gu, Y. Fainman, Temperature dependence of the spontaneous emission factor in subwavelength semiconductor lasers. *IEEE J. Quantum Electron.* **50**, 175–185 (2014).

119. E. M. Purcell, H. C. Torrey, R. V. Pound, Resonance absorption by nuclear magnetic moments in a solid. *Phys. Rev.* **69**, 37 (1946).

120. K. J. Vahala, Optical microcavities. *Nature* **424**, 839–846 (2003).

121. H. Yokoyama, Physics and device applications of optical microcavities. *Science* **256**, 66–70 (1992).

122. D. K. Cheng, *Field and wave electromagnetics* (Pearson Education India, 1989).

123. W. Hayenga, Fundamental Properties of Metallic Nanolasers. (2019).

124. S.-W. Chang, S. L. Chuang, Fundamental formulation for plasmonic nanolasers. *IEEE J. Quantum Electron.* **45**, 1014–1023 (2009).

125. M. Lorke, T. Suhr, N. Gregersen, J. Mørk, Theory of nanolaser devices: Rate equation analysis versus microscopic theory. *Phys. Rev. B* **87**, 205310 (2013).

126. S. H. Pan, Q. Gu, A. E. Amili, F. Vallini, Y. Fainman, Dynamic hysteresis in a coherent high-β nanolaser. *Optica* **3**, 1260–1265 (2016).

127. N. Hempler, *et al.*, Pulsed pumping of semiconductor disk lasers. *Opt. Express* **15**, 3247–3256 (2007).

128. Y. Wang, *et al.*, Photoluminescence Study of the Interface Fluctuation Effect for InGaAs/InAlAs/InP Single Quantum Well with Different Thickness. *Nanoscale Res. Lett.* **12**, 229 (2017).

129. J.-Y. Duboz, P. Bois, E. Rosencher, "Intersubband Transitions in Quantum Wells" in *Confined Electrons and Photons: New Physics and Applications*, NATO ASI Series., E. Burstein, C. Weisbuch, Eds. (Springer US, 1995), pp. 249–268.

130. L. M. Pedrotti, M. Sokol, P. R. Rice, Linewidth of four-level microcavity lasers. *Phys. Rev. - At. Mol. Opt. Phys.* **59**, 2295–2301 (1999).

131. S. M. Ulrich, *et al.*, Photon statistics of semiconductor microcavity lasers. *Phys. Rev. Lett.* **98**, 043906 (2007).

132. T. Wang, *et al.*, Superthermal-light emission and nontrivial photon statistics in small lasers. *Phys. Rev. A* **101**, 063835 (2020).

133. A. Lebreton, *et al.*, Unequivocal Differentiation of Coherent and Chaotic Light through Interferometric Photon Correlation Measurements. *APS* **110** (2013).

134. W. E. Hayenga, *et al.*, Second-order coherence properties of metallic nanolasers. *Optica* **3**, 1187 (2016).

135. S. Kreinberg, *et al.*, Thresholdless Transition to Coherent Emission at Telecom Wavelengths from Coaxial Nanolasers with Excitation Power Dependent β-Factors. *Laser Photonics Rev.* **14** (2020).

136. T. Wang, G. P. Puccioni, G. L. Lippi, Dynamical buildup of lasing in mesoscale devices. *Sci. Rep.* **5**, 15858 (2015).

137. M. Aßmann, *et al.*, Ultrafast tracking of second-order photon correlations in the emission of quantum-dot microresonator lasers. *Phys. Rev. B - Condens. Matter Mater. Phys.* **81**, 165314 (2010).

138. G. Moody, *et al.*, Delayed formation of coherence in the emission dynamics of high-Q nanolasers. *Optica* **5** (2018).

139. K. A. Serrels, *et al.*, Solid immersion lens applications for nanophotonic devices. *J. Nanophotonics* **2**, 021854 (2008).

140. R. Horodecki, P. Horodecki, M. Horodecki, K. Horodecki, Quantum entanglement. *Rev. Mod. Phys.* **81**, 865–942 (2009).

141. D. Bruß, Characterizing entanglement. *J. Math. Phys.* **43**, 4237–4251 (2002).

142. P. Walther, *et al.*, Experimental one-way quantum computing. *Nature* **434**, 169–176 (2005).

143. S. Zhou, M. Zhang, J. Preskill, L. Jiang, Achieving the Heisenberg limit in quantum metrology using quantum error correction. *Nat. Commun.* **9**, 78 (2018).

144. N. Brunner, D. Cavalcanti, S. Pironio, V. Scarani, S. Wehner, Bell nonlocality. *Rev. Mod. Phys.* **86**, 419–478 (2014).

145. G. Adesso, T. R. Bromley, M. Cianciaruso, Measures and applications of quantum correlations. *J. Phys. Math. Theor.* **49**, 473001 (2016).

146. M. Erhard, M. Krenn, A. Zeilinger, Advances in high-dimensional quantum entanglement. *Nat. Rev. Phys.* **2**, 365–381 (2020).

147. C. Senko, *et al.*, Realization of a Quantum Integer-Spin Chain with Controllable Interactions. *Phys. Rev. X* **5**, 021026 (2015).

148. S. P. Qudit, Emulation of a Quantum Spin with. *Astron Astrophys* **496**, 1 (2009).

149. S. Choi, *et al.*, Observation of discrete time-crystalline order in a disordered dipolar many-body system. *Nature* **543**, 221–225 (2017).

150. B. Yan, *et al.*, Observation of dipolar spin-exchange interactions with lattice-confined polar molecules. *Nature* **501**, 521–525 (2013).

151. M. Kues, *et al.*, On-chip generation of high-dimensional entangled quantum states and their coherent control. *Nature* **546**, 622–626 (2017).

152. S. Pirandola, B. R. Bardhan, T. Gehring, C. Weedbrook, S. Lloyd, Advances in photonic quantum sensing. *Nat. Photonics* **12**, 724–733 (2018).

153. F. Flamini, N. Spagnolo, F. Sciarrino, Photonic quantum information processing: a review. *Rep. Prog. Phys.* **82**, 016001 (2018).

154. S. Slussarenko, G. J. Pryde, Photonic quantum information processing: A concise review. *Appl. Phys. Rev.* **6**, 041303 (2019).

155. A. Cabello, Á. Feito, A. Lamas-Linares, Bell's inequalities with realistic noise for polarization-entangled photons. *Phys. Rev. A* **72**, 052112 (2005).

156. A. Mair, A. Vaziri, G. Weihs, A. Zeilinger, Entanglement of the orbital angular momentum states of photons. *Nature* **412**, 313–316 (2001).

157. L. Olislager, *et al.*, Frequency-bin entangled photons. *Phys. Rev. A* **82**, 013804 (2010).

158. H. Takesue, K. Inoue, Generation of 1.5-um band time-bin entanglement using spontaneous fiber four-wave mixing and planar lightwave circuit interferometers. *Phys. Rev. A* **72**, 041804 (2005).

159. H. Cable, J. P. Dowling, Efficient Generation of Large Number-Path Entanglement Using Only Linear Optics and Feed-Forward. *Phys. Rev. Lett.* **99**, 163604 (2007).

160. P. Kok, H. Lee, J. P. Dowling, Creation of large-photon-number path entanglement conditioned on photodetection. *Phys. Rev. A* **65**, 052104 (2002).

161. H. Takesue, Long-distance distribution of time-bin entanglement generated in a cooled fiber. *Opt. Express* **14**, 3453–3460 (2006).

162. J.-H. Kim, J.-W. Chae, Y.-C. Jeong, Y.-H. Kim, Quantum communication with time-bin entanglement over a wavelength-multiplexed fiber network. *APL Photonics* **7**, 016106 (2022).

163. J. D. Franson, Bell inequality for position and time. *Phys. Rev. Lett.* **62**, 2205–2208 (1989).

164. W. Tittel, J. Brendel, H. Zbinden, N. Gisin, Violation of Bell Inequalities by Photons More Than 10 km Apart. *Phys. Rev. Lett.* **81**, 3563–3566 (1998).

165. M. Hunault, H. Takesue, O. Tadanaga, Y. Nishida, M. Asobe, Generation of time-bin entangled photon pairs by cascaded second-order nonlinearity in a single periodically poled $LiNbO_3$ waveguide. *Opt. Lett.* **35**, 1239–1241 (2010).

166. Y. Huang, *et al.*, A Sixteen-user Time-bin Entangled Quantum Communication Network With Fully Connected Topology. *Laser Photonics Rev.* **19**, 2301026 (2025).

167. C. Reimer, *et al.*, Generation of multiphoton entangled quantum states by means of integrated frequency combs. *Science* **351**, 1176–1180 (2016).

168. T. Ono, Y. Tsujimoto, K. Wakui, M. Fujiwara, Quantum interference of pulsed time-bin entanglement generated from silicon ring resonator. *Sci. Rep.* **14**, 1051 (2024).

169. T. Huber, *et al.*, Coherence and degree of time-bin entanglement from quantum dots. *Phys. Rev. B* **93**, 201301 (2016).

170. H. Jayakumar, *et al.*, Time-bin entangled photons from a quantum dot. *Nat. Commun.* **5**, 4251 (2014).

171. L. Ginés, *et al.*, Time-bin entangled photon pairs from quantum dots embedded in a self-aligned cavity. *Opt. Express* **29**, 4174–4180 (2021).

172. J. P. Lee, *et al.*, A quantum dot as a source of time-bin entangled multi-photon states. *Quantum Sci. Technol.* **4**, 025011 (2019).

173. M. A. M. Versteegh, *et al.*, Single pairs of time-bin-entangled photons. *Phys. Rev. A* **92**, 033802 (2015).

174. P. Aumann, *et al.*, Demonstration and modeling of time-bin entangled photons from a quantum dot in a nanowire. *AIP Adv.* **12**, 055115 (2022).

175. T. Ward, M. Keller, Generation of time-bin-encoded photons in an ion-cavity system. *New J. Phys.* **24**, 123028 (2022).

176. S. Saha, *et al.*, High-fidelity remote entanglement of trapped atoms mediated by time-bin photons. [Preprint] (2024). http://arxiv.org/abs/2406.01761.

177. Z. Xie, Y. Liu, X. Mo, T. Li, Z. Li, Quantum entanglement creation for distant quantum memories via time-bin multiplexing. *Phys. Rev. A* **104**, 062409 (2021).

178. X.-H. Li, S. Ghose, Hyperentanglement concentration for time-bin and polarization hyperentangled photons. *Phys. Rev. A* **91**, 062302 (2015).

179. A. Tchebotareva, *et al.*, Entanglement between a Diamond Spin Qubit and a Photonic Time-Bin Qubit at Telecom Wavelength. *Phys. Rev. Lett.* **123**, 063601 (2019).

180. P.-F. Sun, *et al.*, Deterministic Time-Bin Entanglement between a Single Photon and an Atomic Ensemble. *Phys. Rev. Lett.* **128**, 060502 (2022).

181. P. Farrera, G. Heinze, H. de Riedmatten, Entanglement between a Photonic Time-Bin Qubit and a Collective Atomic Spin Excitation. *Phys. Rev. Lett.* **120**, 100501 (2018).

182. T.-H. Yang, *et al.*, Time-bin entanglement built in room-temperature quantum memory. *Phys. Rev. A* **103**, 062403 (2021).

183. N. J. Cerf, M. Bourennane, A. Karlsson, N. Gisin, Security of Quantum Key Distribution Using d -Level Systems. *Phys. Rev. Lett.* **88**, 127902 (2002).

184. G. M. Nikolopoulos, K. S. Ranade, G. Alber, Error tolerance of two-basis quantum-key-distribution protocols using qudits and two-way classical communication. *Phys. Rev. A* **73**, 032325 (2006).

185. T. Brougham, C. F. Wildfeuer, S. M. Barnett, D. J. Gauthier, The information of high-dimensional time-bin encoded photons. *Eur. Phys. J. D* **70**, 214 (2016).

186. F. Steinlechner, *et al.*, Distribution of high-dimensional entanglement via an intra-city free-space link. *Nat. Commun.* **8**, 1–7 (2017).

187. A. Delteil, N-qubit universal quantum logic with a photonic qudit and O(N) linear optics elements. *APL Quantum* **1**, 046101 (2024).

188. X. Liu, N. Bharos, L. Markovich, J. Borregaard, Error correlations in photonic qudit-mediated entanglement generation. *Phys. Rev. Res.* **6**, 023075 (2024).

189. J. Kim, *et al.*, Fully controllable time-bin entangled states distributed over 100-km single-mode fibers. *EPJ Quantum Technol.* **11**, 1–15 (2024).

190. I. Vagniluca, *et al.*, Efficient Time-Bin Encoding for Practical High-Dimensional Quantum Key Distribution. *Phys. Rev. Appl.* **14**, 014051 (2020).

191. F. Bouchard, *et al.*, Programmable Photonic Quantum Circuits with Ultrafast Time-Bin Encoding. *Phys. Rev. Lett.* **133**, 090601 (2024).

192. T. Ikuta, *et al.*, Scalable implementation of (d + 1) mutually unbiased bases for d -dimensional quantum key distribution. *Phys. Rev. Res.* **4**, L042007 (2022).

193. A. Martin, *et al.*, Quantifying Photonic High-Dimensional Entanglement. *Phys. Rev. Lett.* **118**, 110501 (2017).

194. A. Regensburger, *et al.*, Photon Propagation in a Discrete Fiber Network: An Interplay of Coherence and Losses. *Phys. Rev. Lett.* **107**, 233902 (2011).

195. A. Regensburger, *et al.*, Parity–time synthetic photonic lattices. *Nature* **488**, 167–171 (2012).

196. M. Wimmer, M.-A. Miri, D. Christodoulides, U. Peschel, Observation of Bloch oscillations in complex PT-symmetric photonic lattices. *Sci. Rep.* **5**, 17760 (2015).

197. M. Wimmer, M. Monika, I. Carusotto, U. Peschel, H. M. Price, Superfluidity of light and its breakdown in optical mesh lattices. *Phys. Rev. Lett.* **127**, 163901 (2021).

198. H. de Riedmatten, *et al.*, Long-distance entanglement swapping with photons from separated sources. *Phys. Rev. A* **71**, 050302 (2005).

199. R. Valivarthi, *et al.*, Teleportation Systems Toward a Quantum Internet. *PRX Quantum* **1**, 020317 (2020).

200. I. Marcikic, *et al.*, Time-bin entangled qubits for quantum communication created by femtosecond pulses. *Phys. Rev. A* **66**, 062308 (2002).

201. S. N. Sahoo, S. Chakraborti, A. K. Pati, U. Sinha, Quantum State Interferography. *Phys. Rev. Lett.* **125**, 123601 (2020).

202. E. Polino, M. Valeri, N. Spagnolo, F. Sciarrino, Photonic quantum metrology. *AVS Quantum Sci.* **2**, 024703 (2020).

203. J. S. Bell, On the Einstein Podolsky Rosen paradox. *Phys. Phys. Fiz.* **1**, 195–200 (1964).

204. J. S. BELL, On the Problem of Hidden Variables in Quantum Mechanics. *Rev. Mod. Phys.* **38**, 447–452 (1966).

205. D. Collins, N. Gisin, N. Linden, S. Massar, S. Popescu, Bell Inequalities for Arbitrarily High-Dimensional Systems. *Phys. Rev. Lett.* **88**, 040404 (2002).

206. X. Guo, Y. Mei, S. Du, Testing the Bell inequality on frequency-bin entangled photon pairs using time-resolved detection. *Optica* **4**, 388–392 (2017).

207. K.-C. Chang, *et al.*, 648 Hilbert-space dimensionality in a biphoton frequency comb: entanglement of formation and Schmidt mode decomposition. *Npj Quantum Inf.* **7**, 48 (2021).

208. H. B. Perets, *et al.*, Realization of Quantum Walks with Negligible Decoherence in Waveguide Lattices. *Phys. Rev. Lett.* **100**, 170506 (2008).

209. M. A. Broome, *et al.*, Discrete Single-Photon Quantum Walks with Tunable Decoherence. *Phys. Rev. Lett.* **104**, 153602 (2010).

210. Y. Lahini, *et al.*, Anderson Localization and Nonlinearity in One-Dimensional Disordered Photonic Lattices. *Phys. Rev. Lett.* **100**, 013906 (2008).

211. M. Kawachi, Silica waveguides on silicon and their application to integrated-optic components. *Opt. Quantum Electron.* **22**, 391–416 (1990).

212. Y. Liu, X. Zhang, Metamaterials: a new frontier of science and technology. *Chem. Soc. Rev.* **40**, 2494–2507 (2011).

213. C. M. Soukoulis, M. Wegener, Past achievements and future challenges in the development of three-dimensional photonic metamaterials. *Nat. Photonics* **5**, 523–530 (2011).

214. B. Bartlett, A. Dutt, S. Fan, Deterministic photonic quantum computation in a synthetic time dimension. *Optica* **8**, 1515–1523 (2021).

215. L. Yuan, A. Dutt, S. Fan, Synthetic frequency dimensions in dynamically modulated ring resonators. *APL Photonics* **6**, 071102 (2021).

216. P. Kok, *A First Introduction to Quantum Physics* (Springer International Publishing, 2018).

217. T. Ozawa, H. M. Price, N. Goldman, O. Zilberberg, I. Carusotto, Synthetic dimensions in integrated photonics: From optical isolation to four-dimensional quantum Hall physics. *Phys. Rev. A* **93**, 043827 (2016).

218. X.-W. Luo, *et al.*, Synthetic-lattice enabled all-optical devices based on orbital angular momentum of light. *Nat. Commun.* **8**, 16097 (2017).

219. E. Lustig, *et al.*, Photonic topological insulator in synthetic dimensions. *Nature* **567**, 356–360 (2019).

220. A. Dutt, *et al.*, Experimental band structure spectroscopy along a synthetic dimension. *Nat. Commun.* **10**, 3122 (2019).

221. R. S. Tucker, G. Eisenstein, S. K. Korotky, Optical time-division multiplexing for very high bit-rate transmission. *J. Light. Technol.* **6**, 1737–1749 (1988).

222. A. L. M. Muniz, M. Wimmer, A. Bisianov, R. Morandotti, U. Peschel, Collapse on the line - how synthetic dimensions influence nonlinear effects. *Sci. Rep.* **9**, 9518 (2019).

223. A. L. M. Muniz, M. Wimmer, A. Bisianov, R. Morandotti, U. Peschel, P T-symmetry in Two Synthetic Dimensions in *2019 Conference on Lasers and Electro-Optics Europe and European Quantum Electronics Conference (2019), Paper Pd_2_7*, (Optica Publishing Group, 2019), p. pd_2_7.

224. A. Bisianov, A. Muniz, U. Peschel, O. A. Egorov, Topological Floquet interface states in optical fiber loops. *Phys. Rev. A* **102**, 053511 (2020).

225. A. L. Marques Muniz, *et al.*, Observation of photon-photon thermodynamic processes under negative optical temperature conditions. *Science* **379**, 1019–1023 (2023).

226. M. Monika, *et al.*, Controllable and Scalable Quantum States in Fiber Loop Systems in *Optica Quantum 2.0 Conference and Exhibition (2023), Paper QTh2A.10*, (Optica Publishing Group, 2023), p. QTh2A.10.

227. F. Nosrati, "Characterizing and protecting quantum resources in composite quantum systems.," Université du Québec, Institut national de la recherche scientifique …. (2023).

228. P. Kurzyński, A. Wójcik, Quantum Walk as a Generalized Measuring Device. *Phys. Rev. Lett.* **110**, 200404 (2013).

229. A. Peres, Ed., *Quantum Theory: Concepts and Methods* (Springer Netherlands, 2002).

230. H. E. Brandt, Positive operator valued measure in quantum information processing. *Am. J. Phys.* **67**, 434–439 (1999).

231. F. Hirsch, M. T. Quintino, J. Bowles, N. Brunner, Genuine Hidden Quantum Nonlocality. *Phys. Rev. Lett.* **111**, 160402 (2013).

232. D. Petz, L. Ruppert, Optimal quantum-state tomography with known parameters. *J. Phys. Math. Theor.* **45**, 085306 (2012).

233. J. Bae, L.-C. Kwek, Quantum state discrimination and its applications. *J. Phys. Math. Theor.* **48**, 083001 (2015).

234. J. Singh, Arvind, S. K. Goyal, Implementation of discrete positive operator valued measures on linear optical systems using cosine-sine decomposition. *Phys. Rev. Res.* **4**, 013007 (2022).

235. R. T. Thew, A. Acín, H. Zbinden, N. Gisin, Bell-Type Test of Energy-Time Entangled Qutrits. *Phys. Rev. Lett.* **93**, 010503 (2004).

236. J. A. Bergou, Quantum state discrimination and selected applications. *J. Phys. Conf. Ser.* **84**, 012001 (2007).

237. J. M. Renes, R. Blume-Kohout, A. J. Scott, C. M. Caves, Symmetric informationally complete quantum measurements. *J. Math. Phys.* **45**, 2171–2180 (2004).

238. T. Konrad, A. Rouillard, M. Kastner, H. Uys, Robust control of quantum systems by quantum systems. *Phys. Rev. A* **104**, 052614 (2021).

239. F. Vedovato, *et al.*, Postselection-Loophole-Free Bell Violation with Genuine Time-Bin Entanglement. *Phys. Rev. Lett.* **121**, 190401 (2018).

APPENDIX A

English version of French summary

PHOTON STATISTICS: A VERSATILE TOOL FOR CLASSICAL AND QUANTUM APPLICATIONS

Abstract

Photon statistics is a branch of physics that involves observing the behavior of single or a small number of photons and then aggregating the results through statistical averaging. This process is essential to obtain meaningful and reliable data especially in quantum optics research. Photon statistics provides valuable information about correlations in the electromagnetic field and characteristics of the type of light being measured. For example, second-order correlation function obtained via Hanbury Brown and Twiss experiment is the fundamental way to differentiate between coherent, chaotic and quantum light.

Moreover, extensive investigations into the quantum properties of light resulted in significant progress that allows for precise control of quantum optical systems and sets the stage for genuine quantum engineering. This progress extends to applications in confirming the generation of entangled photons and exploring their properties for various purposes. The non-classical correlation between the entangled photons has resulted in various quantum optical techniques that enable the practical implementation of conceptual experiments that probe the core principles of quantum theory. This enhanced control over quantum phenomena offers exciting opportunities to explore novel information-processing approaches, with the potential to revolutionize technologies rooted in quantum information science.

Driven by the significance and pivotal role of photon statistics, our research pursuits were directed toward two specific domains: the characterization of nanolasers and the characterization of time-bin entangled photons. In the first segment, we delve into the realm of metallic coaxial nanolasers, renowned for their intriguing threshold-less lasing behavior. Through comprehensive photon statistics analysis, we seek to unravel the coherence properties inherent in these nanolasers. Our focus also lies on understanding the elusive threshold-less operation, which has remained a subject of debate and intrigue. To evaluate this unique lasing characteristic, we conduct rigorous second-order coherence measurements alongside time-resolved second-order correlation analyses.

The second segment of this study ventures into the generation and characterization of high-dimensional time-bin entangled photons, a critical resource for quantum technological applications. We simulate a synthetic photonic lattice by employing a coupled fiber-loop system to perform various quantum walk schemes to generate and process high-dimensional time-bin entangled states. Our investigation

focuses on the quantum interference phenomena through detailed photon statistics analysis, with an emphasis on their applications across diverse quantum technologies.

Through these two interconnected research endeavors, this thesis demonstrates the profound significance of photon statistics as a versatile tool, bridging classical and quantum realms, and paving the way for advancements in diverse applications, ranging from nanolasers to quantum technologies.

1. Characterization of metallic coaxial nanolaser

Introduction

The continuous progress in modern society, encompassing fields like health care, education, and transportation, heavily relies on our ability to generate, process, transmit, and receive data. Currently, electronic devices and circuits play a significant role in achieving these tasks, but they are limited by factors such as speed, power consumption, and self-heating effects. To overcome these limitations, the future vision involves replacing electronic devices and circuits with photonic counterparts. Fundamental elements for any photonic system are the light source. Initially, like the first transistors, early lasers were macroscopic devices, occupying a significant physical footprint ranging from centimeters to decimeters. When the size of an electromagnetic cavity is reduced relative to the emission wavelength, fascinating physical phenomena, specific to such cavities, emerge. For example, early experiments conducted in the radio and microwave frequencies showed that the spontaneous emission rate of atoms within a cavity could be either enhanced or inhibited compared to their emission rate in free space. This change in the spontaneous emission rate is found to be influenced by the cavity's geometry in addition to the orientation and spectra of the atoms. This phenomena, known as the Purcell effect has significant applications, including diode lasers with improved modulation bandwidth, enhanced energy efficiency, and thresholdless lasing.

A desirable nanolaser must have ultra-low threshold and exhibit subwavelength dimensions in all three directions, both in its physical size and the confinement of its optical mode. Such devices are crucial for various practical applications, including highly integrated chip-scale photonic circuits, displays, and sensors. Various architectures of small-scale lasers, including VCSELs, micropillar lasers, photonics crystal lasers, etc. have been introduced. However, for some the overall structure remains relatively large, while for others the modes are not well confined to their active regions and can extend beyond the physical boundaries of the cavity, leading to undesirable mode coupling between neighboring devices.

Metal-clad nanolasers, introduced in the late 2000s, have revolutionized this field by enabling both subwavelength physical footprints and mode volumes. In metals, the excited modes are known as surface plasmon polaritons (SPPs), which consist of a photon coupled with a collective oscillation of electrons. SPPs have an effective wavelength that is shorter than the wavelength in free space. This allows for the confinement of electric fields at subwavelength scales. The metal cladding effectively guides optical modes, allowing for precise design of the cavity to channel most of the spontaneous emission into the lasing mode resulting in high β values, which describes the degree of utilization of spontaneous emission into the lasing mode, giving rise to thresholdless lasing. However, it is important to note that nanolasers do have a threshold and should not be confused with hypothetical zero threshold. The threshold of these lasers cannot be determined by usual classical approaches, such as linewidth narrowing or Light input - Light output

curve ($L - L$ curve). Therefore, we need to utilize second-order correlation measurements ($g^2(0)$) carried out through Hanbury Brown and Twiss (HBT) setup to determine the actual threshold. This function depends on the nature of the light source and is independent of the input or the output power.

Metallic coaxial nanolaser

In our studies, we used a metallic coaxial nanolaser with the dimensions of R_{core} = 65 nm and Δ = 285 nm (the schematic of the metallic coaxial nanolaser is shown in Fig. 1). The laser comprises a metallic rod (R_{core}) surrounded by a silver metal-coated semiconductor ring, which acts as an effective heat sink, aiding the lasing process under optical pumping, and gain medium, which consists of six vertically stacked alternating layers in the form of rings of $In_{x=0.56}Ga_{1-x}As_{y=0.938}P_{1-y}$ and $In_{x=0.734}Ga_{1-x}As_{y=0.57}P_{1-y}$ with 10 nm and 20 nm thickness, respectively. The quantum well system featuring a total height of $h = 260$ nm is protected by SiO_2 (30 nm), and InP (10 nm) for the top layer, as well as an air plug (20 nm) at the bottom. The top and bottom sides, terminated by a SiO_2 plug and air, respectively, enhance mode confinement. Additionally, the SiO_2 layer prevents the formation of unwanted plasmonic modes at the interface, while the lower air plug enables optical pumping and out-coupling of light. This coaxial cavity exhibits several promising properties of an "ideal" nanolaser, including the capability to support ultra-small confined modes despite being subwavelength.

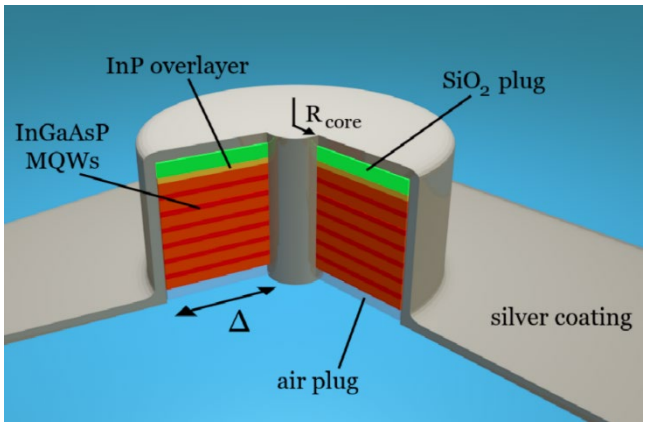

Fig. 1: **Schematic of a metallic coaxial nanolaser.** The system is shaped like a pillar consisting of InGaAsP multi-quantum-wells, surrounding a plasmonic metal core. The top and bottom sides are terminated by a SiO_2 plug and air, respectively, to enhance mode confinement.

The sample containing the metallic coaxial nanolasers was cooled to cryogenic temperatures (77 K) and maintained at a pressure of 10^{-2} mbar. This helped to overcome metal losses by reducing Joule losses and increasing the achievable semiconductor gain thereby improving the performance of metallic coaxial

nanolaser. Consequently, the number of emitted photons was high enough for our single photon detection scheme.

Experimental setup

The metallic coaxial nanolaser was pumped optically by a Q-switched 1064 nm laser with pulse width 5-ns at a repetition rate of 1 MHz. An attenuator was installed in order to control the input power delivered to the metallic coaxial nanolaser without changing the pump laser gain conditions. A detailed illustration of the experimental setup is shown in Fig. 2.

The experimental setup features a kinematic mirror, which directs the coupled output of the metallic coaxial nanolaser either to a monochromator or to an HBT setup. The former characterizes the spectral properties including spectrum and linewidth, utilizing a monochromator in addition to the analysis of $L-L$ curve. The latter studies the coherence properties and temporal dynamics of the nanolaser emission. The HBT configuration consisted of a pair of highly sensitive superconducting nanowire single photon detectors and read out with an electronic time tagger, which were positioned after the 50:50 non-polarizing beam splitter. In the latter path, the light was passed through a diffraction grating and a slit prior to the $g^2(0)$ measurement for spectral filtering and eliminating any pump leakage.

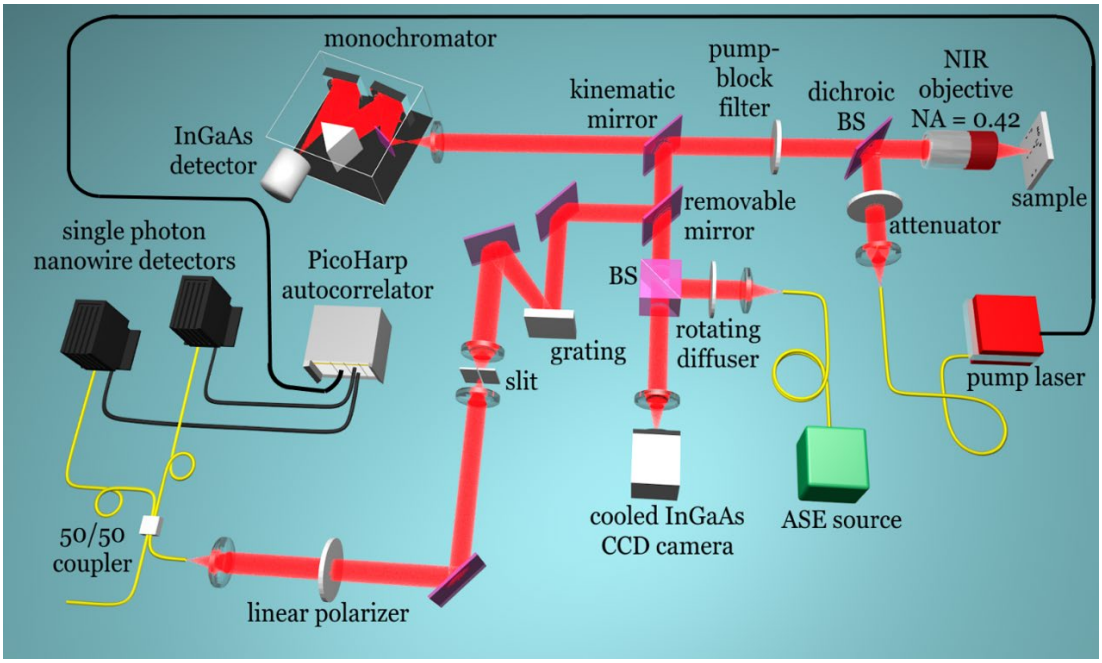

Fig. 2: **Experimental setup for photon statistical coherence and spectral measurements**. The sample containing the nanolasers is held at the focus of an objective lens. The emission from the metallic coaxial nanolaser is directed to three separate beam lines (CCD near-infrared camera, spectrometer or single photon detectors). The sample is cooled down to 77 K (cryo chamber and cooling feed not shown). The optical pumping scheme could be varied between CW operation or pulsed mode with various pulse repetition rates, durations and shapes.

Results

The micro-PL measurement setup was used to do classical measurements. The metallic coaxial nanolaser was excited using a pulsed laser. We varied the average input power between 45 μW and 750 μW. The emission was collected and send to the monochromator. Initially, the spectral data was collected and emission wavelength was found to be ~1300 nm. Moreover, we observed a blue-shift with increasing power, which has been attributed to the saturation of energy states in the quantum well induced by the localized carriers. With increasing pump powers, along with the saturation of quantum states, free carriers tend to spill out from these states, causing a blue-shift of the PL emission. In addition, we measured the linewidth of the nanolaser emission, which increased with increasing input power. This broadening could be the result of refractive index fluctuations related to the carrier density and self-heating effect.

We also plotted the $L-L$ curve for the coaxial nanolaser, where output power is obtained by integrating the spectral power density over the entire PL peak as a function of average input power. Instead of a typical 'S' shaped curve, we observed a linear behavior without any pronounced kink. The absence of a kink is typical of high-β lasers and agrees well with the hypothesis of thresholdless lasing. However, the concept of thresholdless operation based on $L-L$ curve is a subject of debate and therefore, we performed photon statistics measurements to study its thresholdless behavior.

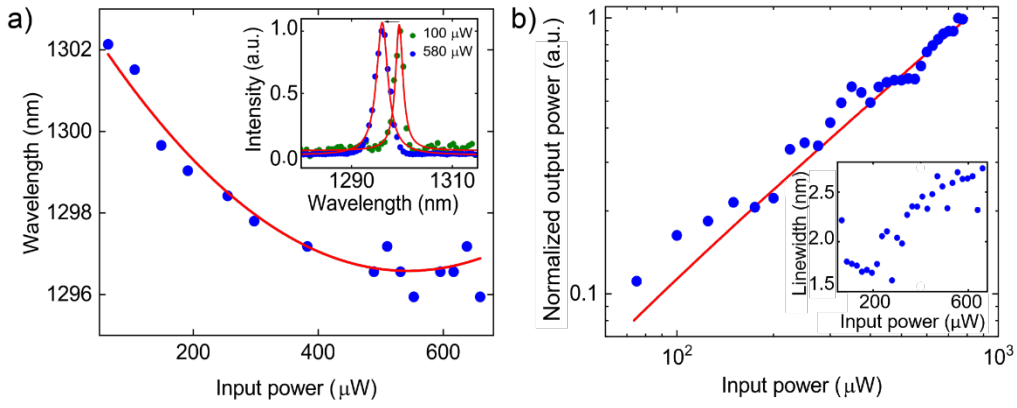

Fig. 3: a) Decrease of the central wavelength for increasing values of the average input power. The inset shows the PL spectra at two different input pump powers. b) Normalized input-output power graph of the metallic coaxial nanolaser in a logarithmic scale. Notably, there is no threshold-like lasing behavior emerging from these measurements.

Following the classical nanolaser characterization, we performed pulsed HBT measurements to determine the photon statistics. First, we averaged the second-order correlation function over the full pump pulse as it is typically done. The $g^2(0)$ for various input powers was determined. We observed that even

though the $L - L$ curve showed thresholdless emission, the nanolaser does pose a threshold. As the input power increased, there was a transition from chaotic to coherent emission of photons from the nanolaser. The chaotic emission in the lower input pump regime is due to spontaneous emission which gradually starts lasing at the threshold. From the HBT measurement, the threshold was determined to by at ~400 μW, where the value of $g^2(0)$ reached near unity. A slight deviation from unity was observed even for higher input powers because of amplitude fluctuations in the pump pulse.

In addition, the width of the normalized correlation peak for different pump powers was determined to track the transition form thermal to coherent behavior because the FWHM is influenced by the pump pulse, and lifetime of the photons. We observed that initially, the width of the peak narrows as the pump intensity increases in the spontaneous emission regime, and falls to minimum in the amplified spontaneous emission regime. For input powers above the threshold, the FWHM broadened and then again narrowed down for higher pump powers due to heating effects.

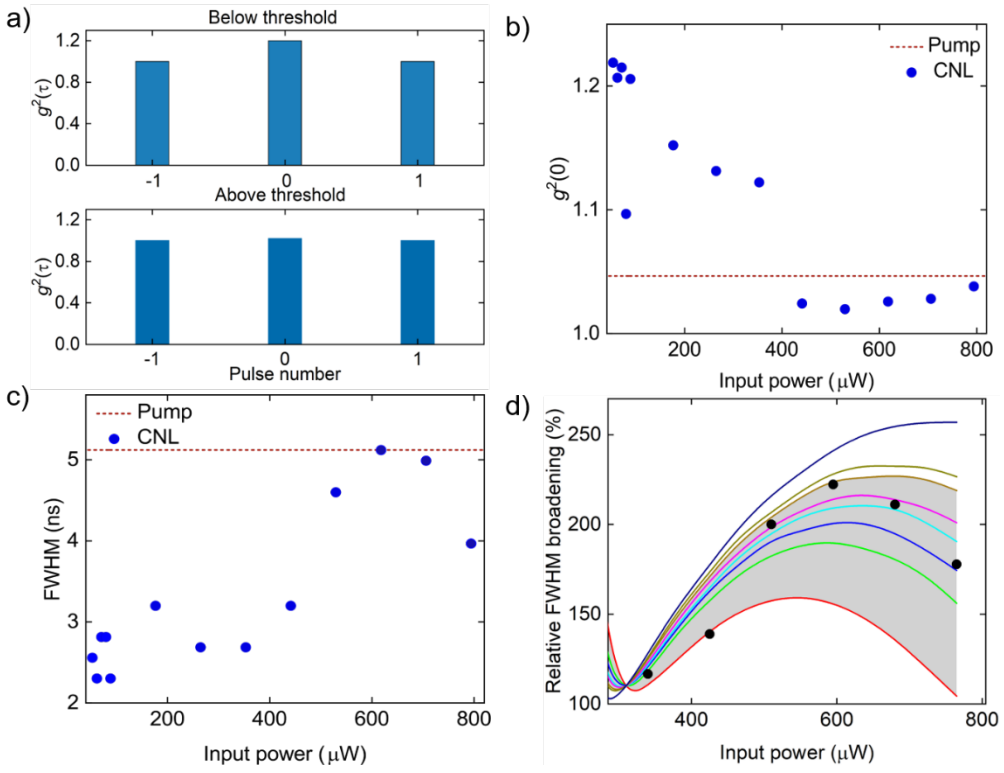

Fig. 4: a) Example of a $g^2(0)$ measurement above and below threshold. b) Second-order correlation function values $g^2(0)$ plotted for varying pump power. c) FWHM of the correlation peaks as a function of average power. d) The FWHM of the autocorrelation trace as a function of the pump power obtained from the rate equation model.

Furthermore, we conducted a detailed investigation of the time-resolved second-order correlation function ($g^2(t,\tau=0)$) within the duration of the emitted pulse from the metallic coaxial nanolaser, using narrower time windows across the entire pulse temporal envelope. We mapped out the transition from a thermal to a coherent response of the emitted pulses within the pulse envelope at various input power levels, without the need for additional spectral filtering. We observed that the leading edge of the pump pulse generates carriers in the higher quantum well or barrier states and these carriers rapidly relax into the lower quantum well states yielding spontaneous emission ($g^2(0) > 1$). As the intensity of the pump pulse increases in time, population becomes sufficiently strong and the system is driven into the regime of coherent emission ($g^2(0) = 1$). Since nanolaser cavities have an ultrafast response, at the trailing edge of the pulse envelope, (where the intensity of the pump pulse is low), spontaneous emission dominates over the coherent emission, leading to $g^2(0) > 1$. Moreover, for higher excitation densities, stimulated emission is maintained for a longer time resulting in an asymmetry in the time resolved data.

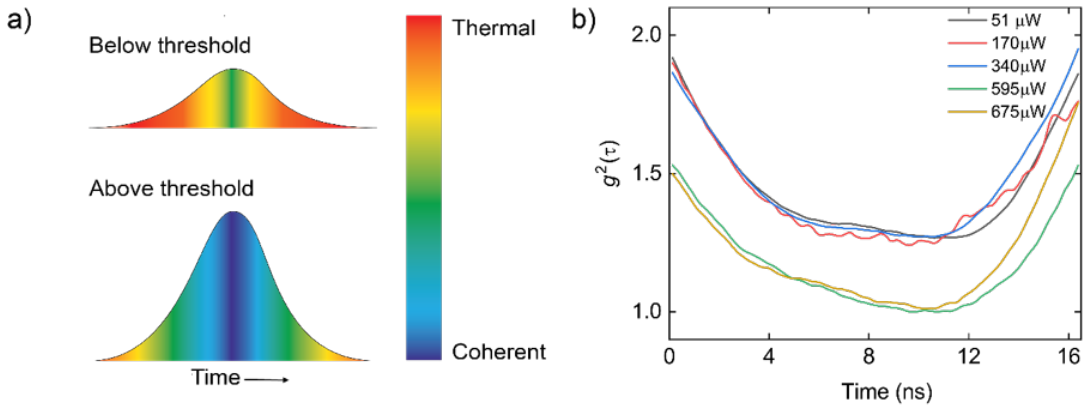

Fig. 5: a) Schematic of the expected photon statistic as a function of the emitted pulse's temporal envelope shown for two cases, above and below threshold. b) $\boldsymbol{g^2(\tau)}$ evolution from a thermal (photon bunching) to a coherent behavior scanned over the emitted pulse length.

In summary, our investigation involved classical characterization and photon statistics to comprehensively study the emission properties of a thresholdless nanolaser. It became evident that conventional methods like the $L-L$ graph and spectral characterization were insufficient, and photon statistics emerged as the key approach to extract the nanolaser's emission behavior. Our findings indicate that the emission from the nanolaser, even at higher input powers, comprises a combination of spontaneous and stimulated emission.

2. Characterization of time-bin entangled state

Introduction

The enhanced control over quantum phenomena, due to advancements in the field of quantum engineering, offers exciting opportunities to explore novel information-processing approaches with the potential to revolutionize technologies rooted in quantum information science. One of the most important resources in quantum technology is entanglement. Entanglement is a purely quantum phenomenon which refers to the correlation between two or more quantum systems where the state of one system cannot be described independently of the other. This phenomenon offers unique advantages in quantum information science, including quantum computation, quantum communication, quantum simulation, and quantum metrology. Entanglement provides the key to achieve 'quantum supremacy, particularly in systems utilizing qubits. A qubit, a two-level system, is the basic unit of information in quantum technology.

Quantum information can be encoded in various physical systems, including Rydberg atoms, trapped ions, solid-state defects, polar molecules, superconducting circuits, and photons. Among these, photons are particularly suitable due to their advantageous properties such as high speed, minimal interaction with the environment, long coherence times, and well-established technologies for their generation, manipulation, and detection. Moreover, they possess many external as well as internal degrees of freedom. Internal degrees of freedom include polarization, orbital angular momentum, frequency and generation time, while the external degrees of freedom include the spatial position and the path traveled by a photon. Consequently, the development of experimental techniques to generate suitable quantum photonic states becomes crucial for practical applications.

Early experiments using polarization, optical paths, and orbital angular momentum modes were performed in free space. However, the development of fiber-based telecommunications has led to exploitation of robust and fiber-compatible degrees of freedom, such as frequency and time. The concept of using time-bins to carry quantum information was first proposed in 1989 and subsequent experiments successfully demonstrated two-dimensional time-bin entanglement. To create entanglement between two photons and encode quantum information in the time-bin domain, two indistinguishable laser pulses separated by a fixed time difference are utilized. Each laser pulse generates photon pairs using a nonlinear light sources such as spontaneous parametric down-conversion (SPDC).

For applications like quantum communication or quantum computation, high-dimensional quantum system, or qudits, offer advantages over qubits due to their higher information capacity, enhanced security and resilience to noise. Therefore, high-dimensional quantum entanglement provides a rich area for both fundamental research and technological innovation.

In principle, the dimensionality of the time-bin entangled states can be scaled up by increasing the number of indistinguishable pulses. However, characterization of high-dimensional entangled states requires estimation of numerous parameters, such as the multiple phase values that arise from delays between pulses. The estimation process demands a large number of measurements, which becomes impractical as dimensionality increases. Experimental limitations further constraints efficient entanglement processing. The setup for their characterization typically involves the utilization of cascaded unbalanced interferometers, where each interferometer measures the phase between two time-bins. Thus, an N-dimensional time-bin entangled states requires $\mathrm{N}-1$ interferometers, which becomes infeasible for large N. Moreover, this results in significant experimental complexity and cost. Therefore, efficient and innovative methods to generate and process high-dimensional time-bin entangled states, particularly in optical fibers, are crucial for practical quantum communication.

In optical fiber networks, the generation and processing of high-dimensional time-bin entangled states can be realized through quantum walks. Quantum walks, the quantum analog of the classical random walks, rely on interference and superposition. As a generalized measurement device, they effectively describe the transport of entangled photons in optical fiber networks. For example, a coupled fiber loop system, which can simulate a synthetic photonic lattice, has been extensively employed to study the nonlinear propagation of light through quantum walks. However, the application of this system in quantum information processing and quantum technologies remains largely unexplored.

These considerations motivate us to experimentally investigate 1) the generation of high-dimensional time-bin entangled states in synthetic photonic lattice and 2) processing of the generated entangled states via various quantum walk schemes.

Synthetic photonic lattice and controlled quantum walk

In our work, the synthetic photonic lattice is implemented using a coupled fiber-loop system comprising two fiber loops of varying lengths coupled with an optical switch that can control the proportion and the direction of flow of light. The in and out-flow of light pulses in the coupled fiber-loop system are controlled by two other optical switches, named gate 1 and 2. To understand synthetic photonic lattice, let us consider the coupled fiber-loop, where the optical switch is kept at 50-50 transmission-reflection ratio all the time. Whenever a light pulse reaches the optical switch, it splits the pulse splits equally into long and short loops. The difference in time taken by these pulses to reach the beam splitter after each roundtrip corresponds to the difference in the lengths of the fiber loops. The roundtrip and the arrival time of the pulses define the time-step (t) and synthetic position (x), respectively, in the synthetic photonic lattice, enabling one-dimensional discrete time quantum walk (DTQW) using the light pulse. However, to obtain

optimal measurements, we need to employ controlled quantum walk scheme, where we utilize the dynamical properties of the optical switch.

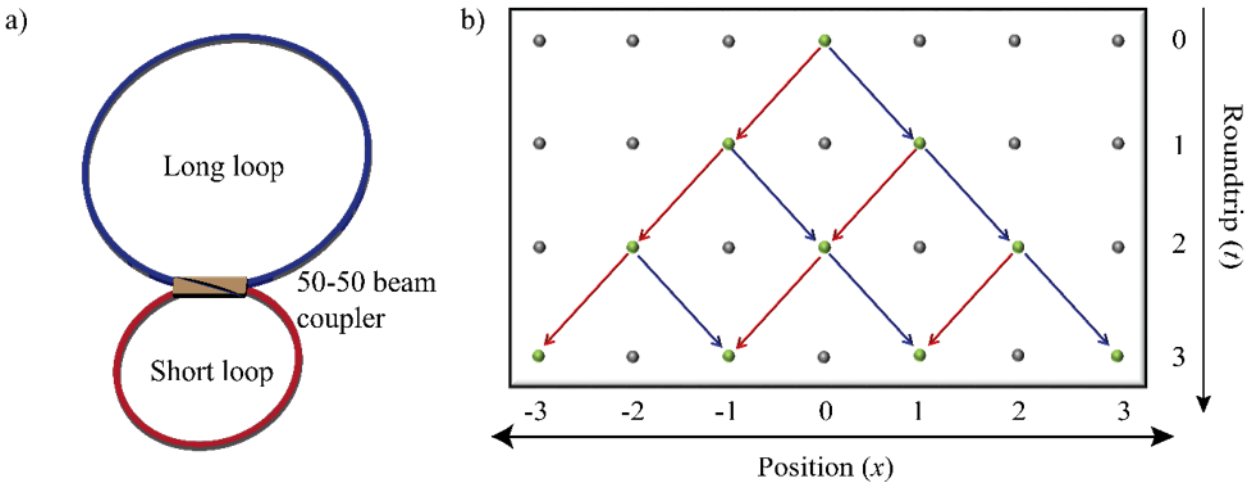

Fig. 6: a) Coupled fiber-loop consisting of two fiber loops of different lengths coupled with a 50-50 beam coupler. b) Quantum walk describing the propagation of light pulse in the coupled fiber-loop system.

The controlled quantum walk comprises three operations, namely Reflection (100:0), Transmission (0:100) and Fourier (50:50) depending on the splitting ratios of the optical coupler. In case where the light pulse is in the long loop, reflection operation shifts from long loop to short loop, while for transmission, it remains in the residing loop, that is, the long loop. When the optical switch is set to Fourier operation, the optical switch equally splits the light pulse into long and short loops.

Experimental setup

The complete experimental setup shown in Fig. 7, consists of four main tasks: 1) Generation of classical double pulse, 2) Generation of time-bin entangled state and information encoding, 3) Processing stage that includes quantum walk and finally, 4) The detection stage.

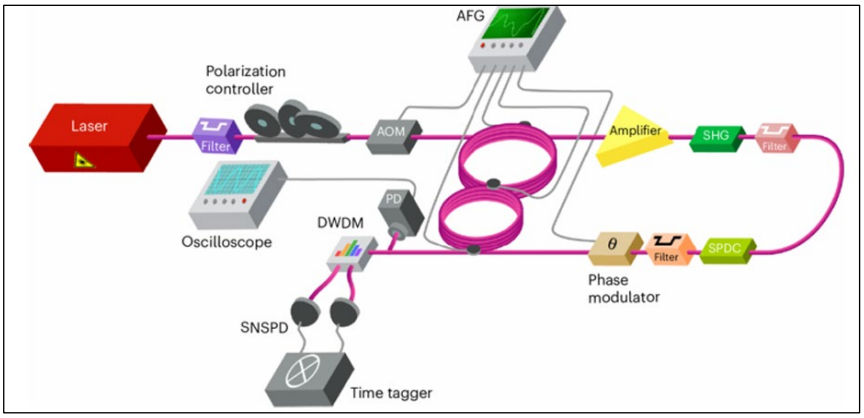

Fig. 7: **Experiment setup.** The repetition rate of the output from the fs laser is reduced to 181.81 kHz using an acousto-optic modulator (AOM). These pulses are sent to the loop system to generate two classical pulses for the state preparation. The classical pulases are passed through the periodically poled lithium niobate (PPLN) crystals for the generation of a pair of correlated photons in two time bins, t_1 and t_2 The PPLN1 crystal generates second harmonic generation that is used by the second PPLN2 crystal for spontaneous parametric down conversion (SPDC), from which correlated photon pairs are generated. The entangled states are fed to a phase modulator for phase encoding. The phase-encoded time-bin entangled photons are allowed to interfere in the fiber-loop system. The interfered peaks at various encoded phase are sent to dense wavelength-division multiplexer (DWDM) to separate signal and idler photons. These signal and idler photons are detected by the state-of-art single photon detectors.

The classical pulse generated by the laser is directed through gate 1 to prepare double pulse, with the optical switch kept at 50-50 during the process. The generated double pulses, separated by a delay corresponding to the difference in the lengths of the short and long loops, are used to excite a pair of periodically poled lithium niobate (PPLN) waveguides to generate signal-idler photon pair in two time bins, t_1 and t_2. Later, the prepared quantum state undergoes individual phase information encoding $\phi = \{\phi_1, \phi_2, \ldots \phi_n\}$ utilizing a phase modulator. The resulting state, $|\psi_1\rangle = \frac{1}{\sqrt{2}}\left(|t_1, t_1\rangle_{s,i} + e^{2i\phi}|t_2, t_2\rangle_{s,i}\right)$, is then injected into the quantum walk platform through gate 2 to undergo the optimal measurement scheme utilizing controlled walk, which requires two roundtrips (Fig. 8).

For the uncontrolled DTQW, the optical switch was set at Fourier operation all the time. In the second roundtrip, the first time-bin the long loop and the second time-bin in the short loop reached the optical switch at the same time resulting in quantum interference. The interfered component in the short loop where then taken out through gate 2 and was directed towards the detection stage.

For the controlled DTQW, initially, quantum bins are injected into the system through the short loop. During the first roundtrip, we do reflection and transmission operations to govern the arrival of t_1 and t_2, shifting t_1 to the long loop ($x = -1$) and t_2 to the short loop ($x = 1$). In the subsequent roundtrip, the Fourier operation distribute the interference components between the short and long loops. Finally, the interfered component is directed to the detection stage through gate 2.

A telecom compatible dense wavelength-division multiplexer (DWDM) separates the signal and idler photons, which are sent to the state-of-the-art single photon detectors. The arrival time of the signal and idler photons are recorded by a time-tagging electronics.

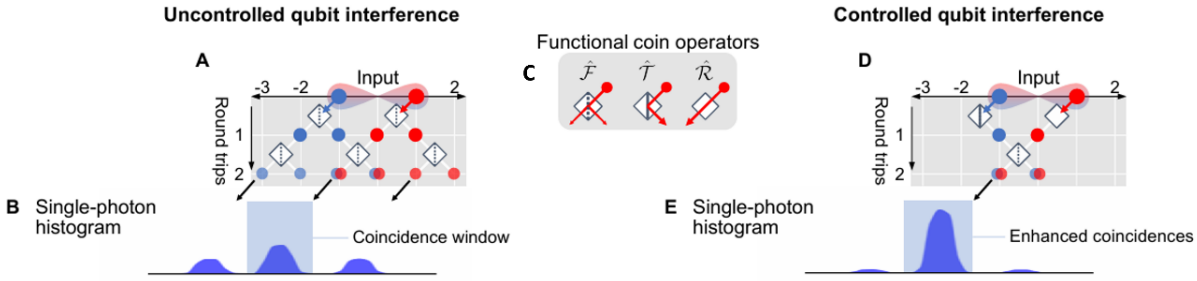

Fig. 8: The uncontrolled a) and controlled d) quantum walk scheme in synthetic photonic lattice. c) represents various coin operations employed in the quantum walk. b) and e) are the illustration of single photon histogram obtained in controlled and uncontrolled quantum walk schemes.

We also generated four-dimensional time-bin entangled states in the same platform. In contrast to two-dimensional case, this required four roundtrips. Once the classical four pulses that are in coherent superposition is generated, they were sent excite a pair of PPLN waveguides to generate four-dimensional time-bin entangled states. The quantum state is given by $|\psi_1\rangle = \frac{1}{\sqrt{2}}\left(|t_1, t_1\rangle_{s,i} + e^{2i\phi}|t_2, t_2\rangle_{s,i} + e^{4i\phi}|t_3, t_3\rangle_{s,i} + e^{6i\phi}|t_4, t_4\rangle_{s,i}\right)$.

The four-dimensional time-bin entangled state was then sent to the coupled fiber-loop system for processing. We utilized two controlled DTQW schemes to obtain interference fringes. The controlled quantum walk scheme 1 consisted of two operations: Reflection and Fourier. For the first two roundtrips, we kept the optical switch at Fourier operation and for the third roundtrip, we kept the optical switch at full Reflection. In the final roundtrip, the optical switch was again kept at Fourier operation to undergo quantum interference. The interfered signal along with side modes were then directed towards the detection state.

In the second control scheme, we sliced the entangled state, that is, the first two time-bins were sent to the long loop and the last two time-bins were kept in the short loop. In the second roundtrip, the optical switch was kept at full Reflection mode allowing the time-bins to stay in their respective loops. In the following two roundtrips, the optical switch was kept at Fourier operation for quantum interference. The interfered signal along with accompanying modes were taken out through gate 2 and was sent to the detection stage.

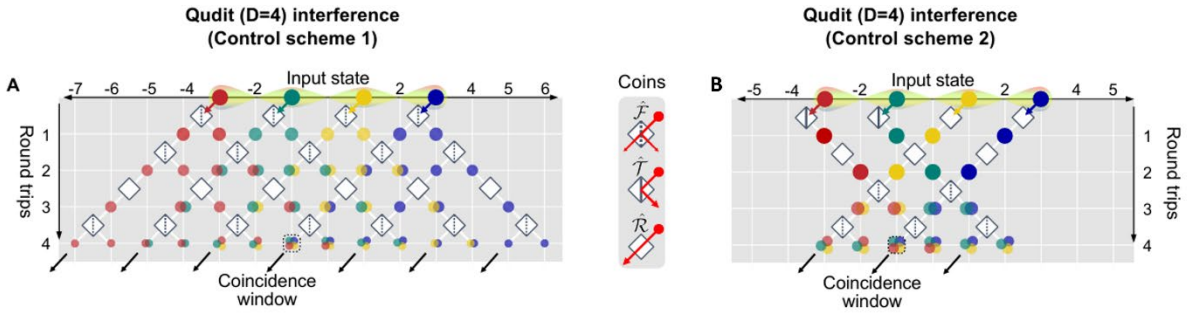

Fig. 9: The controlled DTQW schemes 1 (a) and 2 (b) in synthetic photonic lattice.

Results

We collected the photon statistics at each phase setting, $\phi \in (0, \pi)$ and measured the interference fringes for two and four-dimensional time-bin entangled states.

Fig. 10 (a) and (b) demonstrate the interference fringes obtained through controlled and uncontrolled quantum walks, respectively, employed for two-dimensional time-bine entangled states . The visibilities of these fringes were estimated to be 95.45%, and 90.17%, respectively, and these violated the Bell inequality.

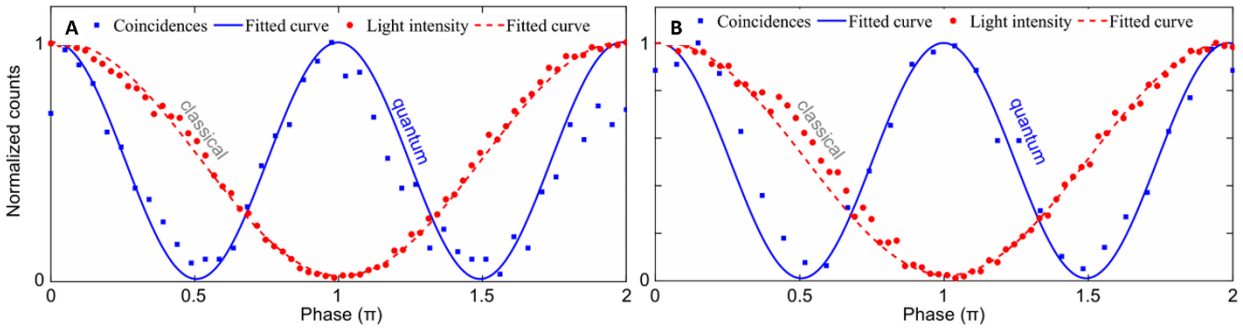

Fig. 10: **Interference fringes.** a) Interference fringe obtained by utilizing uncontrolled quantum walk scheme. b) Interference fringe obtained through controlled quantum walk scheme.

The interference fringes for four-dimensional time-bin entangled states obtained via controlled DTQW scheme 1 and 2 are given in Fig. 11 (a) and (b), respectively. The visibilities of these fringes were estimated to be 91.55%, and 89.51%, respectively, and these violated the CGLM inequality.

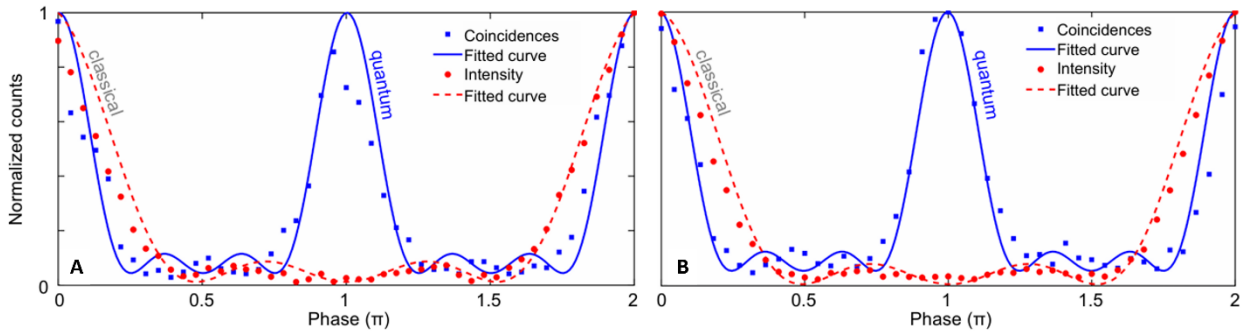

Fig. 11: **Interference fringes.** a) Interference fringe obtained by utilizing controlled quantum walk scheme 1. b) Interference fringe obtained through controlled quantum walk scheme 2.

We demonstrated the quantum properties of SPL as a promising framework for the preparation, generation, and manipulation of d-dimensional time-bin entangled photon pairs based on a dynamically coupled fiber-loop system and discrete-time quantum walk. We could implement a controlled quantum walk scheme enabling us to measure post-selection free quantum interference for two-dimensional entangled states, as well as to optimize the evolution of the quantum walker for higher detection efficiencies and coincidence counts for both two- and four-dimensional cases.